Vacuum-UV photoabsorption imaging of Laser Produced Plasmas.

A thesis submitted for the degree of

Doctor of Philosophy

by

John Stephane Hirsch

Dublin City University

School of Physical Sciences

Research Supervisor
Dr. John T. Costello

May 2003

Declaration

I hereby certify that this material, which I now submit for assessment on the program of study leading to the award of Doctor of Philosophy is entirely my own work and has not been taken from the work of others save and to the extent that such work has been cited and acknowledged within the text of my work.

Signed : _____ I.D. No. : _____

Candidate

Date : _____

To Vanessa and Julia

Acknowledgements

First of all I wish to thank my supervisor, Dr. John Costello for all the support and encouragement over the years. We went through good times and bad times, and encountered many problems all along and I hope we are able to present quality results in this thesis. At the same time I have to thank john for being a friend and I will keep very blurred memories of the many extra-curricular activities spent in various fine establishments.

I would also like to thank Des Lavelle, and Cian Merne for all the work and extra hours spent on the construction of the system, and of course for the numerous discussions and laughs in "ze workshop" and Pat Wogan for his help with electronics.

I would like to extend my thanks to Prof. Piergiorgio Nicolosi and Dr. Luca Poletto, for their help and assistance with the ray tracing and the alignment of the of the system.

I am very grateful to Dr. Jean Paul Mosnier, Prof. Eugene Kennedy and Dr. Paul Van Kampen for their help, advice and assistance over the years. At the same time I was lucky to meet the different CLPR generations:
The old school: the famous moody trio, i.e., Oonagh, Eilish and Dierdre and the local jedi master, Andy Gray.
The contemporary school: Mohamed, Mark, Alan, Sarah, Pat, Jonathan, Murph.
The new physicists in block II: Kevin and Eoin.

Finally and I would like to thank my parents for giving up asking question about the content of this thesis and my brother Jerome for all his help.

Abstract

Complementary to the existing VUV/soft X-ray spectroscopic systems, a VUV photoabsorption imaging optical system has been developed.The technique consists in passing a pulsed VUV beam, tuned to an atomic/ionic resonance, through a laser plasma plume and recording the transmitted light or shadowgram.

A first optical set-up was designed and built as proof of principle to validate the photoabsorption technique. The promising results obtained, as well as the limitations of the system lead, to the design and fabrication of a new system with improved flux collection, probe beam quality, spatial and spectral resolution. The design of both systems was done with the aid of a ray tracing code, and the calculated performances from the simulations were compared to experimental measurements.

Time and space resolved distributions of atomic calcium, Ca^{+}, Ca^{2+} equivalent width were measured using the respective 3p-3d resonances, and information on the plasma expansion dynamics was extracted and compared with an expansion model. With the absolute cross section known, maps of equivalent width could be converted to maps of column density NL; this was achievable when using the 3p-3d Ca^{+} resonance at 37.43 nm and the 5p-5d Ba^{+} resonance at 46.7 nm.

Chapter 1

Introduction

The main aim of the project is the construction of an imaging system operating in the VUV wavelength range dedicated to photoabsorption studies of expanding laser produced plasmas. This system is to provide time and space resolved maps of column density of the plasma plume for transitions where the absolute cross section is known. The motivation for this project is to address the need for new absorption imaging diagnostics in the VUV wavelength range and to add to the DCU laboratory a new capacity working alongside and supporting the existing spectroscopic systems.

This thesis consists of three main chapters; chapter 1 introduces the basics of plasma formation and plasma processes. The theoretical background needed for the results analysis, i.e., the derivation of column density maps, is presented and the equation of radiative transfer is derived. We present a solution for the specific case of photoionisation depending on the plasma plume opacity conditions. A plasma expansion code is described here to compare with experimental observations on the dynamics of the plasma evolution.

Chapter 2 describes in detail the two optical systems used in this work. The first system was tested in the Rutherford Appleton Laboratory and was used as a proof of principle experiment prior to the design and construction of the final optical set-up in the DCU laboratory.

Chapter 3 presents the results and analysis of photoabsorption studies using the 3p – 3d resonance lines of neutral calcium as well as singly and doubly charged calcium ions. A similar experiment has been performed on singly charged barium ions in the 5p-excitation region.

This thesis is concluded by a summary of the results obtained and suggestions on further applications of the photoabsorption imaging system.

Laser Produced Plasmas constitute a cheap, compact, and competitive light source compared to large synchrotron facilities. Radiation emission with wavelength ranging from the infrared region to x-rays, and Vacuum-UV (VUV) photon flux of up to 10^{14} photon.nm^{-1}.sr^{-1} (Fischer *et al.*. 1984) from table top Q-switched laser plasma continuum sources is possible.

This project is inspired by a well established technique for measuring photoabsorption spectra of almost all atoms and singly/multiply charged ions known as the Dual Laser Plasma (DLP) method (Carroll and Kennedy 1977, Costello *et al.* 1991, Jannitti *et al.* 1993). In DLP spectroscopic experiments, one laser plasma constitutes the absorbing 'sample' while the other forms the VUV (continuum) backlighting source (Carroll *et al.* 1983). VUV light passing through the sample plasma is dispersed by a spectrometer and recorded on a VUV sensitive array detector. Varying the delay between the formation of the 'sample' and 'light source' plasmas one can measure the time resolved photoabsorption spectrum of the sample plasma. By recording photoabsorption spectra in different spatial zones of the sample plasma it is possible to build up a picture of how the plasma evolves in space and time.

The first experiment of this kind was performed by Carillon *et al.* (1970), using two aluminium plasmas, one as a backlighting source and the other one as the sample plasma. However, the very line dominated spectrum of aluminium in the VUV region reduced the observation to very narrow wavelength bands that were free of strong lines and were occupied mainly by bremsstrahlung continuum. This experiment revealed the need for a broad-band continuum source for absorption studies. In 1973 Breton and Papoular showed continuum emission in the VUV region using a tantalum target, their aim being to obtain a strong bremmstrahlung continuum source near the Lyman α line at 121.5 nm to study the neutral hydrogen density in various devices. Further studies have been successfully performed to obtain line free continua in the VUV and XUV region, using other high Z materials such as tungsten, samarium, ytterbium and europium (Caroll *et al.* 1978, O'Sullivan *et al.* 1981,1982) as targets. Since then the dual laser plasma technique has revealed itself to be a very powerful technique leading to characterisation of multiple new transitions in the VUV and XUV wavelength range (West 2002, Meighan 2000). However very few imaging experiments have been performed in the VUV wavelength ranges as opposed to extensive imaging studies in the X-ray or visible region (Michette *et al.* 1994, Geohegan 1992).

In the X-ray region, the interest shown by the fusion community in laser produced plasmas led to extensive work using laser plasmas as X-ray sources either for spectroscopic studies or imaging experiments. A very similar set-up to the DLP technique is used in point projection absorption spectroscopy (DM O Neill *et al.* 1991, Balmer *et al.* 1989) where a point plasma source emitting X-ray radiation is used to probe a second, larger expanding plasma. The larger plasma absorbs the projected X-rays, which are reflected on a flat or spherical crystal and the data are recorded either on photographic films or by the use of a charged coupled device (CCD). This technique enables the measurement of the population density of the different absorbing ions. The spatial resolution can be better than 10 μm, determined by the size of the backlighting X-ray source and a spectral resolving power up to a few thousand has been achieved (Pikuz *et al.* 2000). On the imaging side, X-ray backlighting is a very important and powerful technique especially as a diagnostic tool for research on inertial confinement fusion (Raven *et al.* 1981). Direct drive inertial confinement fusion can be achieved by irradiating spherical pellets containing a mixture of deuterium and tritium with high power lasers. The laser radiation ablates the outer skin of the capsule and produces high pressure waves that accelerate the capsule inwards to an implosion and, doing so, compresses the fusion fuel at the centre. Four important phenomena take place during the reaction and the X-ray backlighting technique has been revealed to be an adequate tool for their study.

Grun *et al.* (1984) used the technique to measure Rayleigh-Taylor instabilities in ablatively accelerated pellets and differentiate its effects from effects caused by a non-uniform beam profile. Kalantar *et al.* (1997) used an X-ray laser backlighter, coupled to multilayer XUV optics, to study the imprint of the laser beam on a thin foil and thus determine the non-uniformities in the laser radiation. Ablative acceleration of thin foils was studied to simulate spherical pellets in their early imploding phase by Whitlock *et al.* (1982) and Daido *et al.* (1984). Finally, face on X-ray backlighting was used by Shigemori *et al.* (1997), to successfully measure the time resolved mass ablation rate of laser irradiated targets.

In the visible region direct imaging of the light emitted from plasma plumes with gated CCD cameras (Geohegan 1992, Whitty and Mosnier 1998) and of the light absorbed from wavelength tuned lasers (Martin *et al.* 1998) are also increasingly important diagnostics of laser ablated/plasma plumes. The former provides space and time resolved information on excited states of atomic and molecular species, while the latter can provide

corresponding data on ground state or 'dark' species. However, tabletop tuneable lasers are limited for many practical purposes to wavelengths in excess of 300 nm if one requires pulse energies above a few mJ. Hence, they can access the resonance lines of at most singly charged atomic ions and even then not all such species.

In this work, we will show that probing a laser ablated plasma plume with monochromatic VUV light can overcome this limitation. In contrast to the usual DLP spectroscopy experiment we pass a VUV beam, tuned to an atomic or ionic resonance, through a laser-plasma plume and measure the resultant transmitted image (or shadow). In this way we are able to obtain directly the spatial-temporal distribution of plasma species. This method has a number of attractive features for application to laser ablated plasma plume characterisation – namely:

- VUV light can access resonance lines of all atoms and moderately charged ions. Hence one can track ions of any element and in any charge state with resonance energies up to the photon energy limit of the VUV source and any associated optics. In the two systems presented in this work, the upper photon energy limit is 35 eV since we are using near normal incidence monochromators
- VUV light can access the higher density regimes that are excluded from visible light photoabsorption/shadowgraphy techniques
- The pulsed laser plasma light source emits VUV radiation typically for < 1-50 ns, depending on the heating pulse duration; hence the frame time or temporal resolution available can be short and achieved automatically without any additional fast switching requirement. By varying the interlaser delay the plasma may be shadowgraphed at different times after its creation

However, the most important point is that the laser plasma source makes the analysis of the transmitted light distribution relatively uncomplicated; it is, to a very good approximation, a direct image of photoabsorption within the plume. The main reasons for this are:

- The dimension and effective relative bandwidth of the laser plasma source means that it is essentially an incoherent source and hence image analysis is not complicated by the presence of interference patterns
- Refraction of a VUV beam in a plasma with given density gradient is significantly reduced compared to the case for a visible beam, with beam deviation angles scaling approximately as $(\lambda_{probe})^2$

The use of VUV radiation as a probe has another very important advantage – it can be used to photoionize atoms or ions, a process immune from the usual radiation transfer problems, which complicate optical probing of plasmas with ground state (bound) resonance transitions. In particular, tuneable VUV radiation can be used to induce *resonant photoionization*, which we will demonstrate for Ca^+ and Ba^+ via the path:

$$Ca^+ (3p^6 4s\ ^2S) + h\upsilon \rightarrow Ca^{+*} (3p^5 4s\ 3d\ ^2P) \rightarrow Ca^{2+} (3p^6\ ^1S) + e^-$$

$$Ba^+ (5p^6 6s\ ^2S) + h\upsilon \rightarrow Ba^{+*} (5p^5 6s\ 5d\ ^2P) \rightarrow Ba^{2+} (5p^6\ ^1S) + e^-$$

The branching ratio for fluorescence to electron emission processes for such VUV excited (inner-shell) resonances, tends to be significantly less than 10^{-4} (Schmidt 1992). Hence, almost all absorbed photons are converted to electrons and one does not have to be concerned about multiple photon absorption/re-emission cycles in the plasma plume up to the detectable opacity.

For those atoms (and ions) for which measured photoionization cross-sections are available one can extract column density values (NL) or (for well-defined plume dimensions) actual atomic or ionic number densities (N). Since peak values of photoionization cross-sections for resonant inner-shell excitations can be as high as 2200 Mb for the Ca^+ 3p – 3d resonance line (Lyon *et al.* 1986), column densities can be as low as $\sim 5 \times 10^{13}$ cm^{-2} . This corresponds to a transmittance (I/I_0) of ~ 0.9, which can be easily measured with our system. Below this value, significant efforts are needed to account for noise, small residual scattered light effects and small drifts in the VUV light source level during a multi laser shot exposure. The use of inner shell excitations brings another advantage; excitation energies for different stages of ionization tend to be displaced slightly from each other. Thus, keeping all other experimental conditions identical, one can readily image different ionization stages of the same atom in one experiment by tuning the monochromator energy to the relevant resonance lines.

Chapter 2

Theoretical Background

2. Overview

The generation of plasmas has become over the years, one of the main applications of lasers since their invention some 40 years ago. Plasma is described as the fourth state of matter and constitutes close to 99% of all matter in the universe, it can be generated using mainly electrical discharges or at the focus of an intense laser beam in the laboratory (Carroll and Kennedy 1981). The main characteristics of laser produced plasmas as opposed to discharges through a low pressure gas is their high temperature and high density of ions and electrons. Thus laser plasmas have imposed themselves as an important radiation source and constitute an important tool for atomic spectroscopy enabling the study of highly ionised species. In this section we explain briefly the interaction of the laser beam with the target surface and the resulting formation of the plasma plume.

2.1. Plasma formation

When the output of a high power, Q-switched, laser is focused onto a solid target a dense, high temperature plasma is formed. Radiative emission , i.e., photons with wavelength ranging from the Infra-red to the X-ray as well as emission of singly or multiply charged ions, neutral particles and electrons occur during the duration of the plasma. The creation, heating and expansion phases of laser produced plasmas has been discussed in detail by Hughes (1975), Radziemski (1989) and most recently by Elizer (2002) and also in many review papers (Carroll and Kennedy 1981). Laser radiation reaching the surface of a metallic target only penetrates into the surface by a small distance. This penetration depth or skin depth is estimated to be only a fraction of the laser light wavelength. The skin depth

depends on the laser light frequency as well as on the target type and can be expressed as (Corson and Lorrain 1988)

$$\delta = \sqrt{\frac{2}{\omega\mu\sigma}} \qquad [2.1]$$

with ω the laser light angular frequency, μ the metal magnetic permeability and σ the metal conductivity.

Nevertheless the resulting electric field is of great magnitude; assuming a laser irradiance Φ of 10^9-10^{12} W.cm^{-2} (typical irradiance used in our laboratory), and given that the laser irradiance and the E field are related by the following equation:

$$E = 19.4\ \phi^{1/2} \qquad [2.2]$$

We obtain an electric field of the order of $6 \times 10^5 - 2 \times 10^7$ V.cm^{-1}, and thus a very intense laser-target interaction results in the formation of a very thin and dilute plasma at the surface of the target. The laser radiation is then absorbed by the initial dilute plasma, which leads to an increase in the electron kinetic energy. As a result, the electron temperature increases, causing more and more atoms to be ionized and thus increasing the electron density until it reaches the "critical density". The critical density of the plasma can be explained by an analytical treatment of electron oscillations with respect to ions, which are taken to be at rest due to their larger mass. The angular frequency of these oscillations or plasma frequency can be calculated to be:

$$\omega_p = \left(\frac{n_e e^2}{m_e \varepsilon_0}\right)^{1/2} \qquad [2.3]$$

where n_e is the electron density and m_e is the electron mass. For a wave travelling in the plasma, the frequency of the incident wave can be related to the plasma frequency through the following dispersion relationship:

$$\omega^2 = \omega_p{}^2 + c^2 k^2 \qquad [2.4]$$

with k the propagation constant and c the speed of light. For $\omega > \omega_p$, k is real and the wave can propagate, for $\omega < \omega_p$, k is imaginary and the wave does not propagate substantially into the plasma. For $\omega = \omega_p$ reflection occurs and we can derive an expression for the critical density:

$$n_c = \frac{\varepsilon_0 m_e \omega^2}{e^2} \qquad [2.5]$$

When the electron density reaches the critical density in the plasma, the laser radiation does not reach the target surface anymore. However, the plasma still continues to expand being heated up by the absorption of laser radiation energy which proceeds mainly via inverse Bremsstrahlung at the intensities used here (Kennedy 1984). The increase in the plasma volume results in a decrease in the electron density, the laser radiation can then reach the surface of the target again. This process is continuous and self-regulating during the length of the laser pulse (Hughes 1975). The plasma temperature can be taken to be approximately constant during the duration of the laser pulse, due to fast energy absorption. When the laser pulse is terminated the plasma can then expand adiabatically in vacuum (Singh and Narayan 1990). It is during this expansion phase of the plume that much of the data in this thesis was acquired and the topic will be discussed in detail in section 2.5.

2.2. Radiation and ionization processes in plasmas

In this section we will discuss the different processes leading to radiation emission in laser produced plasmas. We will divide this section into 3 subsections dealing with bound-bound transitions, free-bound transitions and free-free transitions noting that for every emission process an exactly opposite process exists in order to satisfy equilibrium requirements. Each of these processes depends on the conditions of the plasma formation and in turn on the plasma parameters , i.e., temperature and density, which determine the relative importance of the different type of transitions. The excitation and de-excitation paths are illustrated in figure 2.1.

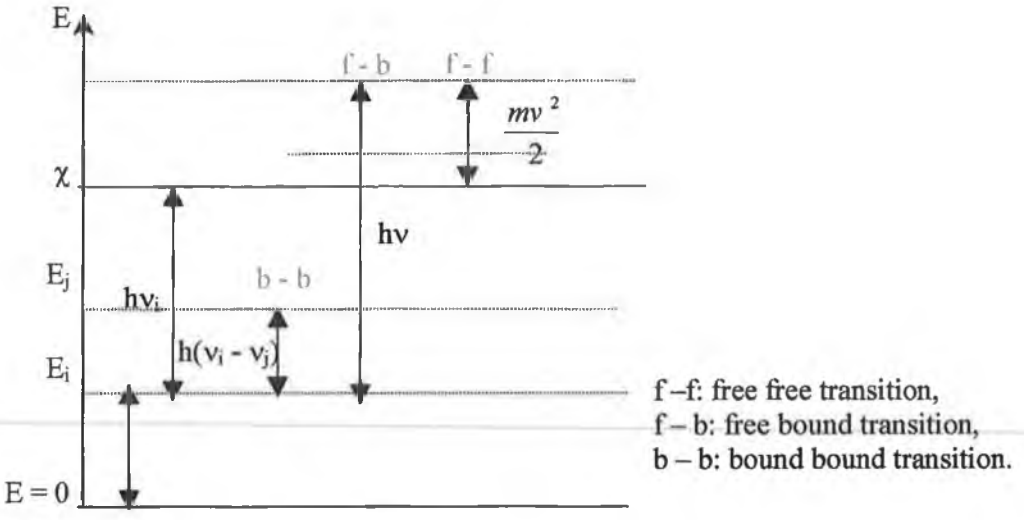

Figure 2.1: Radiation processes in plasmas.

2.2.1. Bound-bound transitions

Radiation emission due to bound-bound transitions occurs after an excited particle (atom or ion), makes a transition to a lower energy state by either radiative or collisional de-excitation. These transitions result in spectral lines whose profiles are dependent on the plasma parameters such as ion velocity, collision rate or perturbations due to magnetic or electric fields (Hughes 1975). Radiative excitation or photoexcitation occurs when an atom/ion absorbs a photon of defined energy and is promoted to a higher energy state. In a similar fashion photo de-excitation to a bound state followed by fluorescence leads to line emission, with a wavelength determined by the absorbed photon energy.

Collisional excitation occurs when an atom or ion in a defined energy state collides with another particle , i.e., atom, ion or electron, and it is promoted to a higher energy state. Collisions with electrons is a very important process in laser produced plasmas, and more efficient than collisions with other heavier particles (Colombant and Tonon 1973). The line spectrum due to de-excitation depends on the electron temperature and density, and the trend in emission tends towards shorter wavelengths as the plasma temperature increases. At high temperature the degree of ionization increases, reducing the screening of the nuclear charge. As a consequence, the energy difference between bounds states gets larger and the line emission tends towards higher photon energy.

Collisional deexcitation can also happen when a particle in an excited state loses energy to an electron during the collision. In this process no radiation is emitted and the energy is transferred to the electron kinetic energy.

2.2.2. Free-bound transitions

Radiation emission following a free-bound transition occurs when a free electron is capture by a n times ionized atom making a transition to a bound state of the n-1 times ionized atom. Since the electron is normally captured into an excited state, the excess energy gained by the atom can be emitted as a photon, this process is called recombination and the radiation emitted is referred to as recombination radiation. The emission spectrum is a continuum, whose profile depends on the velocity distribution of the electrons and the final bound state (Hughes 1975).

The reverse process is referred to as photoionization in which a bound electron in an atom of charge (Z-1)e absorbs a photon with an energy sufficiently large to ionize the atom and the electron is ejected into the continuum. We can write an energy balance equation valid for both recombination and its inverse process as:

$$h\upsilon=\frac{1}{2}mv^2+\chi_{Z-1}-E_i=\frac{1}{2}mv^2+h\upsilon_i \qquad [2.6]$$

where v is the velocity of the free electron, E_i is the energy level of the ion before absorption and ν_i is the minimum light frequency needed for the photoabsorption from level I and χ_{z-1} is the ionization potential of the atom of charge (Z-1)e.

2.2.3. Free-free transitions

Free-free transitions or Bremsstrahlung occurs when a free electron collides with another particle making a transition to a lower energy state by emitting a photon. Electron-ion collisions are the most effective for radiation emission, and the efficiency increases with the plasma temperature. Electron-electron collisions don't lead to radiation emission except at relativistic speed (Hughes 1975). The emission spectrum is a continuum.

The inverse process , i.e., inverse Bremsstrahlung is the dominant mechanism for laser light absorption during the plasma formation. In this case an electron in the electric field of an ion absorbs one photon resulting in an increase in its kinetic energy.

2.3. Equilibrium in plasmas

The relative importance of collisional and radiative processes occurring in a plasma determine its emission spectrum. The exact knowledge of the specific rate of all these processes would enable the prediction of the plasma emission spectrum, however their multiplicity and inter-dependence would lead to very complex models.
Depending on the plasma parameters , i.e., temperature, density, velocity, either collisional or radiative processes are dominant and appropriate models have been derived simplifying greatly the resolution of equations relating the different plasma parameters. We will discuss the three main plasma equilibrium models which are Local Thermodynamic Equilibrium (LTE), Collision Radiative Equilibrium and Coronal Equilibrium (Griem 1964, Lochte-Holtgreven 1995, Hughes 1975, Colombant and Tonon 1973).

2.3.1. Local Thermodynamic Equilibrium

As the plasma density increases, collisions within the plasma are more and more frequent. When the plasma density reaches a sufficient value, collisions are the dominant process, which determines the population of the different excited states.
Several conditions have to be fulfilled for the plasma to be considered as being in LTE;

- the electron and ion velocity distributions should follow a Maxwell Boltzmann distribution, which can be written as:

$$f(v)dv=4\pi n_e v^2\left(\frac{m_e}{2\pi k_B T_e}\right)^{\frac{3}{2}}\exp\left(-\frac{m_e v^2}{2k_B T_e}\right)dv \qquad [2.7]$$

here f(v)dv is the density of electrons with velocity between v and v + dv, n_e is the electron density and T_e the electron temperature.

- the plasma dimensions should be much smaller than the mean free path of the emitted photons but larger than the collision length of electrons and ions. If LTE is valid photons travel a long distance from their emission position and they can either escape from the plasma or be absorbed in another region of the plasma having a different temperature and density. As a consequence photons are not in equilibrium with each other whereas electrons and ions are, verifying the condition of charge neutrality in the plasma:

$$n_e = \sum_{i=0}^{z} iN_i \qquad [2.8]$$

where N_i the partial density of a charge state i.

- The electron density should reach a high enough value so that the ratio between collisional de-excitation and radiative decay should be larger than 10 to 1 for all transitions. An equivalent condition on the electron density has been derived by McWhirter (1965) for optically thin plasmas:

$$n_e \geq 1.6 \times 10^{12} T_e^{\frac{1}{2}} (\Delta E)^3_{\max} \qquad [2.9]$$

with n_e in cm^{-3}, and $(\Delta E)_{max}$ the largest interval between adjacent energy levels of atoms and ions in the plasma in eV. For an optically thick plasma, assuming that $0.8 \times \chi_e \geq (\Delta E)_{\max}$, the condition becomes:

$$n_e \geq 8.10^{11} T_e^{\frac{1}{2}} (\chi_e)^3_{\max} \qquad [2.10]$$

with $(\chi_e)_{max}$ the highest ionization energy of any atom or ion in the plasma.

2.3.2. Coronal Equilibrium

This equilibrium state is the complete opposite of the LTE model. This model applies to very low-density, optically thin plasmas, which are found in interstellar nebulae or the sun's corona; in laboratory experiments it applies to plasmas generated in tokamaks or low-density plasma machines. The corona model applies for very low ion and electron densities,

where the rate of collisional excitation is very low compared with the rate of spontaneous decay so that electrons in excited states decay to their ground state before the next collisional excitation occurs. As a consequence most ions in this equilibrium state are in their ground state and collisional excitation from the ground state balances the radiative decay from upper level to all lower energy levels.

In fact, the coronal model does not fully describe an equilibrium state since conserving processes such as three body recombination are smaller than energy dissipating processes such as radiative recombination. Every radiative recombination is followed by the emission of a photon causing the plasma to cool down and so only a steady state is reached.

2.3.3. Collisional Radiative Equilibrium (CRE)

The collisional radiative model defines an intermediate equilibrium between the Coronal and the LTE models. The CRE model tends to the Coronal model at low density and to the LTE model at high density. Here both collisional and radiative processes have to be taken into account. The conditions under which CRE prevails have been described by Colombant and Tonon (1973):

- Only collisions involving electrons, which are more efficient than collisions between heavy particles are considered, and the process of autoionization and its inverse process , i.e., dielectric recombination are neglected
- The velocity distribution of electrons has to be Maxwellian; this condition is satisfied when the electron-electron relaxation time is smaller than electron heating time. At high electron density the electron relaxation time is the smallest time characteristic in the plasma
- The population density of ions of charge Z+1 must not change dramatically when the quasi-steady-state population of ions of charge Z is being established
- The plasma must be optically thin to its own radiation so that the photon-ion interactions can be neglected

In figure 2.2, we show the different regions defined by the electron temperature and density where either of the three ionisation models prevails.

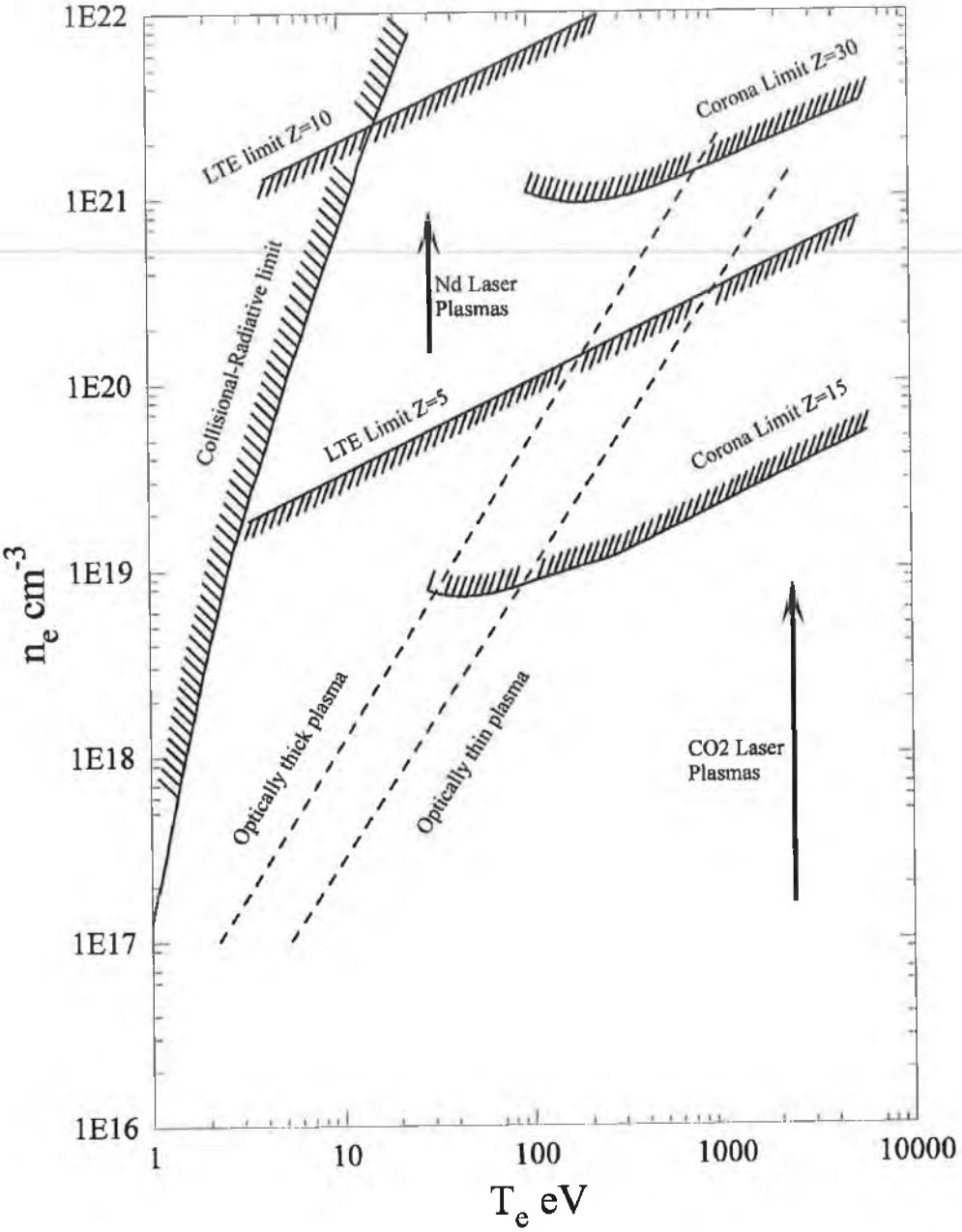

Figure 2.2. Criteria for the application of different ionisation models (after Colombant and Tonon 1973)

2.4. Radiation Transfer

In this section we will introduce the principal parameters needed to derive the equation of radiative transfer , i.e., the Einstein coefficients, the equivalent width, oscillator strength and the cross section of the transition under study. Since we are concentrating on measuring photoabsorption in atoms and ions with photon energies above the corresponding ionisation limits, we are effectively measuring total photoionisation, hence the equation will be solved only for the particular case of photoionisation. Finally, depending on the solution of the equation corresponding to specific plasma conditions, we will explain how we derive maps of column density directly from the experimental results.

2.4.1. Transition Probabilities

Consider a 2 level energy system (E_i and E_k) where $E_i < E_k$, with a population density of n_i and n_k respectively. The frequency ν associated with this transition is given by $h\nu = E_k - E_i$.

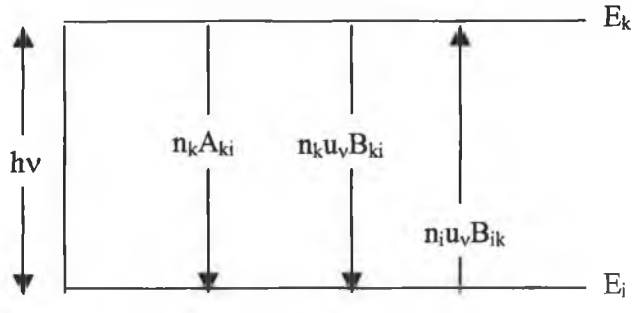

Figure 2.3. Transitions in a two levels energy system

We will consider three processes namely; spontaneous emission, stimulated emission and absorption. The transition probability for each of these processes depends on the population of each energy level and on the corresponding Einstein probability coefficients. The number of absorption processes per second per cm^3, under the influence of a radiation field with radiation density u_ν can be written as (Lochte-Holtgreven 1995):

$$N_{ik} = n_i u_\upsilon B_{ik} \qquad [2.11]$$

with n_i the population density of level i, B_{ik} the Einstein coefficient for absorption and u_ν the energy density of the radiation of the transition line at frequency ν. Here u_ν is taken to be constant in the region of the transition.

In a similar fashion, the number of emission processes per second per cm^3 can be written as:

$$N_{ki} = n_k u_\upsilon B_{ki} + n_k A_{ki} \qquad [2.12]$$

with n_k the population density of level k, B_{ki} the stimulated emission coefficient and A_{ki} the spontaneous emission coefficient for transitions between the upper level k and the lower level i. Assuming thermodynamic equilibrium, the principle of detailed balance applies, i.e., transitions from upper to lower levels occur at the same rate as transitions from lower to upper energy levels. It is then possible to relate the emission and absorption rates:

$$N_{ik} = N_{ki} \qquad [2.13]$$

Since we assumed thermodynamic equilibrium the population densities n_i and n_k are related by Maxwell-Boltzmann distribution:

$$\frac{n_i}{n_k} = \frac{g_i}{g_k} \exp\left(\frac{h\upsilon}{k_b T}\right) \qquad [2.14]$$

with g_i and g_k the statistical weights of the energy levels i and k respectively.
The energy density can be written as (Brehm and Mullin 1989):

$$u_\upsilon = \frac{8\pi h\upsilon^3}{c^3\left(\exp\left(\frac{h\upsilon}{k_b T}\right)-1\right)} \qquad [2.15]$$

We can now replace the terms in equation [2.12] by their specific values:

$$n_k \frac{g_i}{g_k} \exp\left(\frac{h\upsilon}{K_b T}\right) u_\upsilon B_{ik} = n_k u_\upsilon B_{ki} + n_k A_{ki} \qquad [2.16]$$

Therefore:

$$u_\upsilon = \frac{A_{ki}}{\frac{g_i}{g_k} \exp\left(\frac{h\upsilon}{K_b T}\right) B_{ik} - B_{ki}} \qquad [2.17]$$

Or in another form:

$$u_\upsilon = \frac{A_{ki}}{B_{ik} \frac{g_i}{g_k}\left(\exp\left(\frac{h\upsilon}{K_b T}\right) - \frac{g_k}{g_i}\frac{B_{ki}}{B_{ik}}\right)} = \frac{8\pi h\upsilon^3}{c^3\left(\exp\left(\frac{h\upsilon}{K_b T}\right) - 1\right)} \qquad [2.18]$$

This expression has to be valid for all temperatures to satisfy the principle of detailed balance, we have then:

$$B_{ik} = \frac{c^3}{8\pi h\upsilon^3} \frac{g_k}{g_i} A_{ki} \qquad [2.19]$$

and

$$g_i B_{ik} = g_k B_{ki} \qquad [2.20]$$

We can relate the Einstein coefficient for absorption B_{ik} to the oscillator strength or f-value of the same transition. The f-value corresponds to the fraction of energy of the classical oscillator assigned to a given transition and is related to the coefficient B_{ik} by (Corney 1977):

$$f = f_{ik} = \frac{2\varepsilon_0 m_e h\upsilon}{\pi e^2} B_{ik} \qquad [2.21]$$

Finally we define the integral of the total absorption cross-section for the same transition.

Assuming a radiation beam of intensity I_ν filling a solid angle $d\Omega$, the power absorbed by an atom is:

$$P_{abs} = h\upsilon N_{ik} = h\upsilon B_{ik}\left(\frac{4\pi}{c}\right) I_\upsilon \frac{d\Omega}{4\pi} \qquad [2.22]$$

Then

$$P_{abs} = I_\upsilon \frac{\pi e^2}{2\varepsilon_0 m_e c} f_{ik} d\Omega \qquad [2.23]$$

The power absorbed can also be written as a function of the total absorption cross section:

$$P_{abs} = I_\upsilon d\Omega \int_0^\infty \sigma_\upsilon d\upsilon \qquad [2.24]$$

We have then a relationship between the integral of the total absorption cross section and the f-value, which reads:

$$\int_0^\infty \sigma_\upsilon d\upsilon = \frac{\pi e^2}{2\varepsilon_0 m_e c} f_{ik} \qquad [2.25]$$

From this equation we can extract an expression for the total absorption cross section:

$$\sigma_\upsilon = \frac{\pi e^2}{2\varepsilon_0 m_e c} \frac{df_{ik}}{d\upsilon} \qquad [2.26]$$

for absorption resonances where $\frac{df_{ik}}{d\upsilon}$ is the differential oscillator strength. This formula can be approximated by introducing an appropriate line shape function g(ν):

$$\sigma_\upsilon = \frac{\pi e^2}{2\varepsilon_0 m_e c} f_{ik} g_\upsilon \qquad [2.27]$$

The above expression will be used for the derivation of the solution of the equation of radiative transfer and more specifically in the expression of the equivalent width.

2.4.2. The equation of radiative transfer

The equation of radiative transfer will be derived by considering a collimated beam of radiation passing through a cylindrical volume of a laser produced plasma. The beam is contained in a small solid angle dΩ(Corney 1977).

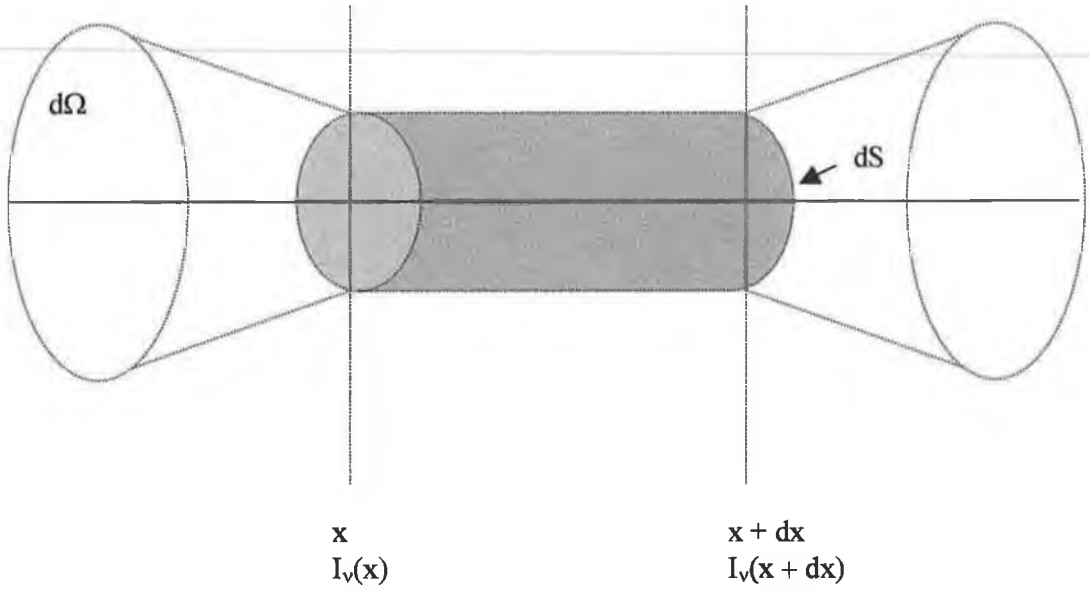

Figure 2.4. Geometric element considered for the derivation of the radiative transfer equation for a light beam of solid angle dΩ

We consider here the Einstein coefficient for absorption given in its intensity form, and defined by the relation:

$$N_{ik} = B_{ik}u_\nu = B^{J}_{ik}I_\nu \qquad [2.28]$$

The intensity I_ν and the radiation density u_ν of a given radiation field are related by the following expression:

$$I_\upsilon = \frac{c}{4\pi}u_\upsilon \qquad [2.29]$$

We express now the change in the radiation intensity at frequency between ν and ν + dν between x and x + dx, in a cylinder of cross section dS, for a time interval dt:

$$\left(I_\upsilon(x+dx)-I_\upsilon(x)\right)dSd\upsilon d\Omega dt=\frac{dI_\upsilon(x)}{dx}dxdSd\upsilon d\Omega dt \qquad [2.30]$$

This quantity corresponds to the difference between the energy emitted and the energy absorbed during the same time interval dt.

Considering a transition between two energy levels i and k with $E_i < E_k$, the energy emitted either by spontaneous or stimulated emission from level k can be written as:

$$E_{emitted}=h\upsilon n_k A_{ki} g_\upsilon dSd\upsilon dxdt\frac{d\Omega}{4\pi}+h\upsilon n_k B^{I}{}_{ki} g_\upsilon dSd\upsilon dxdt\frac{d\Omega}{4\pi}I_\upsilon \qquad [2.31]$$

The energy absorbed corresponds to the energy of a single photon multiplied by the number of transitions occurring from level i to level k during a time interval dt. If n_i is the population density of level i then:

$$E_{absorbed}=h\upsilon n_k B^{I}_{ik} g_\upsilon dSd\upsilon dxdt\frac{d\Omega}{4\pi}I_\upsilon \qquad [2.32]$$

The function g_ν is the line shape function for the transition of interest. It has to be introduced since the Einstein coefficients are frequency averaged and if transition rates induced by monochromatic light are needed the Einstein coefficients have to be multiplied by the appropriate normalised line shape function.

The equation of radiative transfer relates the difference in intensity between x and x + dx, to the difference between the energy absorbed and emitted, and it can be written as:

$$\frac{dI_\upsilon}{dx}=\frac{h\upsilon}{4\pi}\left(A_{ki}n_k+\left(B^{I}_{ki}n_k-B^{I}_{ik}n_i\right)I_\upsilon\right)g_\upsilon \qquad [2.33]$$

or

$$\frac{dI_\upsilon}{dx}=\varepsilon_\upsilon-K_\upsilon I_\upsilon \qquad [2.34]$$

where ε_υ is the volume emission coefficient and K_υ is the volume absorption coefficient defined by:

$$\varepsilon_\upsilon = \frac{h\upsilon}{4\pi} A_{kl} n_k g_\upsilon \qquad [2.35]$$

and

$$K_\upsilon = \frac{h\upsilon}{4\pi} B^I_{ik} n_i \left(1 - \frac{g_i n_k}{g_k n_i}\right) g_\upsilon \qquad [2.36]$$

The equation of radiative transfer is presented here in its general form. We will now derive the equation not for a transition between bound states but for the process of photoionisation.

2.4.3. A solution of the radiative transfer equation for photoionisation

2.4.3.1 Equation of radiative transfer

In this work we used quasi-monochromatic light to probe the different sample plasmas. In the prototype system used at the Rutherford Appleton Laboratory (RAL) – Central Laser Facility (described in chapter 3), we used a slowly diverging beam but retained spatial resolution mainly determined by the size of the pixels on the detector. In the final set-up in the DCU laboratory, (described in the second part of chapter 3), we use a collimated tuneable VUV monochromatic beam as a probe of cross section 4 mm by 4 mm, so that for both systems the derivation of the equation of radiative transfer is valid.

When dealing specifically with photoionisation a few simplifications can be made to equation [2.33]. First of all we can neglect the term due to spontaneous emission, since here we are not dealing with a bound-bound transition, the light absorbed leads to the emission of electrons almost exclusively. Stimulated emission due to fluorescence can be neglected as well since the branching ratio for fluorescence to electron emission processes tends to be less than 10^{-4} (Schmidt 1992).

We can then write the "simplified" equation:

$$\frac{dI_\upsilon(x)}{dx} = -K_\upsilon I_\upsilon(x) \qquad [2.37]$$

with a straightforward solution, when integrating between 0 and x:

$$I_\upsilon(x) = I_\upsilon(0)\exp(-K_\upsilon x) \qquad [2.38]$$

Since we neglect the term due to stimulated emission here, we also have a simplified expression for K_ν:

$$K_\upsilon = \frac{h\upsilon}{4\pi} n_i g_\upsilon B_{ik}^l = \frac{\pi e^2}{2\varepsilon_0 m_e} n_i f_{ik} g_\upsilon \qquad [2.39]$$

and as a function of the photoionisation cross section:

$$K_\upsilon = \frac{\pi e^2}{2\varepsilon_0 m_e} n_i f_{ik} g_\upsilon = \sigma_\upsilon n_i \qquad [2.40]$$

The volume absorption coefficient K_ν is expressed here as a function of the total absorption cross section since it is the latter quantity that has been measured previously for the calcium and barium ions studied in this work (Lyon *et al.* 1986, 1987).

2.4.3.2 Equivalent width

We introduce here the concept of equivalent width W_ν, which corresponds to the width of a rectangle having the same area as the absorption line. This concept is described graphically in figure 2.5.

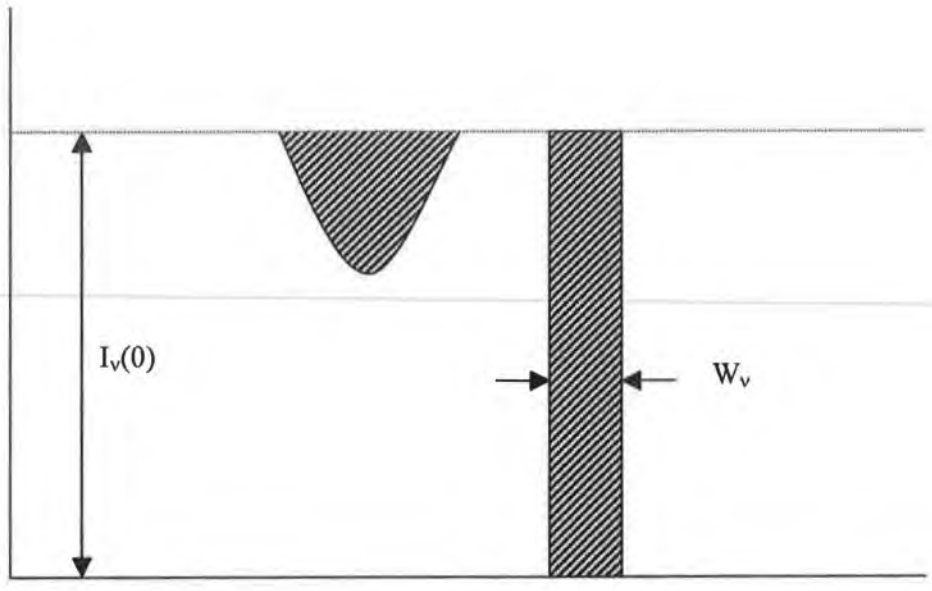

Figure 2.5. Schematic definition of the equivalent width (after Corney 1977)

The equivalent width is related to the transmitted intensity by the following equation:

$$W_\upsilon I_\upsilon(0) = \int (I_\upsilon(0) - I_\upsilon(x)) d\upsilon \qquad [2.41]$$

The equivalent width has to be introduced here since experimentally we are not measuring I_ν directly, but the integral of I_ν over a bandwidth determined by the linear dispersion of the monochromator. It has been shown that within this bandwidth, typically ~ 0.1 nm, $I_\nu(0)$ can be considered to be constant for laser plasma continua (Kiernan 1994). Equation [2.41] can be written as:

$$W_\upsilon = \int \left(1 - \frac{I_\upsilon(x)}{I_\upsilon(0)}\right) d\upsilon \qquad [2.42]$$

Using the solution of the equation of radiative transfer $I_\upsilon(x) = I_\upsilon(0)\exp(-K_\upsilon x)$, we can write:

$$W_\upsilon = \int\left(1\text{-}\exp\left(\text{-}K_\upsilon x\right)\right)d\upsilon \qquad [2.43]$$

Considering an absorbing plasma of length L, depending on the opacity conditions in the plasma we can isolate three different cases; when the plasma is optically thin , i.e., $K_\nu L$ is much smaller than 1, when $K_\nu L$ can no longer be assumed to be much smaller than unity and finally when the plasma is optically thick and the ion density n_i is very large.

2.4.3.3 Optically thin plasmas

We consider now, an absorbing plasma column of length L. The equivalent width reads:

$$W_\upsilon = \int\left(1\text{-}\exp\left(\text{-}K_\upsilon L\right)\right)d\upsilon \qquad [2.44]$$

For an optically thin plasma the product $K_\nu L$ tends to zero and the 1st order limited development of the exponential function at 0 gives us $1 - K_\nu L + 0(\nu)$, where $0(\nu)$ is a negligible function of ν. Substituting into the equation we have:

$$W_\upsilon = \int K_\upsilon L d\upsilon = \int \frac{\pi e^2}{2\varepsilon_0 m_e} n_i L f_{ik} g_\upsilon d\upsilon \qquad [2.45]$$

Since the line shape function g_ν is the only function dependent on ν, we can take the other values outside the integral and since the function g is normalised over the considered bandwidth we have then $\int g(\upsilon)d\upsilon = 1$, and hence we can write the equivalent width as

$$W_\upsilon = \frac{\pi e^2}{2\varepsilon_0 m_e} n_i f_{ik} L \qquad [2.46]$$

We have here a simple linear relation between the equivalent width and the column density n_iL. Given a map of equivalent width values of the expanding plasma plume, and knowing the transition oscillator strength f_{ik}, it is then straightforward to convert it to a map of column density. We introduce the total absorption cross section into the previous relation since we are using this value for the analysis in the next section.
From equation [2.26]:

$$\sigma_\upsilon = \frac{\pi e^2}{2\varepsilon_0 m_e c} f_{ik} g_\upsilon$$

Substituting in the expression for W_ν:

$$W_\upsilon = \int K_\upsilon L d\upsilon = \int n_i L \sigma_\upsilon d\upsilon = n_i L \int \sigma_\upsilon d\upsilon \qquad [2.47]$$

assuming that n_i and L are independent of ν. By choosing a transition where the integral of the total absorption cross section is known, we can convert maps of equivalent width directly into maps of column density n_iL using a simple division:

$$n_i L = \frac{W_\upsilon}{\int \sigma_\upsilon d\upsilon} \qquad [2.48]$$

2.4.3.4 Non-optically thin plasmas

In the case of a non-optically thin plasma where $K_\nu L \sim 1$ it is not possible to expand the exponential function at zero. We have to take into consideration the complete expression of the equivalent width which is:

$$W_\upsilon = \int \left(1-\exp\left(-K_\upsilon L\right)\right) d\upsilon \qquad [2.49]$$

We still assume here that I_ν is constant over the defined bandwidth, and write the expression of W_ν as a function of the total absorption cross section σ_ν:

$$W_\upsilon = \int_{\Delta\upsilon}\left(1-\exp\left(-K_\upsilon L\right)\right)d\upsilon = \int_{\Delta\upsilon}\left(1-\exp\left(-n_i L\int_{\Delta\upsilon}\sigma_\upsilon d\upsilon\right)\right)d\upsilon \qquad [2.50]$$

Here again it is possible to calculate the value of W_ν for every value of n_iL if the value of the integral over the bandwidth of the absolute cross section is known. The expression for W_ν becomes then;

$$W_\upsilon = \int_{\Delta\upsilon}(1-\exp(-n_i LC))d\upsilon \qquad [2.51]$$

with $C = \int\sigma(\upsilon)d\upsilon$.

In this way a table of values of equivalent width is constructed for each value of n_iL. It is then straightforward to plot a curve of n_iL as a function of W_ν. By fitting a polynomial to this function, i.e., $n_iL = f(W_\nu)$ we can convert maps of equivalent width obtained experimentally into maps of column density n_iL. This expression will be used in the analysis section of this work, the constant C being calculated using the experimental results of Lyon *et al.*.(1986, 1987) for Ca^+ and Ba^+. Using the best polynomial fit to the curve, maps of equivalent width obtained experimentally will be converted directly into maps of column density.

2.4.3.5 Optically thick plasmas

For a high density regime a square root dependence between W_ν and n_iL can be obtained (Corney 1977), assuming a Lorentzian profile for the absorption coefficient K_ν and a Gaussian profile for the incident radiation I_ν:

$$W_\upsilon = \left(\frac{\pi e^2 f_{ik} n_i L\Gamma}{\varepsilon_0 mc}\right)^{\frac{1}{2}} \qquad [2.52]$$

where Γ is the Lorentzian line width parameter.

In the present work, such a high-density regime in the absorbing plasma will not be reached and we will show in Chapter 4 that we cannot assume to be in an optically thin condition either. Thus, we will use the general expression of the equivalent width , i.e., K_ν close to

unity, for the data analysis. During the experiment we measure the equivalent width in wavelength units so that in chapter 4 the data analysis is carried out using the following expression:

$$W_\lambda = \int_{\Delta\lambda}\left(1-\exp\left(-n_i L \int_{\Delta\lambda}\sigma_\lambda d\lambda\right)\right)d\lambda \qquad [2.53]$$

and the equivalent width will be expressed in nanometers.

2.5. Plasma dynamics: The Singh and Narayan model

In this section a description of the 3 dimensional plasma plume expansion model developed by R. K Singh and J. Narayan (1990) is given. From the experimental data we are able to extract time and space resolved column density maps as well as plasma plume front velocities, which we compare with the simulation results. Other information (ion or electron temperature) on the plasma parameters, which could not be measured using our experimental apparatus, will be derived directly from the simulations. The model was written to simulate the phenomenon of pulsed laser evaporation for the deposition of thin films. The model distinguishes three phases in the process; first the interaction of the laser beam with the target surface, the interaction of the laser beam with the evaporated material and an adiabatic expansion in vacuum. We will explain in some detail these three successive phases.

2.5.1. Interaction of the laser beam with the target surface

Depending on the on target laser irradiance, melting and/or evaporation occur at the target surface. These thermal effects have been studied in detail and can be explained by the solution of a one dimensional heat flow equation with adequate boundary conditions. These conditions have to account for the phase change at the surface of the target knowing that thermal evolution depends on several parameters such as the laser energy, wavelength, pulse length and shape as well as the thermophysical properties of the target material. The solution to this problem is complicated by the motion of the laser target interface which follows the melting of the surface, and by the variation of the optical and material properties with time and temperature, so that numerical solutions have to replace the classic

analytical approach. At the end of this phase it is important to know the amount of material that has evaporated. Assuming energy deposited by the laser on the target is equal to the energy required to vaporise the surface, and taking into account the conduction losses by the substrate and the absorption losses by the plasma, we can derive an expression for the thickness of evaporated material Δx:

$$\Delta x = \frac{(1-R)(E-E_{th})}{(\Delta H + C_v \Delta T)} \qquad [2.54]$$

where R is the reflectivity of the target surface, ΔH is the latent heat, C_v is the heat capacity at constant volume and ΔT is the maximum temperature rise. E_{th} is dependent on the laser energy and represents the minimum energy above which evaporation is observed. This relation is true only if the thermal diffusion distance is greater than the absorption length of the laser light in the target material.

2.5.2. Laser beam interaction with evaporated material

The primary laser energy absorption mechanism is due to electron and ion collisions through inverse Bremsstrahlung. Introducing the absorption coefficient α, laser radiation is highly absorbed if the value of the product αL is large, L being the plasma dimension in the plane perpendicular to the target surface.

However since α is proportional to the plasma density the strongest absorption occurs near the target surface and the subsequent heating of the evaporated material is strongly related to its value. In turn, the density of particles in the early phase of the plasma depends on the ionisation degree, the evaporation rate and the plasma expansion velocity. From a very dense plasma located near the target surface, the plasma expands very rapidly outwards causing the ion and electron density to decrease swiftly and the plasma to be transparent to laser radiation. On the other hand, evaporation is still taking place and evaporated material is being added to the plasma so that there is always a thin layer of dense plasma between the bulk of the target and the plasma front edge that is absorbing laser light. The laser-target interaction region can then be divided into 4 sub-regions shown in figure 2.6.

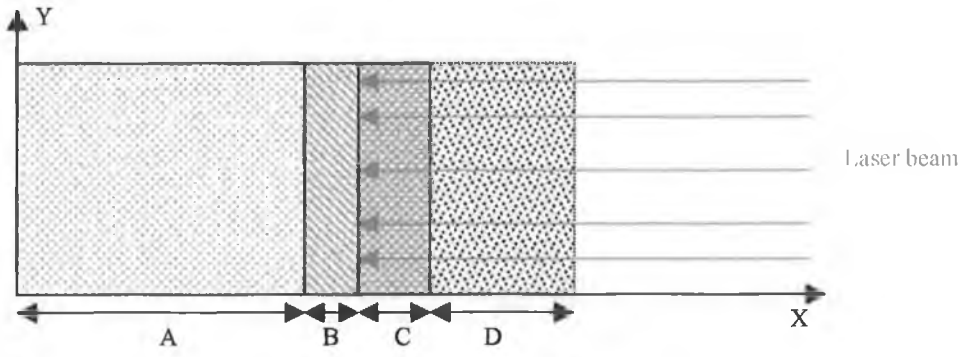

Figure 2.6. Schematic diagram showing the 4 different phases in plasma expansion

On the schematic drawing region A corresponds to the unaffected bulk target, region B shows the evaporated target material, region C is composed of the dense plasma absorbing laser radiation and region D corresponds to the expanding plasma transparent to the laser radiation.

During the laser pulse a dynamic equilibrium exists between the plasma absorption coefficient α and the fast transfer from thermal to kinetic energy, so that a self-regulating regime is created at the target surface (region C). As the thermalisation time is much smaller than the plasma expansion time, and since the plasma only occupies a small volume, radiation losses are negligible and it is legitimate to assume an isothermal and uniform regime. In summary, during the duration of the laser pulse, the plasma in region D is expanding isothermally perpendicularly from the target, while the region C of the plasma is constantly absorbing laser light.

The plasma expansion occurs very quickly due to large density gradients. The plasma can then be simulated as a high-pressure, high temperature gas suddenly allowed to expand in vacuum. In the early stages of the plasma formation, the density is very high so that the mean free path is very short and the plasma behaves as a continuum fluid and hence the gas dynamic equation can be applied.

The density n can be written as a Gaussian function at any time $t < \tau$:

$$n(x,y,z,t) = \frac{N_T t}{\sqrt{2}\pi^{\frac{3}{2}}\tau X(t)Y(t)Z(t)} \times \exp\left(-\frac{x^2}{2X(t)^2} - \frac{y^2}{2Y(t)^2} - \frac{z^2}{2Z(t)^2}\right) \quad [2.55]$$

where N_T is the number of particles evaporated at the end of the laser pulse τ, and X(t), Y(t), Z(t) are the dimensions of the expanding plasma. The density profile, even though assumed as Gaussian here, should be dependent on the degree of excitation , i.e., on the specific heat ratio γ. The plasma being treated as an ideal gas, the pressure P is related to the density n by the ideal gas equation:

$$P = nkT_0 = n(x,y,z,t)kT_0$$

$$P = \frac{N_T tkT_0}{\sqrt{2}\pi^{\frac{3}{2}}\tau X(t)Y(t)Z(t)} \times \exp\left(-\frac{x^2}{2X(t)^2} - \frac{y^2}{2Y(t)^2} - \frac{z^2}{2Z(t)^2}\right) \qquad [2.56]$$

where T_0 is the isothermal temperature of the plasma.

For the density to retain a Gaussian profile, Dawson (1964) showed that the velocity should be proportional to the distance from the target, therefore the velocity v can be written as:

$$\vec{v}(x,y,z,t) = \frac{x}{X(t)}\frac{dX(t)}{dt}\vec{i} + \frac{y}{Y(t)}\frac{dY(t)}{dt}\vec{j} + \frac{z}{Z(t)}\frac{dZ(t)}{dt}\vec{k} \qquad [2.57]$$

where $\frac{dX(t)}{dt}, \frac{dY(t)}{dt}, \frac{dZ(t)}{dt}$ are the expansion velocities of the plasma edges.

The equation of dynamics describing the plasma expansion are; (i) the equation of continuity, (ii) the equation of motion and (iii) the equation of energy, which isn't solved here since a constant and uniform temperature is assumed.

The equation of continuity is given by:

$$-\frac{\partial}{\partial t}\int_V \rho dV = \int_S \rho\left(\vec{v}.\vec{N}\right)dS - \frac{\partial}{\partial t}\frac{mN_T t}{\tau} \qquad [2.58]$$

where V is the volume, S the surface enclosing V, dS, dV are respectively the differential surface and volume elements, N is the unit normal vector, ρ the density and m the mass of the atomic species. The equation of motion is:

$$\int_V \left(\rho \frac{\partial \vec{v}}{\partial t} + \vec{v} \frac{\partial \rho}{\partial t} + \rho \left(\vec{v}.\nabla \right) \vec{v} + \vec{v} \left(\vec{v}.\nabla P \right) + \rho \vec{v} \left(\nabla.\vec{v} \right) + \nabla P \right) dV = 0 \qquad [2.59]$$

To solve these equations we replace the pressure P, the velocity v and the density n by their values given in equations [2.55], [2.56], [2.57]. The solution for $t < \tau$ is then:

$$X(t)\left(\frac{1}{t}\frac{dX}{dt} + \frac{d^2X}{dt^2} \right) = Y(t)\left(\frac{1}{t}\frac{dY}{dt} + \frac{d^2Y}{dt^2} \right) = Z(t)\left(\frac{1}{t}\frac{dZ}{dt} + \frac{d^2Z}{dt^2} \right) = \frac{kT_0}{M} \qquad [2.60]$$

This solution describes the initial plasma expansion during the laser pulse. The dimensions of the plasma on the target plane are of the order of a few hundred microns whereas in the direction perpendicular to the target the dimensions are only a few microns. At the end of the laser pulse, during the adiabatic expansion in vacuum, as the velocity is controlled by pressure gradients, the velocity in the direction perpendicular to the target is greater than in the other directions explaining the elliptical shape of the plasma.

2.5.3. Adiabatic expansion in vacuum

At the end of the laser pulse the plasma expands adiabatically so that its dimension can be related to the plasma temperature by $TV^{\gamma-1} = C$ or:

$$T\left(X(t)Y(t)Z(t) \right)^{\gamma-1} = C \qquad [2.61]$$

Here γ is the ratio of the specific heat capacities at constant pressure and volume and C is a constant.

During the adiabatic expansion, the thermal energy is rapidly converted into kinetic energy increasing constantly the plasma expansion velocity. As the laser pulse is terminated there are no more particles being introduced in the system so that the ratio t/τ can be neglected and we can then write the expression for the velocity, the pressure and the density as we did for the isothermal expansion phase ($t < \tau$):

$$\vec{v}(x,y,z,t)=\frac{x}{X(t)}\frac{dX(t)}{dt}\vec{i}+\frac{y}{Y(t)}\frac{dY(t)}{dt}\vec{j}+\frac{z}{Z(t)}\frac{dZ(t)}{dt}\vec{k}$$

$$P=nkT_0=n(x,y,z,t)=\frac{N_T kT_0}{\sqrt{2}\pi^{\frac{3}{2}}X(t)Y(t)Z(t)}\times\exp\left(-\frac{x^2}{2X(t)^2}-\frac{y^2}{2Y(t)^2}-\frac{z^2}{2Z(t)^2}\right) \quad [2.62]$$

$$n(x,y,z,t)=\frac{N_T}{\sqrt{2}\pi^{\frac{3}{2}}X(t)Y(t)Z(t)}\times\exp\left(-\frac{x^2}{2X(t)^2}-\frac{y^2}{2Y(t)^2}-\frac{z^2}{2Z(t)^2}\right)$$

Here the equation of energy has to be solved since we are not in a uniform isothermal regime any more, and the adiabatic equation of state must be solved. The adiabatic equation of state is given by:

$$\frac{1}{P}\left(\frac{\partial p}{\partial t}+\vec{v}.\nabla P\right)-\frac{\gamma}{n}\left(\frac{\partial n}{\partial t}+\vec{v}.\nabla n\right)=0 \quad [2.63]$$

and the equation of energy is given by:

$$\frac{\partial T}{\partial t}+\vec{v}.\nabla T=(1-\gamma)T\nabla.\vec{v} \quad [2.64]$$

By replacing the values of P, n, and v in equations [2.58], [2.59], [2.63], [2.64], the solution describing the adiabatic expansion of the plasma can be written as:

$$X(t)\left(\frac{d^2X}{dt^2}\right)=Y(t)\left(\frac{d^2Y}{dt^2}\right)=Z(t)\left(\frac{d^2Z}{dt^2}\right)=\frac{kT_0}{M}\left(\frac{X_0Y_0Z_0}{X(t)Y(t)Z(t)}\right)^{\gamma-1} \quad [2.65]$$

X_0, Y_0, Z_0 are the initial plasma size at the end of the laser pulse.

From the equation we deduce that the acceleration depends on the temperature, the plasma dimensions and the mass of the different species constituting the plasma. Since the expansion model is based on fluid flow it applies to all plasma species collectively. Here again the transverse dimensions are larger than the dimension perpendicular to the target

surface, as the velocity depends on these parameters and as the highest velocity corresponds to the smallest dimension, the velocity in the direction perpendicular to the target is larger explaining the oblong shape of the plasma even after the termination of the laser pulse.
The two equations describing the plasma expansion before and after the termination of the laser pulse are solved numerically using the Runge Kutta method, with small time steps (0.01 picosecond) during the duration of the laser pulse to 100 picosecond and then 1 ns steps for the adiabatic expansion in vacuum. The program used to solved the equation was written by Whitty (1998)

2.6. Summary

We introduced the basic processes in plasma formation and the different equilibrium conditions found in laser produced plasmas.
The equation of radiative transfer is derived and solved for the specific case of photoionisation. The concept of equivalent width is introduced here. Indeed values of equivalent width can be calculated directly by a simple ratio between the different images recorded experimentally. The equivalent width is related to the column density NL by the following equation:

$$W_\lambda = \int_{\Delta\lambda}\left(1-\exp\left(-n_i L \int_{\Delta\lambda}\sigma_\lambda d\lambda\right)\right)d\lambda$$

and can be used to in turn calculate values of column density.
Finally, the laser plasma expansion model derived by Singh and Narayan (1991) is described here and will be used in chapter 4 to compare experimental plume expansion velocity with the code predictions.

Chapter 3

Experimental systems

3. Introduction

During the course of the work described in this thesis two different experimental systems involving normal incidence (RAL) or normal plus grazing incidence (DCU) optical systems were used.

For spectroscopic studies in the XUV region, spectrometers equipped with spherical concave gratings operating at grazing incidence are ideally suited due to the high reflectivity of optical surfaces at these angles of incidence. Concave gratings combine the focusing properties of a spherical surface and the dispersive properties of a ruled surface. Rowland (1882, 1883) stated that if such a grating were placed tangentially to a circle of diameter equal to the radius of curvature of the grating so that the grating centre lies on the circumference, the spectrum of an illuminated point on the circle would be focused on this circle. This is known as the Rowland circle. However, spherical gratings used at grazing incidence in the classical Rowland mount are near to completely astigmatic. To compensate for this severe astigmatism toroidal gratings can be used providing stigmatic conditions at one particular wavelength but suffering from large aberrations in both spatial and spectral directions. In 1959, Rense and Violet proposed to couple a toroidal mirror to the concave spherical grating to overcome astigmatism and study the emission spectrum of the Sun in the VUV wavelength range.

In the absence of a toroidal mirror, the spherical grating will focus the light from a source on the Rowland circle only in the meridional or tangential plane. The vertical focus will be located outside the Rowland circle. Thus to obtain a stigmatic image the source has to be imaged on the Rowland circle in the tangential and sagittal planes. By choosing the

radii of the toroidal mirror adequately a stigmatic image can be obtained for a given wavelength. The toroidal mirror has two functions, first to focus the astigmatic image of the light source onto the entrance slit of the spectrometer in the meridional plane and secondly to focus the astigmatic image in the sagittal plane on the Rowland circle defined by the grating parameters. Cantu and Tondello used this configuration in 1975 for the study and improvement of a triggered spark source in vacuum. Here the mirror was used both as a light collimator to increase the flux collection and to correct astigmatism. Later, with his co-workers he extended his investigations to the study of emission spectra of laser produced plasma (Tondello 1979, Malvezzi *et al.* 1981, Villoresi *et al.* 1994).

This particular optical configuration has been studied in detail by H.J. Shin *et al.* (1995), who carried out intensive ray tracing simulations to understand the variation of the system's spatial resolution. They showed that the spatial resolution is very high in the meridional plane but only in the stigmatic region. However the opposite trend is observed when moving away from the astigmatic region where the best resolution is obtained in the sagittal plane.

Villoresi *et al.* (2000) used a similar configuration except that the toroidal mirror was coupled to a toroidal grating operating in the Rowland circle configuration. This system was used for photoabsorption studies, where the continuum radiation of the first plasma was focused onto the sample plasma located at the entrance slit of the spectrometer. The toroidal mirror – toroidal grating optical configuration is shown in figure 3.1.

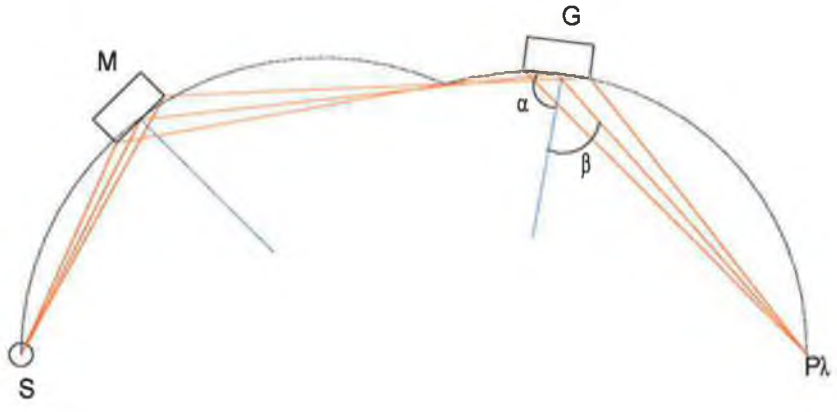

Figure 3.1. Optical configuration combining a toroidal grating (G) coupled to a toroidal mirror (M) (after Villoresi *et al.* 2000)

In the X-ray region, flat or spherical crystals have revealed themselves as efficient tools for spectroscopic and imaging experiments (Kieffer *et al.* 1989). Sanchez del Rio *et al.* (1999) used a spherical bent mica crystal to collimate and monochromate X-rays produced by short pulse laser produced plasma. Pikus *et al.* (2000) modified the well-established shadow monochromatic backlighting technique (Lewis and McGlinchey 1985), where the sample to be studied is placed between the crystal and the backlighting source. The crystal operates in the Rowland circle configuration but at an angle close to normal incidence to limit aberrations and retain high spatial resolution. The main drawback in this set-up is that the tangential and sagittal foci are not located at the same position thereby altering the shape of the object under study. In this modified set-up the detector is placed in order to ensure the same magnification in both planes. A spatial resolution of 4 microns was achieved for a spectral range of 0.1 nm to 1.8 nm. As an alternative to crystals, micro-channel plates and zone plates have been used as light collimators (Aota *et al.* 1997, Yamagushi *et al.* 1987) and as focusing elements (Wilkins *et al.* 1989, Kaaret *et al.* 1992, Folkard *et al.* 2001).

In the VUV wavelength range (30 nm to 100 nm) the surface reflectivity is still high enough to allow the use of normal incidence optics. Very few imaging system have been developed in this spectral region. We point out the work of Koog *et al.* (1996) who used a normal incidence monochromator identical to the one used in this work to develop an imaging system designed to carry out spatially resolved measurement of power losses and distributions of ions impurities in tokamak plasmas. The system consists of a concave grating working off Rowland circle at normal incidence (15° subtended angle), where astigmatism is greatly reduced compared with a grazing incidence configuration. Instead of using a focusing optic, here the imaging properties are achieved using the entrance slit (of finite width and height) as a pinhole. A schematic diagram of the optical set-up is shown in figure 3.2.

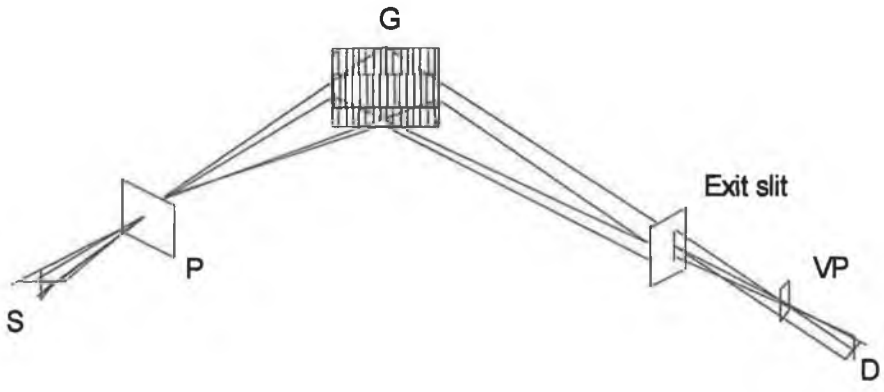

Figure 3.2. Optical set-up where S is the light source, P is a pinhole, G is the concave grating, VP is the focal point in the vertical plane and D is a CCD detector.

The distribution of C^{3+} ion impurities in the JIPP T-IIU tokamak has been measured using the emission line at 154.8 nm, and their relative position in the plasma plume has been recorded with a resolution of the order of a millimetre or so. The same experiments were repeated with oxygen and nitrogen impurities.

The optical system built in the DCU laboratory and described in this thesis is inspired by these previous optical configurations. The DCU built system combines toroidal mirrors working at grazing incidence and a normal incidence monochromator. The mirror located between the light source and the entrance slit of the monochromator acts as a focusing element to maximise flux collection in the system. Astigmatism, although present in this configuration, is reduced compared with monochromators operating at grazing incidence. Even though the location of the grating focal point is situated outside the Rowland circle in the sagittal plane the parameters of the exit mirror are calculated to account for the different locations of the two foci. The exit mirror acts as a light collimator delivering a parallel quasi-monochromatic beam.

The principle of the technique is similar to the DLP experimental set-up. Basically the VUV backlighting source is created in a vacuum chamber coupled to a mirror chamber housing a concave spherical mirror in the prototype set-up used at RAL and then upgraded to a toroidal mirror in the final design in DCU. The mirror focuses the VUV light onto the slit of a monochromator where the wavelength of the VUV radiation is tuned to the resonance line under study. On the exit arm of the system, the quasi-monochromatic beam is used to probe a sample plasma located in a second target chamber. The prototype set-up didn't contain any optical element on the exit arm and the diverging beam from the exit slit

was used to probe the sample plasma. The final design included a collimating toroidal mirror that illuminated the sample plasma with a parallel beam. In both systems the transmitted image or shadowgram was recorded on a CCD camera.

Both target chambers are fitted with target holders allowing movements in the x, y and z directions. On the source side this mount enables one to translate or rotate the target in order for the laser beam to interact with a fresh target area. On the sample side, space resolved photoabsorption images can be obtained by translating the absorbing plasma in and out of the probe beam.

The lasers being synchronised to one another, it is possible to insert a variable delay between the two laser pulses. Time resolved images can then be obtained with delay ranging from 10 nanoseconds to a few milliseconds with a jitter within $\pm$ 1 ns.

This chapter is divided into three main sections. Section 3.1 deals with general considerations relating to the ray tracing program, and introduces the basic equations of geometrical optics used to describe the individual optical components used during the ray tracing study. Section 3.2. describes the prototype system used at the Rutherford Appleton Laboratory and section 3.3 the final optical set-up implemented in the DCU laboratory.

3.1 The ray tracing code and geometrical optics considerations

3.1.1 The ray tracing code

LPS (Light Path Simulation) is a ray-tracing program written in FORTRAN 77 by Guiseppe Bonfante (1989). The program treats every ray of light in vectorial fashion, i.e., a vector "position" and a vector "direction" are attributed to each ray of light. Once a set of Cartesian co-ordinates (x, y, z) centred on the simulated light source is chosen one can define the parameters of the light source. Different types of sources can be selected between:

- A fan source which consists in a point source emitting a cone of light
- A box source which can be either square or rectangular
- A dot source which can be a point, a circular or elliptical source
- A Gaussian characterised by a Gaussian distribution of rays

For every type of source the dimensions, the beam divergence and the number of rays emitted have to be indicated. When the source is defined it can be translated along the x-

axis, onto the surface of an Optical Element (OE), which can be a mirror (plane, spherical, toroidal, parabolic…) or a grating (spherical or toroidal) with fixed or variable groove spacing. The parameters of the optical elements have to be indicated, i.e., radii of curvature, type of optic and number of grooves per millimetre for gratings. Once the light reaches the surface of the OE, the set of co-ordinates has to be rotated by an angle equal to the incidence angle + 90 degrees to match the plane defined by the OE surface. At this stage the illumination of the OE surface can be checked. The set of co-ordinates has to be rotated again with an angle equal and opposite to the incidence angle to give the direction of the reflected beam.

At any stage of the ray tracing the footprint of the beam can be visualised on a "screen", which is a plane surface perpendicular to the direction of propagation of the beam.

3.1.2 The concave diffraction grating

Although many studies have been carried out on the theory of the concave grating the main contributions remain from Rowland himself. Nonetheless, since then, Beutler (1945) and Namioka (1959), in particular, who used geometrical optics to demonstrate their theories, have added major contributions to Rowland's initial work (1882, 1883). The theory of the concave grating can be found in many reference textbooks, here we refer in particular to J. A. R. Samson (1967). In this section we will show how the grating equation as well as the equations giving the position of the horizontal and vertical foci are derived. A schematic illustrating image formation by a concave grating is shown in figure 3.3.

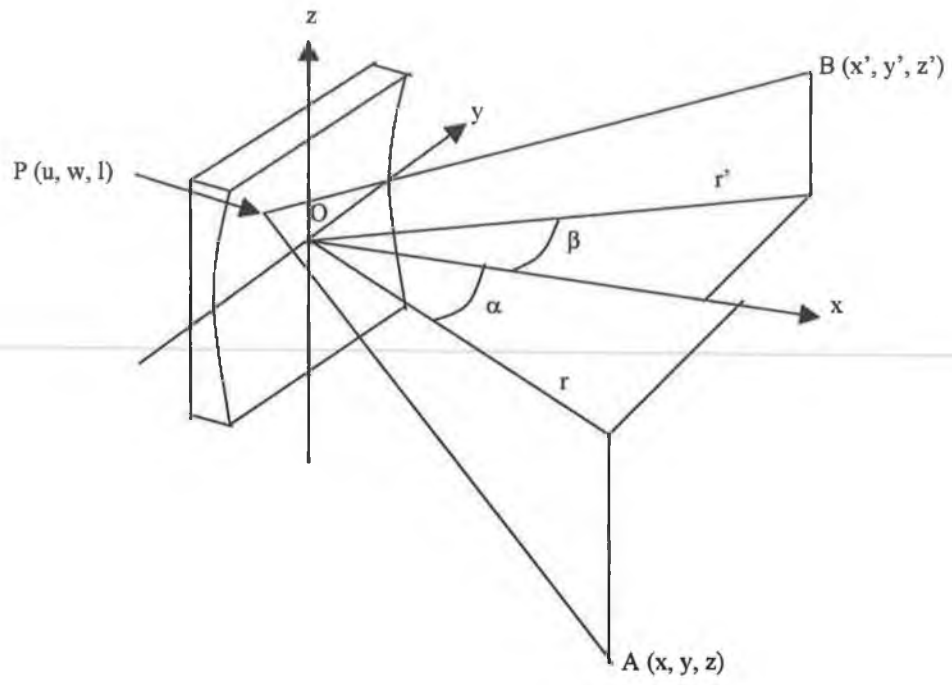

Figure 3.3. Image formation by a concave grating (after Samson 1967)

Let us assume that light travels from A through any point P on the grating surface and is focused on point B, then the light path function F can be written as:

$$F = AP + PB + \frac{wm\lambda}{d} \qquad [3.1]$$

where m is the spectral order, λ the light wavelength and d the groove spacing.
The distances AP and PB can be written as:

$$\begin{aligned} (AP)^2 &= (x-u)^2 + (y-w)^2 + (z-l)^2 \\ (BP)^2 &= (x'-u)^2 + (y'-w)^2 + (z'-l)^2 \end{aligned} \qquad [3.2]$$

By rewriting these expressions in cylindrical co-ordinates and applying Fermat's principle of least time (B being located such that F will be either maximum or minimum for any point P), we have:

$$\frac{\partial F}{\partial l} = 0$$
$$\frac{\partial F}{\partial w} = 0 \qquad [3.3]$$

Combining Fermat's principle with the expression for the light path of equation [3.1], we derive the positions of the horizontal and vertical foci of the concave grating. For the horizontal or primary focus:

$$\frac{\cos^2(\alpha)}{p} + \frac{\cos^2(\beta)}{q} = \frac{\cos(\alpha)+\cos(\beta)}{R} \qquad [3.4]$$

where p is the object to grating distance, q is the image to grating distance, and R is the radius of curvature of the grating.
For the vertical or secondary focus:

$$\frac{1}{r'} = \frac{\cos(\alpha)+\cos(\beta)}{R} - \frac{1}{r} \qquad [3.5]$$

Using Fermat's conditions we can also derive the grating equation for the central ray AOB shown in figure 3.3.

$$\left(1+\frac{z^2}{r^2}\right)^{-\frac{1}{2}} (\sin\alpha + \sin\beta) = \frac{m\lambda}{D} \qquad [3.6]$$

In practice the ratio $\frac{z^2}{r^2} << 1$, so the equation simplifies to the well-known equation of the concave grating:

$$(\sin\alpha + \sin\beta) = \pm\frac{m\lambda}{D} \qquad [3.7]$$

These equations will be used in the ray tracing of the two optical systems, especially for the simulation of the concave grating, since the program requires the values of the incidence

and diffracted angles at different wavelengths as well as the position of the primary and secondary foci.

3.1.3 Spherical and toroidal mirrors

The object of this section is not to review the basics of geometrical optics; nevertheless we will introduce the equations used during the ray-tracing phase of this work to determine the final optical layout. In both optical systems mechanical constraints forced us to adapt the optical parameters to the desired configuration, i.e., define and calculate the required radii of curvature of the different mirrors. In addition we compare the reflectivity of the different mirrors according to their respective coatings (gold or iridium) with varying wavelength and angle of incidence.

In the prototype system used in the Rutherford Appleton Laboratory, a spherical concave mirror was used in a normal incidence configuration (angle of incidence of 7.5 degrees), the mirror equation can then be written as:

$$\frac{1}{p}+\frac{1}{q}=\frac{2}{R} \qquad [3.8]$$

where p is the mirror-object distance, q is the mirror-image distance and R is the radius of curvature of the mirror.

The use of a concave mirror to focus light onto the entrance slit of a spectrometer is common technique first to increase light collection in the instrument and to reduce the astigmatism of the system for certain wavelengths. However the combination of a toroidal mirror with a concave grating constitutes the best configuration to reduce astigmatism over a wide wavelength range (Tondello 1979).

Consequently, in the final set-up built in DCU a focusing toroidal mirror was introduced. The radii of the mirror as well as its position in the layout are given by the following equations:

Tangential plane $$\frac{1}{p}+\frac{1}{q}=\frac{2}{R\cos\alpha} \qquad [3.9]$$

Sagittal plane $$\frac{1}{p}+\frac{1}{q'}=\frac{2\cos\alpha}{\rho} \qquad [3.10]$$

where p is the object-mirror distance, q is the image-mirror distance in the horizontal or tangential plane, q' is the image-mirror distance in the vertical plane, R is the radius of curvature in the horizontal plane and ρ is the radius of curvature in the vertical or sagittal plane.

Optical aberrations are a major concern in the design of optical systems, and we will discuss this matter for both systems specifically. On the other hand it is also appropriate to discuss the dependence of the reflectivity of any optical surface on the incident radiation wavelength and the angle of incidence. In figure 3.4. we compare the reflectivity of a gold coated and an iridium coated mirror as a function of wavelength at near normal incidence and at grazing incidence.

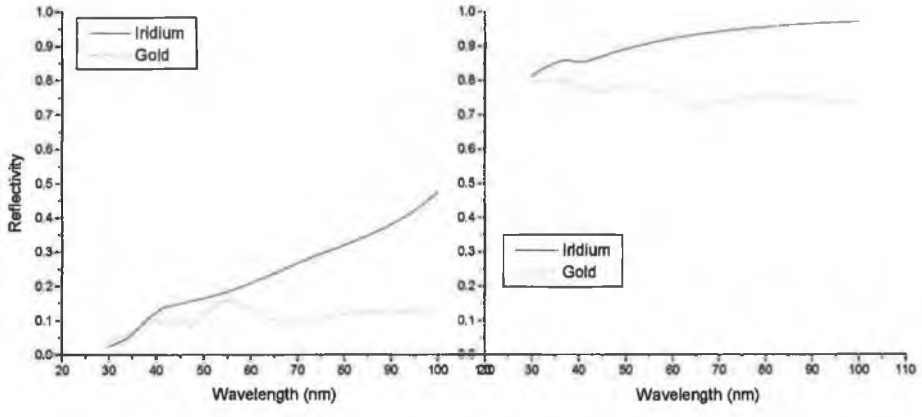

Figure 3.4. Reflectivity of an iridium coated optical surface and a gold coated surface at (A) near normal incidence (5°) and (B) grazing incidence (85°) (From the "multi-ray" code, University of Padova.)

Figure 3.4 shows a considerable increase in reflectivity when working at grazing incidence; the reflectivity reaches values larger than 70 % for both gold and iridium coating. The values of reflectivity are comparable for Gold and Iridium at both grazing and normal incidence at relatively short wavelengths, but diverge at longer wavelengths when the reflectivity of Iridium increases monotonically. It would appear logical to work at grazing incidence to benefit from the high reflectivity of the mirror, however optical aberrations increase with increasing incidence angle. Therefore, a trade off exists between

angle of incidence and optical aberrations/light collection efficiency. Working at grazing incidence provides a reflectivity gain, which must be offset against a flux loss due to reduced collection efficiency and increased aberration.

3.2 Prototype system used at RAL

This first experiment performed at the X-ray laboratory of the Central Laser Facility at RAL constituted essentially a proof of principle experiment to validate the photoabsorption imaging technique (Hirsch *et al.* 2000). The optical layout was arranged around existing equipment, mainly an iridium coated concave mirror and the 0.2 m monochromator. The ray tracing was used to minimise the loss of flux at the entrance slit of the monochromator, as well as to reduce optical aberrations. However, taking into account the mechanical constraints imposed by the existing vacuum equipment, the final configuration was far from optimum. Photographs of the system are shown in figure 3.5 and 3.6.

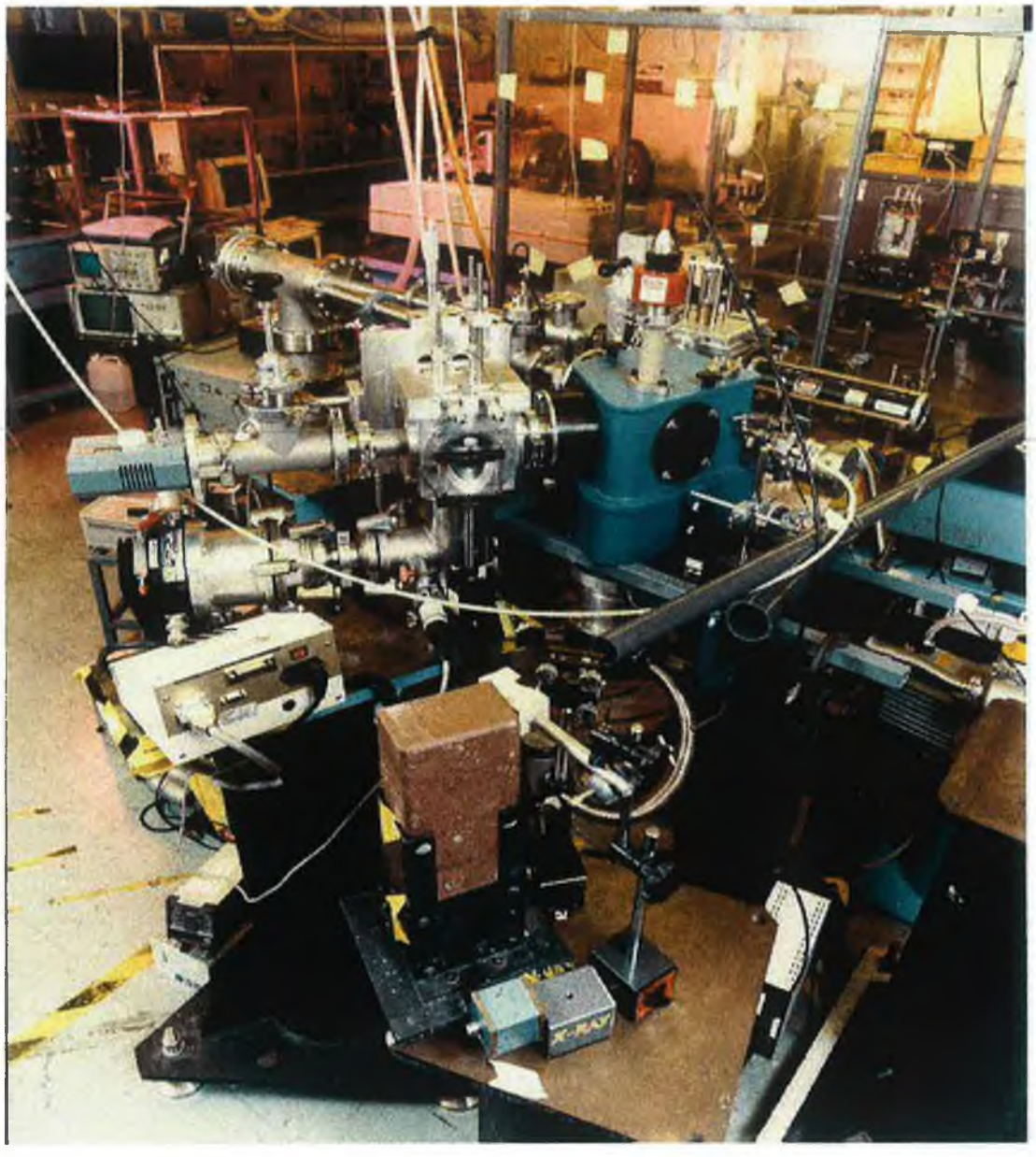

Figure 3.5. Experimental set-up used at RAL (side view –left)

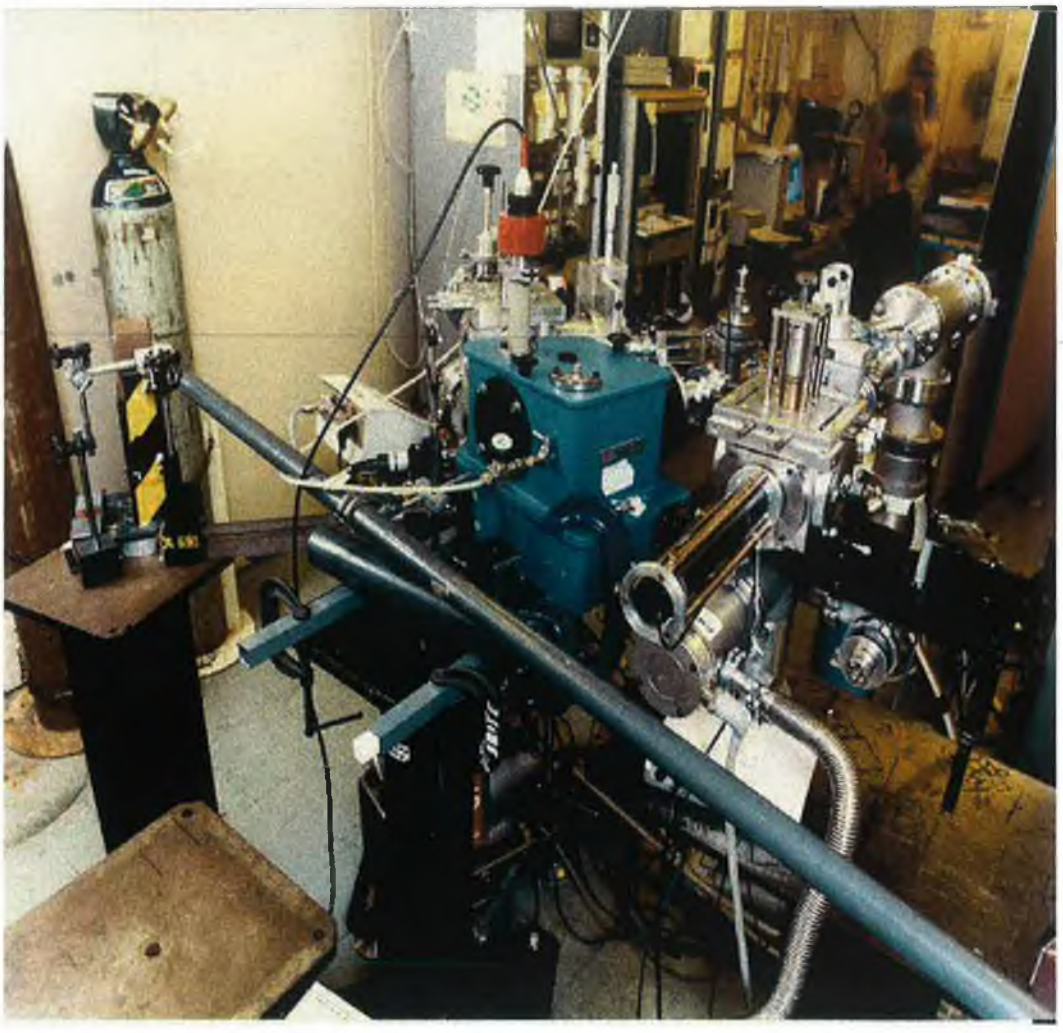

Figure 3.6. Experimental set-up used at RAL (side view –right)

In figure 3.7. we show a schematic diagram of the system.

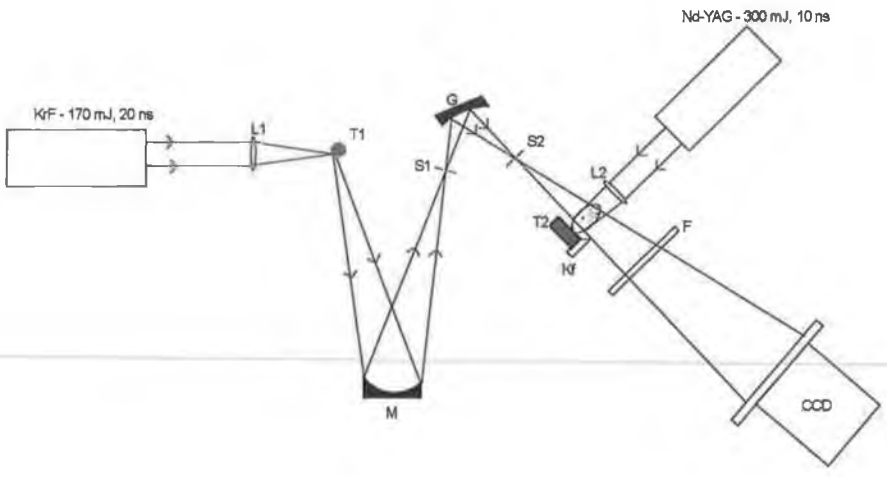

Figure 3.7. Experimental set-up used at RAL

3.2.1 Experiment overview

The experiment consisted of a tungsten plasma, generated by a KrF excimer laser, working at 248 nm, delivering 170 mJ in 20 ns and focused to a ~100 μm point by a 10 cm focal length f/5 fused silica lens. This tungsten plasma acted as a VUV continuum light source. It was located 1m from a f/10 iridium coated mirror of focal length 0.5 m with which it made an angle of incidence of 7.5°. The plasma source was imaged with unit magnification onto the entrance slit of a 0.2 m focal length vacuum f/4.5 monochromator (Acton™ VM-502). The VUV radiation emanating from the exit slit was directed through a calcium plasma produced by a Nd-YAG laser. The Nd-Yag laser (1064 nm, 300 mJ in 10 ns) was synchronised using a delay generator to the KrF laser pulse and focused to a horizontal line of length 8 mm and width ~ 0.25 mm by a 15 cm focal length cylindrical lens. A continuously variable delay in the range of nanoseconds to tens of microseconds with a jitter of < 5 nsec was inserted between the Nd-YAG and KrF laser pulses.

In order to shield the CCD detector from both scattered 248 nm laser light and direct calcium plasma emission, a 0.4 μm thick aluminium filter was placed in front of the camera. When combined with the near normal incidence iridium coated mirror, the composite filter restricted the monochromator transmission to light with a wavelength

range between 20 nm and 80 nm. In addition, a knife-edge was located close to the calcium target. It protruded some 200 μm outwards from the surface of the calcium target in order to occlude the brightest part of the calcium plasma from the direct view of the CCD. In this way we were able to further reduce the background signal on the CCD due to calcium plasma emission. It also provided a well-defined edge on the images and protected the aluminium filter, which was easily damaged by plasma debris in its absence. The VUV shadowgrams were recorded on a 2048 x 1024 pixel ANDOR™ back-thinned CCD camera with a pixel size of 13 μm x 13 μm, placed 50 cm from the exit slit of the monochromator and ~ 38 cm from the calcium plasma.

3.2.2 Vacuum arrangement

The system was composed of 4 main vacuum components: two target chambers housing both backlighting and sample plasmas, one mirror chamber and the 0.2 m monochromator. The target chambers are identical and consist of two 127 mm × 127 mm cubes with 70 mm diameter holes on each of the six sides (Kiernan 1994).
All six ports can be connected to:

- A window flange allowing the laser beam to penetrate into the target chamber and interact with the target
- Custom made flanges fitted with KF-40 connectors to couple the chamber to the rest of the vacuum system
- Custom made flanges allowing the connection to x, y, z vacuum compatible target holders, vacuum gauges or vacuum pumps

This symmetric configuration gives the system enough flexibility to be adapted to different experimental configurations. The whole system is evacuated using a combination of rotary and tubomolecular pumps reaching a typical pressure of the order of 10^{-5} mbar.

An important element of the vacuum system is a light tight but vacuum compatible aluminium filter holder. This filter holder consisted of a KF-50 T-piece fitted with an aluminium insert. A slot was machined into the insert allowing one to push the filter in and out of the beam path using a vacuum feedthrough. To avoid damaging the thin (0.4 μm) filter during the pumping phase, it was held in the "up" position, and when the pumping

was completed the filter was pushed down making the insert light tight. Several grooves machined into the insert enabled equal pressure to be maintained on both side of the filter. A schematic of the arrangement is shown in figure 3.8.

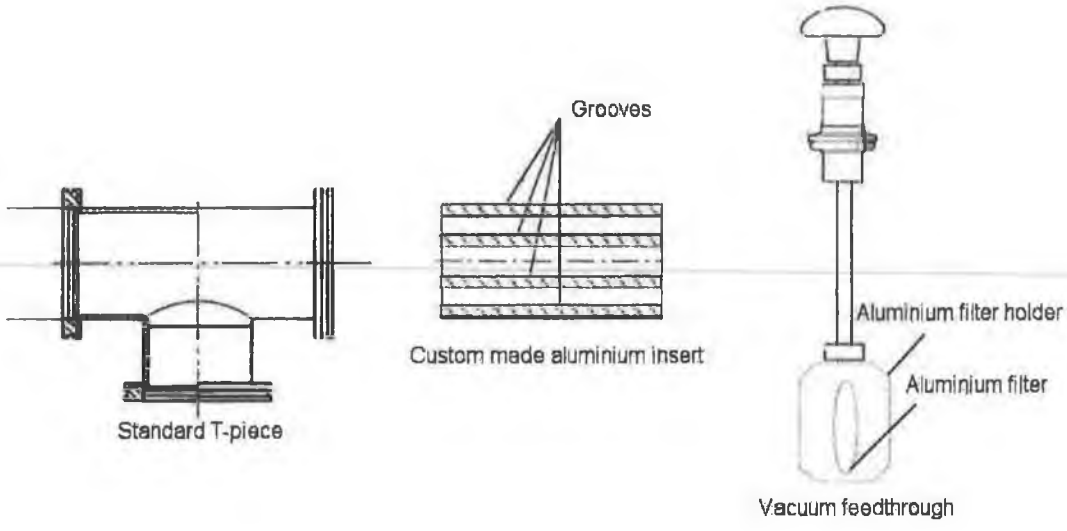

Figure 3.8. Aluminium filter holder arrangement

The calcium target was mounted on a translation stage allowing movement in the x, y, and z directions. This target holder was designed by C. Maloney (1998) and simplified considerably the alignment phase of the experiment since the target could be moved in and out of the VUV beam. The movement in the vertical z direction allowed us to move to a fresh target spot without changing its horizontal position.

3.2.3 Laser system and synchronisation

The experiment was carried out in the Lasers for Science Facility, part of the Central Laser Facility in the Rutherford Appleton Laboratory. Two laser systems were available for the experiment, a Nd-YAG laser and a KrF laser. The lasers specifications are summarised in table 3.1. and 3.2.

Krypton-fluoride Excimer laser (Lambda-Physik 205)	
Wavelength	248 nm
Energy	170 mJ
Pulse length	20-25 ns
Repetition rate	0.2 Hz
Trigger jitter	± 2 ns
Beam dimension	24 mm × 6-12 mm
Buffer gas	Neon

Table 3.1. Specifications of the KrF laser

Nd-YAG Laser	
Wavelength	1064 nm
Energy	300 mJ
Pulse length	10 ns
Repetition rate	10 Hz
Trigger jitter	± 1 ns
Beam dimension	12mm × 12 mm

Table 3.2. Specifications of the Nd-YAG laser

Laser synchronisation is essential for this experiment since much of the study concerns time resolved investigations. To synchronise the two laser systems and introduce a variable delay between the output pulses, two delay generators were used. The first delay generator produced a TTL pulse (5V, 10 Hz) and was used as the initial time reference T_0. One output was connected to the Nd-YAG flashlamps ensuring a repetition rate of 10 Hz. A second output was connected to a "divide by" electronic circuit to trigger the KrF laser at a desired repetition rate of 0.2 Hz. The same output pulse was then used to trigger the second delay generator at 0.2 Hz. One of the outputs was connected to the Nd-YAG Pockels cell allowing the laser to fire at the same repetition rate as the KrF laser. A delay of 180 ms was inserted between the flashlamp and the Pockels cell of the Nd-YAG laser. The delay

between the two lasers could then be adjusted by varying the setting on the second delay generator; delays from a few nanoseconds to microseconds could be inserted between the two laser pulses with a jitter of less than ± 5 ns. To prevent the laser from firing continuously both trigger pulses (on the YAG Pockels cell and the KrF Thyratron) were connected to the lasers via an "AND" gate controlled by the CCD camera. Taking an acquisition with the CCD camera would then open the gate and allow both lasers to fire for a defined time delay. The time delay was monitored using two photodiodes located at the back of the mirrors used to steer the laser beams and connected to a digital oscilloscope. A schematic diagram of the laser synchronisation is shown in figure 3.9.

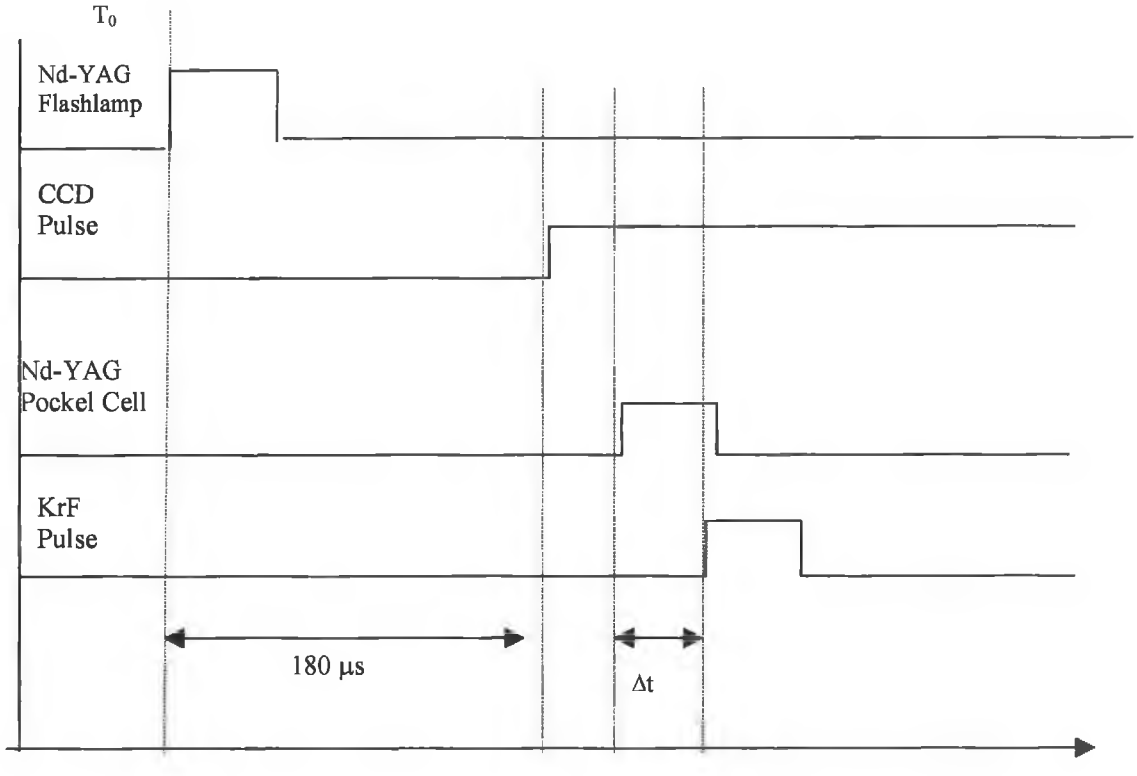

Figure 3.9. Timing diagram used at RAL to fire both lasers at a defined time delay Δt

3.2.4 Ray tracing

The source used in this simulation is a laser produced plasma, which we approximate as a point source for the ray tracing. The light emitted is intercepted by a spherical iridium coated mirror of 0.5 m focal length and an aperture of f/10 which constitutes the entrance arm of the optical system. The angle of incidence of the central ray on the mirror is 7.5°. The laser plasma continuum source is located at a 1m from the mirror and hence the system operates with an aperture of f/20 and the divergence of the plasma light source computed in the ray tracing code was set accordingly to 50 mrad.

The spherical mirror focuses the light emanating from the plasma source onto the entrance slit of a 0.2 m, f/4.5 vacuum monochromator, also located at 1m from the mirror. On the exit arm of the system, the sample plasma is located at 115 mm and the CCD camera at 0.5 m from the exit slit of the monochromator. A schematic of the optical layout is shown in figure 3.10.

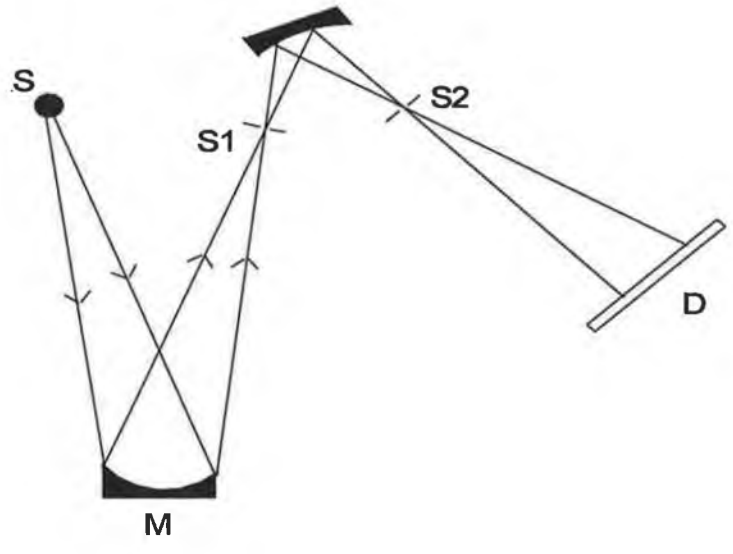

Figure 3.10. Schematic of the optical set-up with S: plasma source, M: concave mirror, S1: entrance slit, S2: exit slit and D: CCD camera

3.2.4.1 Monochromator simulation

The monochromator used in the RAL experiment is a VM-502 Acton Research monochromator with specifications as shown in table 3.3.

VM-502 Specifications (1200 lines/mm Grating)	
Operating range	30 nm to 550 nm
Focal length	200 mm
Dispersion	4 nm/mm
Optical system	Concave Grating
Angle between Entrance and Exit ports	64 Degrees
Aperture ratio	F/4.5

Table 3.3. Acton research monochromator specifications

The monochromator parameters, i.e., the angle of incidence on the grating, the diffracted angle and the position of the primary and secondary foci have to be calculated and used as inputs in the ray tracing code. These parameters can be calculated for every wavelength using the following classical equations derived in section 3.1:

$$\alpha - \beta = 64^0 \qquad [3.11]$$

$$\sin(\alpha) + \sin(\beta) = \frac{m\lambda}{d} \qquad [3.7]$$

$$\frac{\cos^2(\alpha)}{p} + \frac{\cos^2(\beta)}{q} = \frac{\cos(\alpha) + \cos(\beta)}{R} \qquad [3.4]$$

First of all, we calculate the angle of incidence of the light entering the monochromator. This value is dependent on the light wavelength as indicated in equation [3.7]. Knowing α for the different wavelengths of interest it is then trivial to calculate the diffracted angle β using equation [3.11].

Using [3.11] and [3.7] we obtain a relation between the angle of incidence and the radiation wavelength:

$$\alpha = 32^0 + \arcsin\left(\frac{m\lambda}{2d\cos(32^0)}\right) \qquad [3.12]$$

The system was ray-traced for three different wavelengths 30 nm, 50 nm, and 100 nm corresponding to the wavelength range of interest for the experiment. The results are summarised in table 3.4.

Wavelength	*Incidence angle α*	*Diffracted angle β*
30 nm	33.216 °	30.784 °
50 nm	34.027 °	29.973 °
100 nm	36.057 °	27.943 °

Table 3.4. Calculated incident and diffracted angles for three wavelength settings

Knowing α and β the position of the primary focus (spectral focus) can be determined using equation [3.4]. Using the Rowland circle condition we choose p = q = r and equation [3.4] becomes:

$$\frac{\cos^2(\alpha)+\cos^2(\beta)}{r} = \frac{\cos(\alpha)+\cos(\beta)}{R} \qquad [3.13]$$

and the position of the primary focus is given by:

$$r = R\left(\frac{\cos^2(\alpha)+\cos^2(\beta)}{\cos(\alpha)+\cos(\beta)}\right) \qquad [3.14]$$

In a similar fashion, we can calculate the position of the secondary focus r' (vertical focus) using equation [3.5].

$$\frac{1}{r'} = \frac{\cos(\alpha) + \cos(\beta)}{R} - \frac{1}{r} \qquad [3.5]$$

The values of r and r' calculated at 30 nm, 50 nm, 100 nm, are shown in table 3.5.

Wavelength	*Horizontal focus r*	*Vertical focus r'*
30 nm	169.60 mm	387.24 mm
50 nm	169.58 mm	387.86 mm
100 nm	169.52 mm	390.60 mm

Table 3.5. Position of the horizontal and vertical focus of the M-502 Acton Research monochromator for different wavelengths (the positions are measured from the centre of the grating)

3.2.4.2 Aberrations at the monochromator entrance slit

The ray tracing code enables one to view the footprint of the beam at any stage during the system simulation. Assuming a point source, and a divergence of 50 mrad, we monitor the optical aberrations at the entrance slit of the monochromator for different angles of incidence on the mirror. The results are shown in figure 3.11. for an angle of incidence on the mirror of 5, 7.5, 10°.

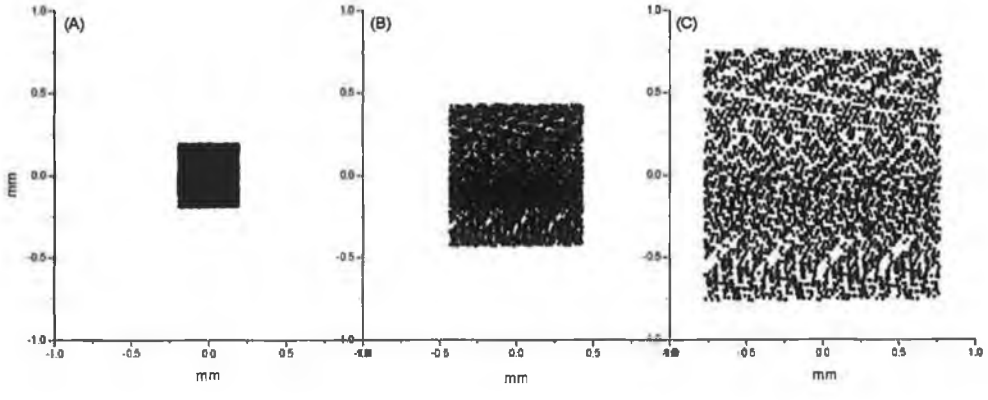

Figure 3.11. Image of a point like source at the entrance slit plane for an angle of incidence of (A) 5°, (B) 7.5° and (C) 10°

As expected the aberrations increase with the increasing angle of incidence, the source size is 0.4 mm x 0.4 mm at 5 degrees incidence angle, 0.86 mm x 0.86 mm at 7.5° and 1.62 mm x 1.62 mm at 10°. We notice that aberrations increase very rapidly with the angle of incidence, and even though the reflectivity of iridium is much higher for grazing incidence angle, aberrations are so important that the output flux is close to zero. Due to mechanical constraints, set by the only vacuum mirror chamber available for the experimental test, and a trade off between high reflectivity and low aberrations, we chose an angle of incidence of 7.5°, which corresponded to an image of the source on the entrance slit of the monochromator of dimensions 0.86 mm x 0.86 mm. The system operates with an entrance slit of 250 μm, thus the flux loss is ~ 70 % after the entrance slit of the monochromator. In figure 3.12 we show the reflectivity of an iridium coated mirror for different angles of incidence for a wavelength of 50 nm as well as the reflectivity at an angle of incidence of 7.5 degrees as a function of the radiation wavelength.

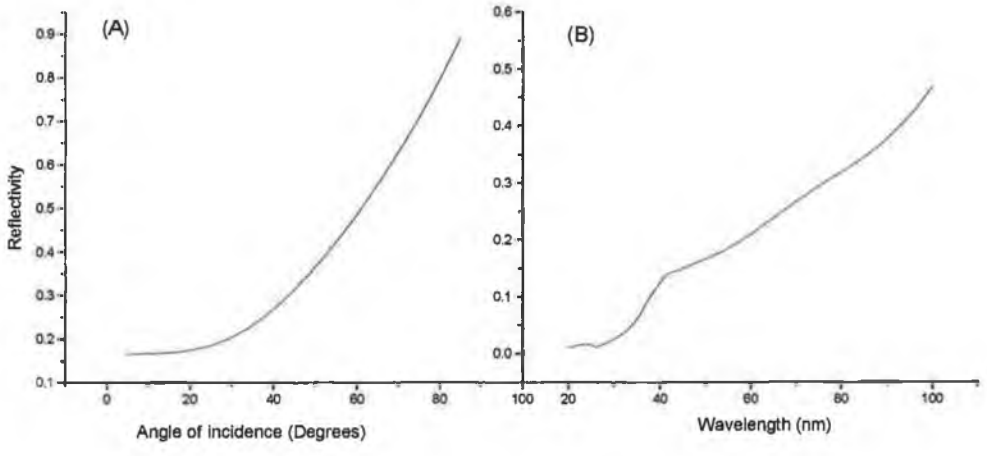

Figure 3.12. Reflectivity of an iridium coated mirror (A) as a function of the angle of incidence for a wavelength of 50 nm and (B) as a function of wavelength for an angle of incidence of 7.5°

As seen in figure 3.12, the reflectivity near normal incidence is poor where it varies from 0.05 to 0.3 between 30 and 80 nm, the wavelength range of interest, reducing the light flux considerably. The need for a better focusing optical element working near grazing incidence to increase the reflectivity and with better focusing properties is clearly indispensable in the optical set-up. This modification was implemented in the final set-up built in the DCU laboratory discussed in section 3.4.

3.2.5 RAL system performance

3.2.5.1 Spectral resolution

The spectral resolution was calculated using the ray tracing code, but due to the limited time allocated to the experiment, it wasn't measured experimentally. The spectral resolution can be calculated at every wavelength but since the system was ray-traced at VUV wavelength of 30 nm, 50 nm, 70 nm and 100 nm, we only performed the calculations for these wavelengths. The procedure is quite straightforward. The output flux at the exit slit of the spectrometer for the set wavelength is taken as a reference. The wavelength is then increased in small $\delta\lambda$ steps until 50% of the initial flux is lost, the corresponding wavelength interval is written as $\Delta\lambda_1$. The same wavelength scan is repeated when decreasing the wavelength and the second interval is written as $\Delta\lambda_2$.
The resolving power is then given by:

$$R = \frac{\lambda}{\Delta\lambda_1 + \Delta\lambda_2} \qquad [3.15]$$

The results are shown in figure 3.13.

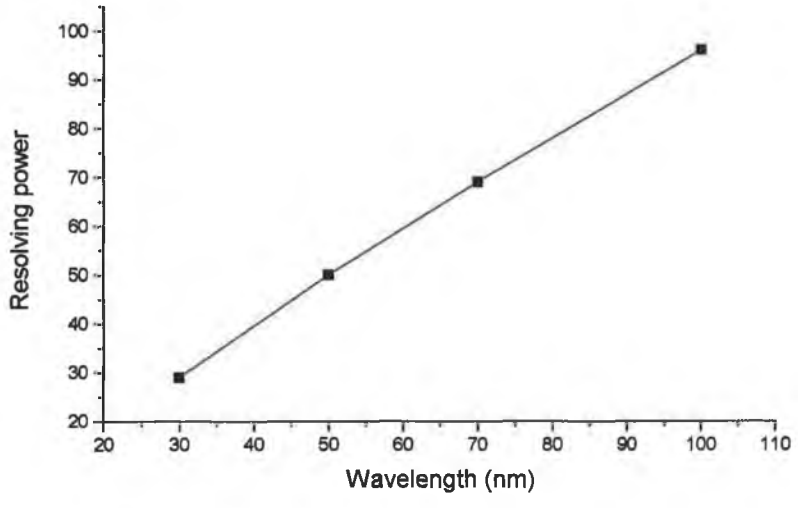

Figure 3.13. System resolving power as a function of wavelength for an entrance and exit slit width of 250 μm

The poor values obtained for the spectral resolution can be explained as follows. The ray tracing study showed that the spectral resolution was mainly determined by the width of the entrance slit of the monochromator. Here to minimise the flux loss, the entrance slit width was set at 250 μm and hence the very low resolution; added to this, the fact that the grating was under-filled due to non-matching f-number of the different optical components of the system may also have contributed to slightly lower the spectral resolution.

3.2.5.2 Magnification and spatial resolution

To measure the magnification of the system in the horizontal plane we used a moveable knife-edge. Starting at the cut-off position (i.e., blocking all VUV radiation from the backlighter) the knife-edge was retracted from the VUV beam in steps of 200 μm and the corresponding change in image size recorded. As expected, we observed a linear relation between the dimension recorded on the camera plane and the real dimension at the plasma position. A linear fit on the data points gives a value of 3.4 ± 0.1 for the slope of the graph corresponding to the horizontal magnification. The magnification in the vertical plane was also measured using a moveable knife-edge and a value of 1.0 ± 0.1 was obtained. The horizontal magnification is shown in figure 3.14.

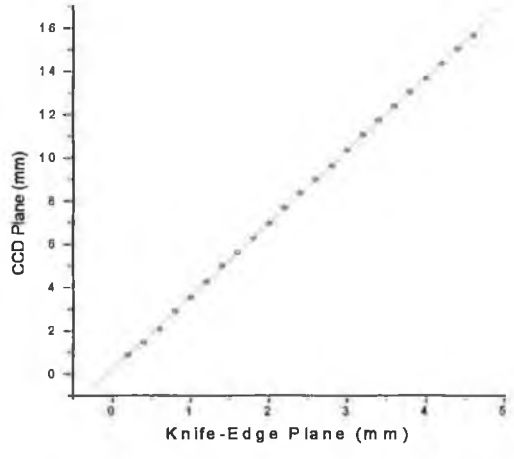

Figure 3.14. System magnification in the hortizontal plane

We used the same knife-edge data to estimate the horizontal and vertical resolution of the system. From an image where the knife-edge cuts the VUV beam, we isolate one line of pixels on the detector and measure the intensity fall off. This is shown in figure 3.15.

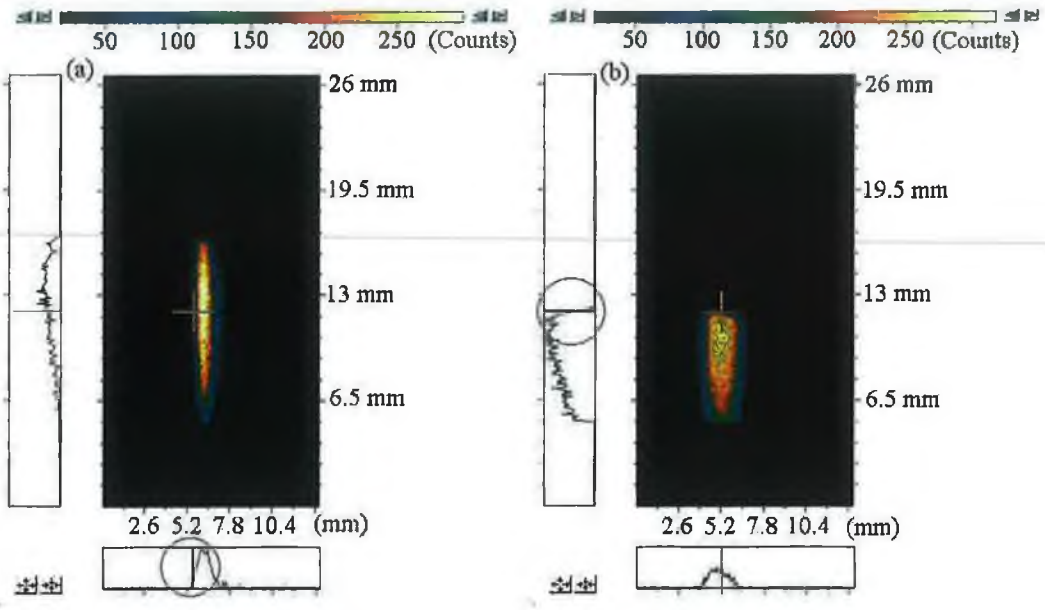

Figure 3.15. Intersection of the knife-edge and the monochromatic VUV beam in (a) the vertical plane and (b) the horizontal plane

The curve obtained is defined as the edge function and corresponds to the integral of the of the line spread function following the relation (Williams and Becklund 1989)

$$W_e(x) = \int_{-\infty}^{x} W_l(u)du \qquad [3.16]$$

where W_e is the edge trace function and W_l is the line spread function. To obtain the line spread function we take the derivative of the edge trace at every point. The resulting function is best approximated by a Gaussian function and its width (FWHM) determines the spatial resolution. Figure 3.16 shows the edge trace function when inserting the knife edge into the VUV beam and the resulting line spread function in the horizontal plane.

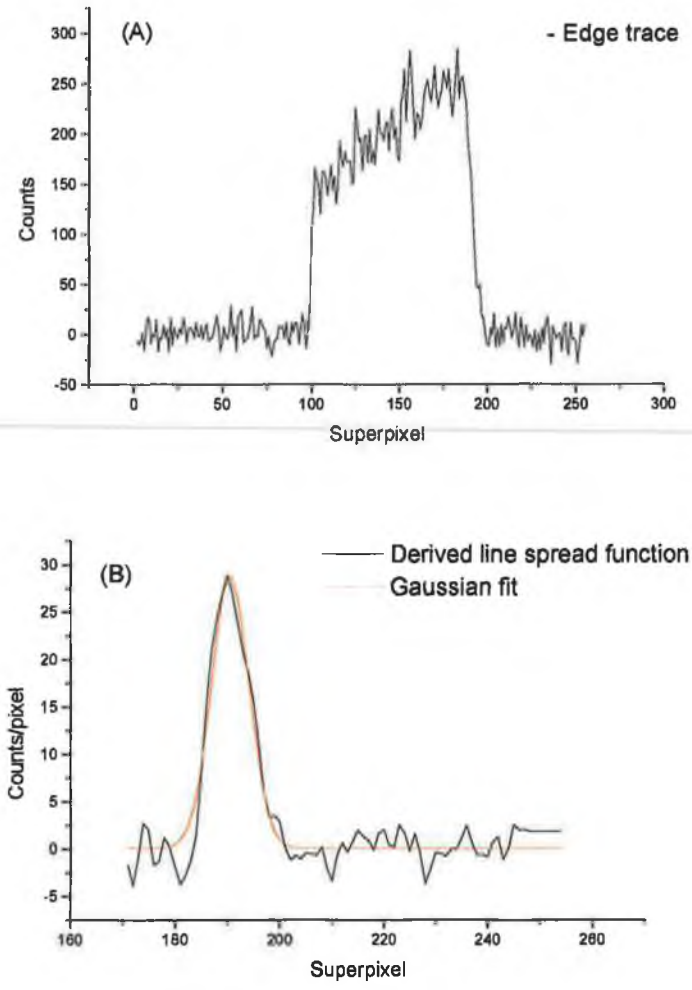

Figure 3.16. Determination of the horizontal spatial resolution, with (A) the edge trace and (B) the derived line spread function

In the horizontal plane (meridional plane), the spatial resolution is mainly determined by the size of the exit slit, here we measure the width of the Gaussian fit to be 7.15 superpixels, i.e., 13 μm pixels binned 4 x 4 for this measurement. Hence, we extract a spatial resolution of 371 μm in the horizontal plane.

Figure 3.17, shows the edge trace function when inserting the knife edge into the VUV beam and the resulting line spread function in the vertical plane.

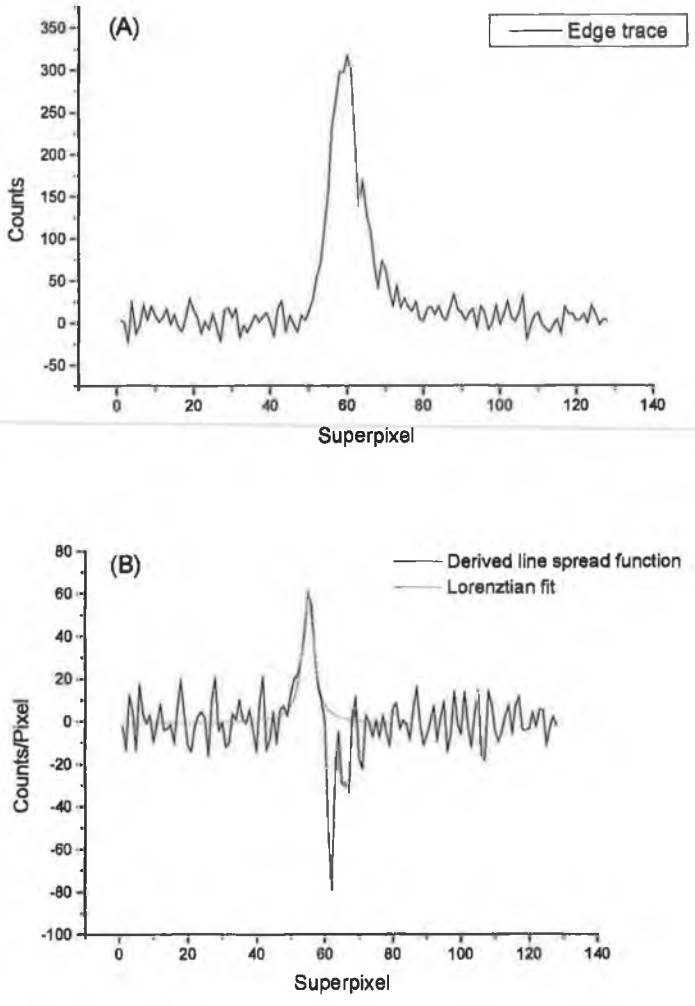

Figure 3.17. Determination of the vertical spatial resolution, with (A) the edge trace and (B) the derived line spread function

In the vertical plane there is no aperture on the beam so that the resolution here depends on the vertical size of the VUV source. Using the same procedure, we measure a width (FWHM) of 4 superpixels for the Lorentzian fit. In this experiment, the pixels were binned 8 x 8, and hence we deduce a vertical spatial resolution of 420 μm.

3.2.5.3 Beam footprint

The position of the sample target with respect to the monochromatic VUV beam is shown in figure 3.18.

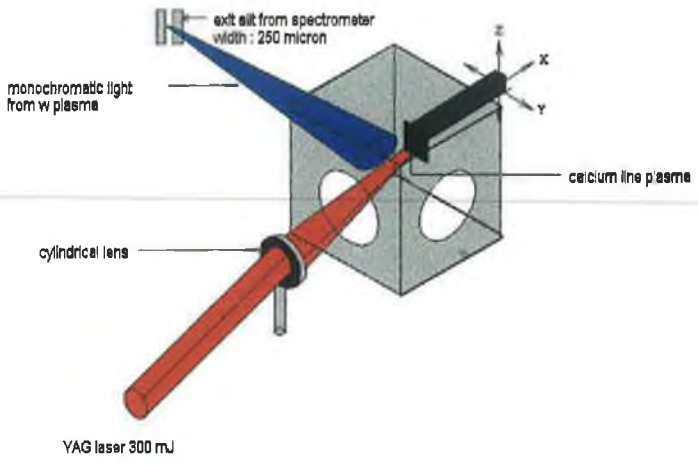

Figure 3.18. Position of the sample target with respect to the VUV beam

The results of the ray tracing study were compared to the footprint of the probe beam measured by locating the CCD camera at different positions from the exit slit of the monochromator. From a previous experiment, we assumed that the size of the VUV continuum source is an ellipse of major axis 140 μm and minor axis 100 μm. These dimensions were used in the ray tracing, and the theoretical and experimental results at 50 nm are compared in figure 3.19.

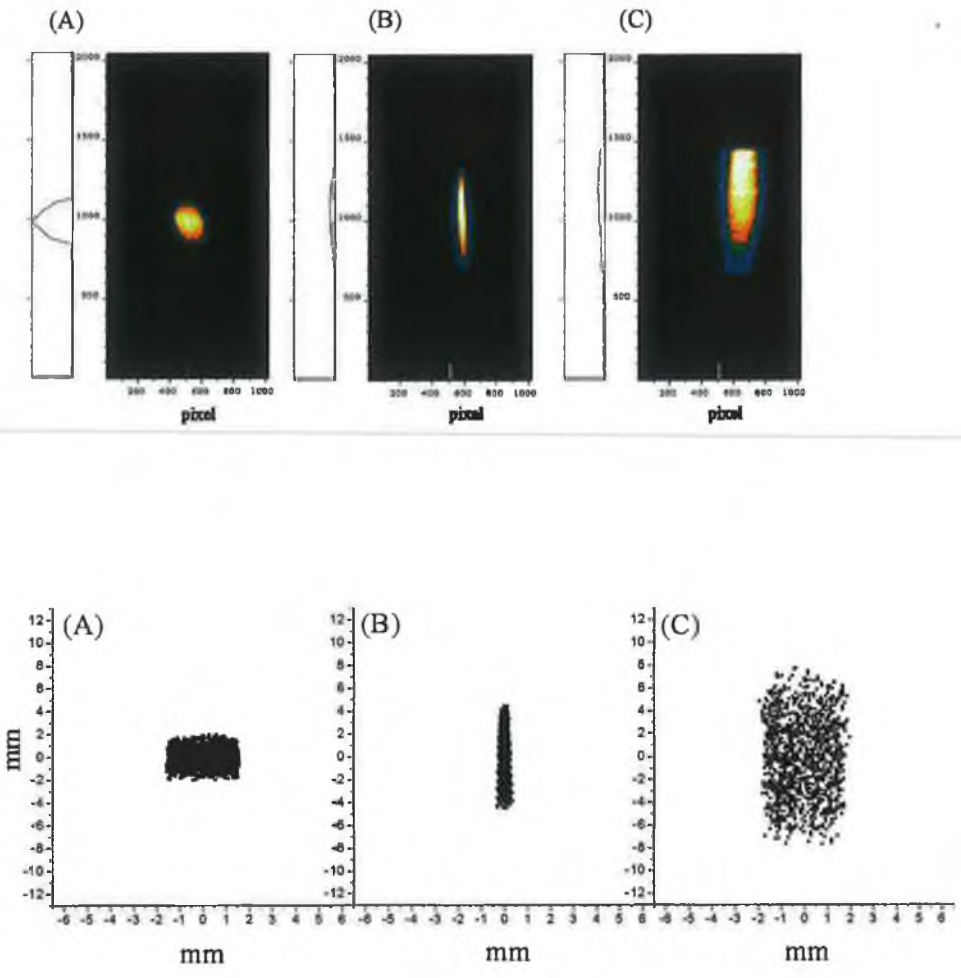

Figure 3.19. Comparison between the VUV beam footprint measured experimentally and the footprint computed using the ray tracing code at (A) 115 mm, (B) 280 mm and (C) 500 mm from the exit slit of the monochromator

The ray tracing calculations predict a probe beam of size of 4 mm x 3.2 mm at 115 mm from the exit slit of the monochromator, 9 mm x 0.7 mm at 280 mm and 15 mm x 3.9 mm at 500 mm. These values are in good agreement with the results obtained experimentally which show a footprint of 4.2 mm x 3.0 mm at 115 mm, 8.7 mm x 0.7 mm at 280 mm and 11 mm x 4.0 mm at 500 mm. The error on these measurements depends on the spatial resolution of the system, i.e., 360 μm in the horizontal plane and 420 μm in the vertical plane. The difference in the horizontal size at 500 mm, 11 mm measured instead of 15 mm expected according to the ray tracing, is a consequence of the position of the

aluminium filter holder which cuts part of the beam. From these measurements we deduce that the VUV beam diverges in the horizontal plane with an angle of ~ 0.03 rad. In the vertical plane it is first brought to a horizontal focus at a distance extrapolated to be 310 mm from the exit slit of the monochromator, and then diverges with an angle of ~ 0.014 rad.

3.3 Collimated VUV beam system implemented in DCU

The design of the first optical set-up used at RAL provided a useful experience for the final design of the photoabsorption imaging system. It demonstrated the existence of a tight trade off between the different optical parameters, i.e., angle of incidence, numerical aperture, width of the spectrometer entrance/exit slit, and the characteristics of the output beam exiting the system (flux, divergence, aberrations, beam size). The main concerns we had were the output flux and the limitations of chromatic or optical aberrations. We learned that these two quantities were closely linked. Reducing the numerical aperture of the system will reduce the aberrations but reduce the output flux. At the same time, increasing the incidence angle going to grazing incidence, will increase the reflectivity and thus the output flux, however this will increase aberrations. The aim of this new system was to reduce the flux loss and aberrations at the entrance slit of the monochromator and to deliver a quasi monochromatic and parallel beam of a defined cross section. Here again, we had to deal with a trade off between the beam cross section and the output flux, since increasing the beam cross section will decrease the collected flux per single pixel on the detector. We present here three different optical configurations envisaged as a possible final design during the ray tracing phase of this project, and will justify the selection criteria leading to the final design. This work was performed in collaboration with P. Nicolosi and L. Poletto of the University of Padova.

The 1m normal incidence monochromator has an aperture of f/10.4 in the tangential plane and f/17.5 in the sagittal plane. The angle of incidence on both mirrors was given the nearest possible value to grazing incidence as the reflectivity was very poor near normal incidence. However with such an angle of acceptance the aberrations were high and the size of the optics needed too large for the geometry of the system. We calculated that 400 mm was the minimum distance for the surface of the mirrors not to be contaminated by plasma

debris and with an aperture of f/10.4, 40 mm diameter mirrors would have been needed at normal incidence. As a result the numerical aperture of all three systems had to be reduced.

- **System 1**

This system (figure 3.20) operates with an aperture of f/100 × f/100, and delivers a parallel beam of cross section 4 mm x 4 mm. The entrance arm is composed of a toroidal mirror in Rowland configuration, located at 400 mm from the plasma source and 400 mm from the entrance slit of the monochromator. The mirror tangential radius is 4590 mm and the sagittal radius is 35 mm working at 85° incidence, and images stigmatically the plasma source on the entrance slit of the monochromator. The monochromator houses a spherical grating at 15° subtended angle. The exit arm is composed of a second toroidal mirror located at 400 mm from the exit slit. The mirror tangential radius is 9180 mm and the sagittal radius is 63.5 mm working at 85° incidence angle. The reflected beam is a parallel beam of cross section 4 mm × 4 mm which gives us flexibility for the location of the sample plasma and the CCD camera.

The entrance and exit slits of the monochromator were set at 50 μm which gives a resolving power of 1000 at 50 nm and a predicted spatial resolution (point spread) of 70 μm (in the horizontal plane) and 150 μm (in the vertical plane) from the ray tracing simulations.

A schematic diagram of the system is shown on fig 3.20.

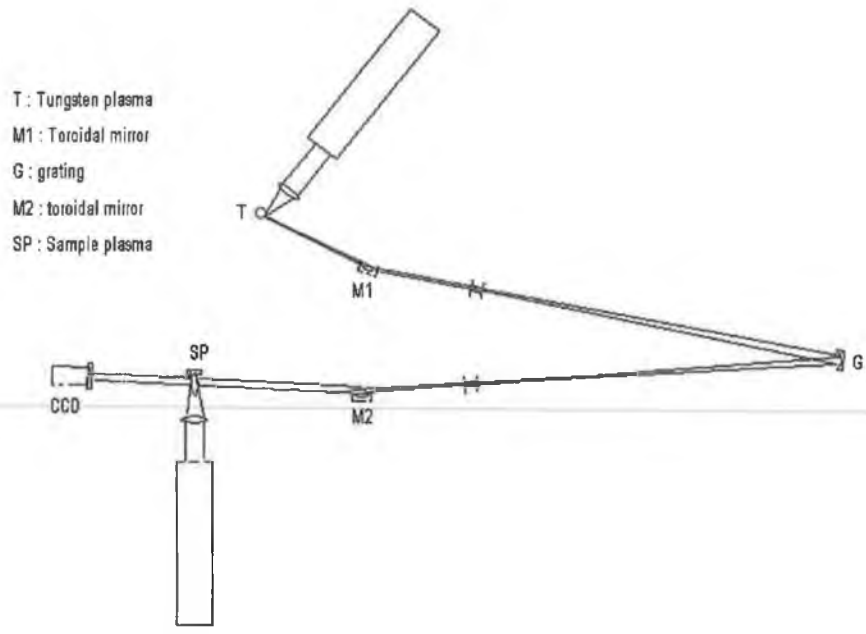

Figure 3.20. Schematic of the optical configuration, where T is the tungsten backlinghting plasma, G the spherical grating, SP the sample plasma, M1, M2 the entrance and exit mirrors, and the CCD detector

The flux collected at the CCD camera position was evaluated using the following formula:

$$I(\lambda) = I_0(\lambda)\ \Omega\ R_1(\lambda)\ T_1\ E_G\ T_2\ R_2(\lambda) \qquad [3.17]$$

where I_0 is the intensity per unit solid angle emitted by the plasma source at a given wavelength, Ω is the acceptance solid angle of the spectroscopic system, R_1 and R_2 the reflectivity of the mirrors, T_1 and T_2 the transmittance of the entrance and exit slits of the monochromator and E_G the grating efficiency. For a wavelength of 50 nm we have:

$T1 = T2 = 1$ $\qquad$ $\Omega = 0.0001$ sr

$R1 = R2 = 0.78$ $\qquad$ Bandwidth: 0.05 nm

$E_G = 0.08$

With an estimated (Fischer *et al.* 1984) photon flux $I_0 \sim 10^{13}$ ph/nm/sr/pulse in the VUV, we obtain a VUV flux of 27 photons/pixel. We can relate this value to the number of counts

per pixel on the CCD camera. Taking into consideration the transmission of the aluminium filter located in front of the detector (see figure 3.21), the incident flux on the camera is:

I(50 nm) = 18 ph/13 μm pixel for a 0.2 μm filter,

and I(50 nm) = 12 ph/13 μm pixel for a 0.4 μm filter.

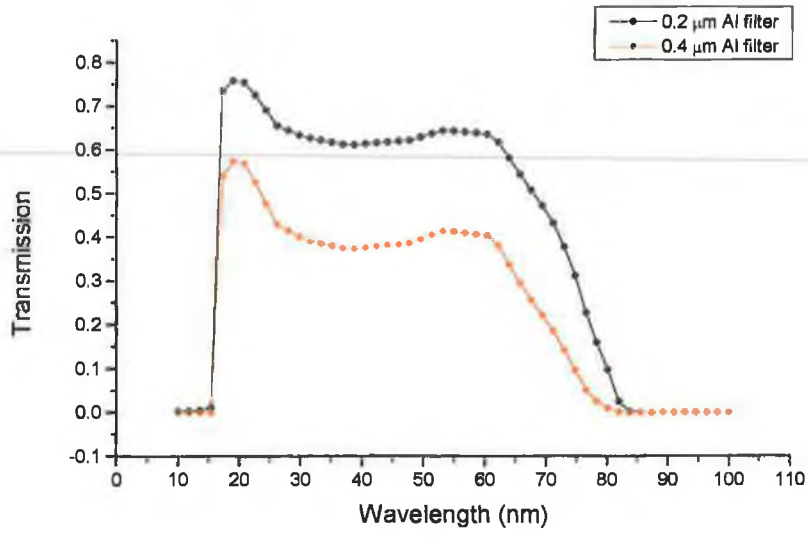

Figure 3.21. Transmission of a 0.2 μm and 0.4 μm filters as a function wavelength (from Center for X-Ray Optics database: http://www-cxro.lbl.gov/optical_constants/filter2.html)

The number of counts N_c per detected photon is given by ANDOR (private communication 2002):

$$N_c = Q_E \frac{E}{3.65g} \qquad [3.18]$$

where Q_E is the quantum efficiency of the detector, E is the incident photon energy in eV, and g the gain of the camera. The quantum efficiency QE, and the gain g, are given by the CCD manufacturer (ANDOR). For our specific detector in our mode of operation the gain is 1.4 and quantum efficiency is 22% at 50 nm.

We can now determine the number of counts per pixel $N = \frac{I(50nm)}{N_c}$ on the CCD camera:

N = 16 counts/pixel for a 0.2 μm Al filter.

N = 11 counts/pixel for a 0.4 μm Al filter.

- **System 2**

This system (similar in lay out to system 1, figure 3.20) operates with an aperture of f/50 × f/50 and delivers a parallel beam of cross section 4 mm × 4 mm. The entrance arm is similar to the first system but as the aberrations were too severe at 85° incidence angle, the angle was reduced to 80° where there wasn't any aberration on the entrance slit and no flux loss. The mirror's tangential and sagittal radii are 2303 mm and 69 mm, respectively, and it images the plasma source on the entrance slit of the monochromator.

The exit arm is composed of a second toroidal mirror located at 200 mm from the exit slit. The mirror tangential radius is 2303 mm and the sagittal radius is 66.5 mm working at 80°. The reflected beam is a parallel beam of cross section 4 mm × 4 mm which gives us here again flexibility for the location of the sample plasma and the CCD camera.

The entrance and exit slit of the monochromator were set at 50 μm which, according to the ray tracing code, gives a resolving power of 1000 at 50 nm and a spatial resolution of 130 μm (in the horizontal plane) and 300 μm (in the sagittal plane).
The output flux can be evaluated using equation [3.17].

T1 = T2 = 1	$E_G = 0.08$
R1 = R2 = 0.62	$\Omega = 0.0004$ sr
Bandwidth: 0.05 nm	$I_0 = 10^{13}$ ph/nm/sr/pulse

The estimated flux is then I(50nm) = 65 photons/pixel
Similarly the number of counts per pixel on the camera is calculated to be:
N = 41 counts/pixel for a 0.2 μm Al filter.
N = 27 counts/pixel for a 0.4 μm Al filter.

- **System 3 (VUV projection imaging)**

This system operates with an aperture of f/25 × f/18. For these angles of acceptance the angle of incidence on the entrance mirror was reduced to 60°. Here again, the entrance arm is composed of a toroidal mirror located at 400 mm from the plasma source and 400 mm from the entrance slit of the monochromator. The mirror tangential radius is 800 mm and the sagittal radius is 200 mm and images stigmatically the plasma source on the entrance slit of the monochromator.

In this system the configuration of the exit mirror changes from the previous two systems; here the image of the sample laser produced plasma is focused by the mirror onto the detector. The exit arm toroidal mirror operates in the Rowland configuration having the plasma itself as a source. The toroidal mirror is located at 500 mm from the exit slit and 400 mm from the sample plasma. The sample plasma is located at 100 mm from the exit slit and the probe beam has cross section 4 mm × 4 mm at the sample plasma position. The mirror tangential radius is 4590 mm and the sagittal radius is 35 mm working at 85°. The mirror radii were determined with the entrance arm being the mirror-plasma distance and not the mirror-slit distance. This way, we obtain an image of the sample plasma with a one to one magnification on the CCD camera located at 400 mm from the mirror. In this set up, the best spatial resolution is 25 μm x 25 μm in the vertical and horizontal directions. A schematic of the optical lay out is shown in figure 3.22.

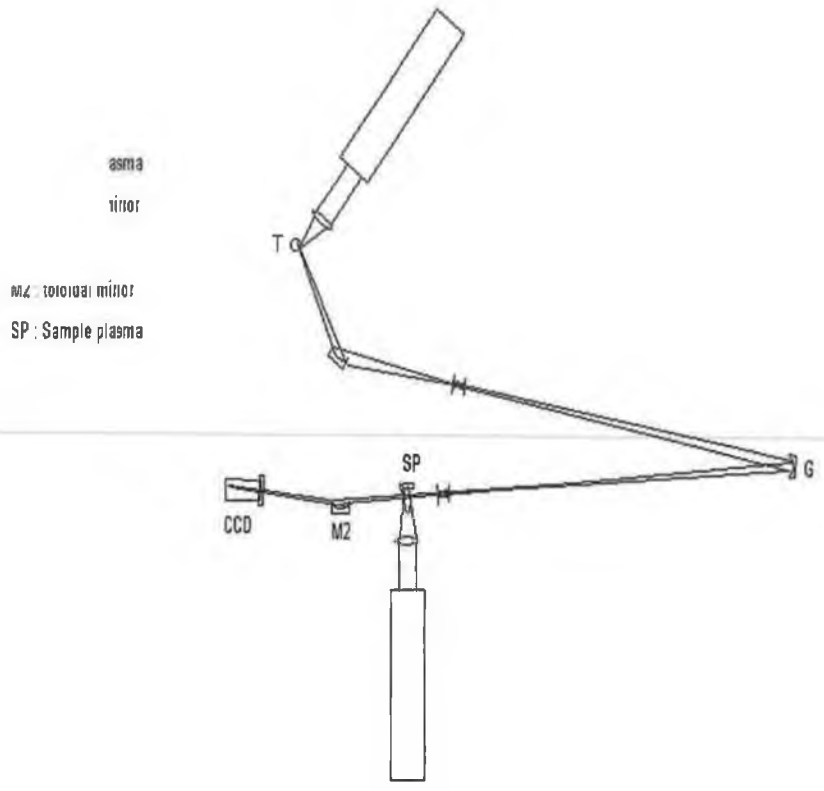

Figure 3.22. Schematic of the optical system configuration, where T is the tungsten backlighting plasma, G the spherical grating, SP the sample plasma, M1, M2 the entrance and exit mirror, and the CCD detector

We can determine the estimated flux for this configuration using equation [3.17] for a wavelength of 50 nm:

$T1 = T2 = 1$	$R1 = 0.32$
$R2 = 0.62$	$E_G = 0.08$
$\Omega = 0.0022$ sr	Spectral range: 0.05 nm

The estimated flux is I(50nm) = 185 photons/13 μm pixel. The number of counts per pixel is then:

N = 117 counts/pixel for a 0.2 μm Al filter.

N = 77 counts/pixel for a 0.4 μm Al filter.

- **Justification for the final optical lay out**

When referring to flux considerations, the third system appears to be the best option, delivering the highest flux and the best spatial resolution. The main problem, however, is that the sample plasma is directly imaged onto the detector constituting a very bright signal compared to the intensity of the probe beam. From the first experiment we learned that the sample plasma emission had to be reduced to a minimum to obtain reliable results. In this configuration the detector would be saturated, and the relative intensity of the probe beam versus the sample plasma emission is just too poor to obtain reasonable results. However, the sample plasma emission in the VUV tends to die out after ~250 ns. Hence, with a gated VUV-CCD, locked to the continuum pulse, one could employ this system to obtain photoabsorption images for long time delays after sample plasma breakdown.

The first two systems are very similar since they both deliver a parallel beam of cross section 4 mm x 4 mm. The advantages of working with a parallel beam are numerous. The geometry of the system is simplified since the distance between the sample plasma and the CCD camera can be adjusted to comply with mechanical constraints. Since the beam is parallel the divergence of the beam is very low and hence the transverse coherence is good (almost a plane wavefront). Finally, as the plasma light source is broadband, the longitudinal coherence is low reducing the effect of interference patterns.

However, there are three main differences: the output flux, the spatial resolution and the exit arm length. The second system operates with a larger angle of acceptance so that the output flux is more than double the flux exiting the first system, however the spatial resolution decreases by a factor of 2. No improvement to the spatial resolution can be made in the second system but the flux can be increased in the first configuration without losing resolution. The CCD camera is composed of 13 μm pixels, however keeping the spatial resolution of 70 μm, we can bin the pixels 3 x 3. A gain in flux of a factor of 9 can be achieved, without reducing the resolution and almost still satifying the Nyquist criteria of 2 pixels per cycle. Moreover, the distance between the mirror and the exit slit of the monochromator has to be 200 mm in the second set-up and, due to mechanical constraints, it would require a different design for the target chamber and additional costs.

As a consequence, the first system was chosen. By binning the pixels on the detector the flux can be increased without interfering with the spatial resolution. Moreover, the symmetric design of both target and mirror chambers constituted a considerable cut in the construction costs. In the next section we will describe in detail the first optical system : ray tracing, vacuum arrangement, laser system, optical properties including a comparison between calculated and measured optical performances.

3.3.1 Experimental set-up.

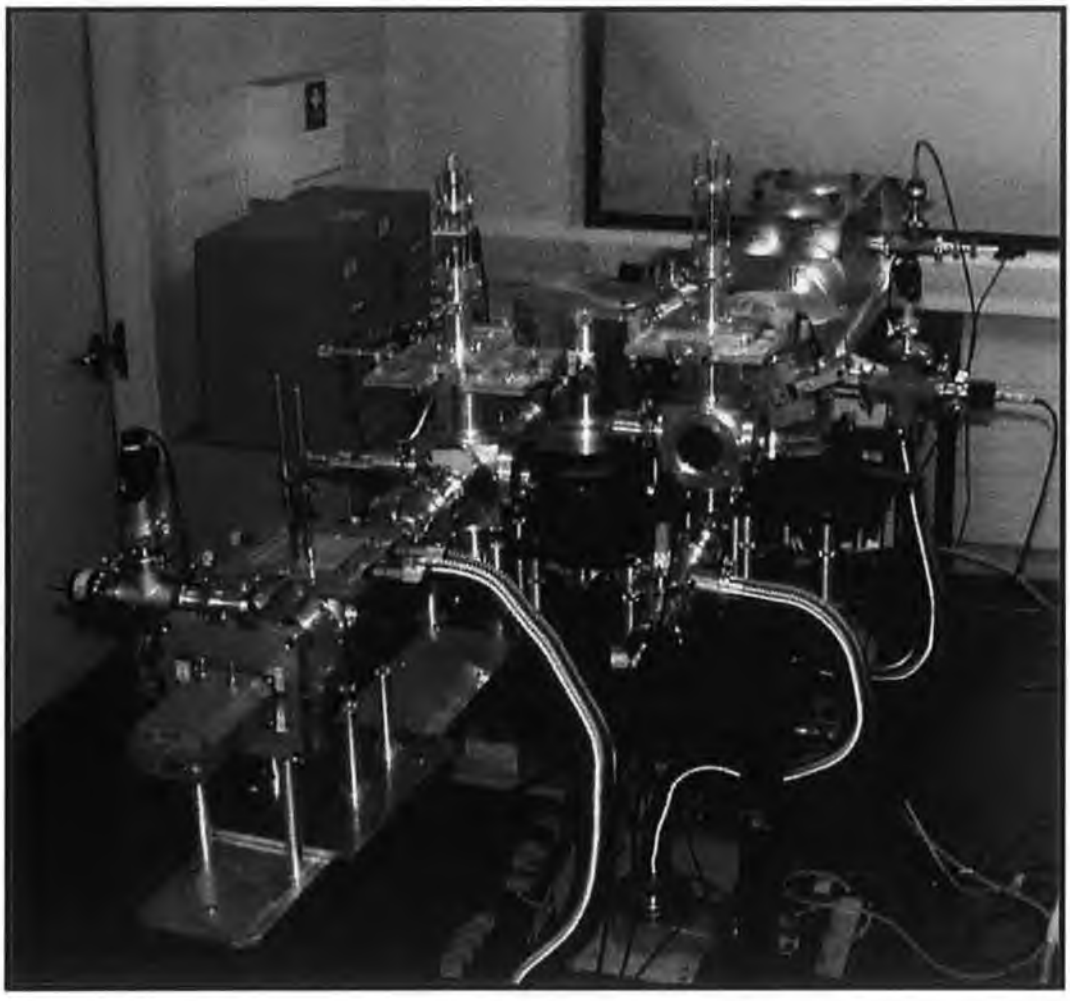

Figure 3.23. Final optical system implemented in the DCU laboratory

3.3.2 System description

As explained in section 3.3.1 we selected the first configuration for the construction of the optical system. A schematic of the system is shown in figure 3.24.

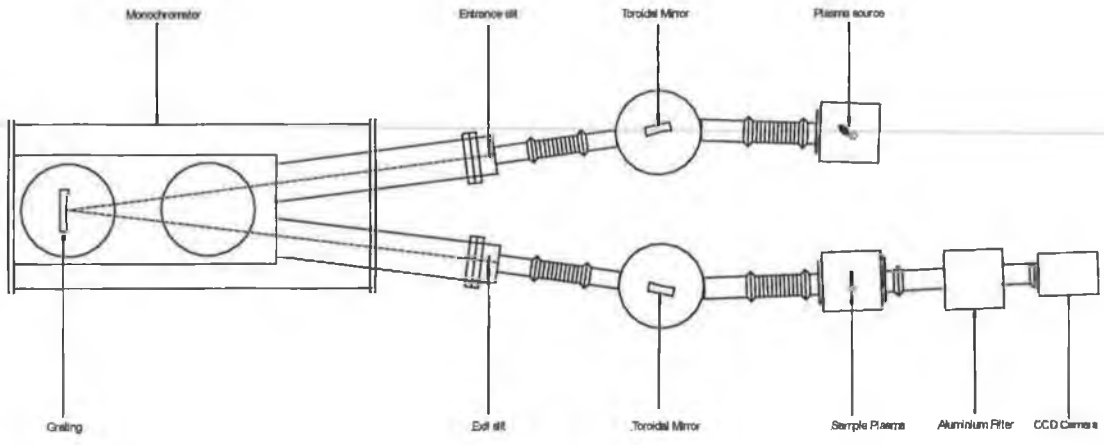

Figure 3.24. DCU experimental set-up

The principle of the experiment is similar to the one explained in section 3.3. The VUV source is focused onto the entrance slit of the monochromator via a toroidal mirror. The wavelength is selected using a 1m normal incidence monochromator and the light emanating out of the exit slit is intercepted by a second toroidal mirror creating a parallel beam of cross section 4 mm x 4 mm. The sample plasma is produced by focusing the radiation of a Nd-YAG laser (SL-400) delivering 300 mJ in 15 ns, and the attenuation of the VUV beam is recorded on a backthinned CCD camera (Andor) with 512×2048, 13 μm size pixels.

3.3.3 VUV light source

Two different laser systems were available to produce the VUV backlighting source: a Continuum laser delivering 0.8 J in 10 ns and a Spectron laser SL 858G delivering 2 J in 10

ns. In this work we used the 0.8 J, 10 ns pulse Nd-YAG laser (Continuum) due to operating failures on the other laser.

A tungsten target was chosen to create the backlighting plasma. However, even though the mirror was located at 400 mm from the plasma source with an incidence angle of 85°, the mirror surface was eventually coated with tungsten debris. The origin of the problem was a combination of two parameters, i.e., the quality of the tungsten rod and a malfunction from the Nd-YAG laser (Spectron SL858G). The Pockels cell was heating due to a design fault in the oscillator stage and resulted in the generation of a long pulse, ~ 100 μs with high energy. This pulse was responsible for a constant drilling of the tungsten target and hence for a very low reproducibility, since the plasma source location moved away from the optical axis, and a considerable amount of tungsten debris. The toroidal mirror had to be re-polished and re-coated.

To test the amount of debris originating from the plasma we replaced the mirror by a microscope glass slide coated with a reflective gold layer. To ensure that the position of the plasma source was located on the optical axis, the output flux, measured by reflection off the gold coated glass plate, was monitored using a photodiode. When the signal disappeared, the target was moved to a fresh surface and its position optimised until the flux was back to its original value. The influence of magnetic fields to deviate the debris in order to avoid coating the mirror was carried out with no successful results, and the use of a helium background gas (Bobkowski *et al.* 1996) was prohibited due to the wavelength region under study < 50 nm. The Spectron laser was subsequently replaced by a continuum laser (800 mJ, 8 ns pulse) and a significant decrease in debris production was observed. A flat homogeneous tungsten target later replaced the tungsten rod, used as a target, which led to further reduction of plasma debris, i.e., there was no evidence of tungsten deposition on the gold coated plate surface after ~ 400000 shots. The experimental work was resumed but after a few days of operation the output flux dropped dramatically.

At first, the spherical grating was checked for any surface coating on a similar 1 m monochromator (Doyle 1995, Dardis 1998) by taking a copper spectrum between 20 and 110 nm. Briefly, the experimental system consists in a 1m normal incidence monochromator identical to the one used in the imaging set-up, the plasma source is located at 30 cm from the entrance slit of the spectrometer and the detector, here a CCD camera, is located on the Rowland circle. Since the spectrometers were identical we could interchange

the grating in this system and compare the spectra having the exact same plasma conditions. The spectra are shown in figure 3.25.

We see in figure 3.25 that the two spectra taken with the two different gratings are very similar, and even though there was no evidence of a debris coating on the mirror, it had to be checked again.

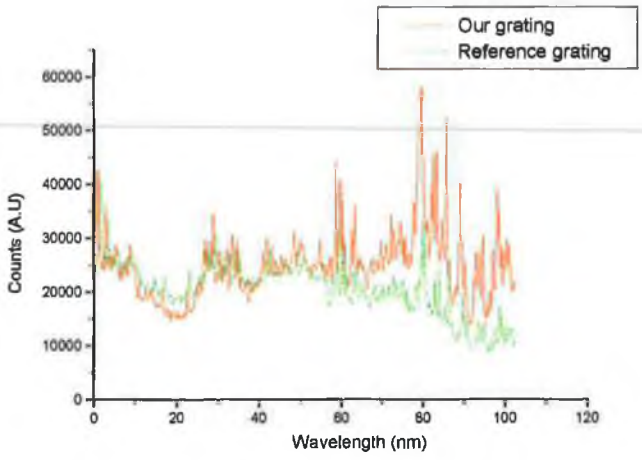

Figure 3.25. Comparison between our grating with possible tungsten coating and a reference grating used in a spectroscopic set-up in the DCU laboratory

Before checking the mirror surface we used the spectroscopic set-up to record a tungsten spectrum with our grating showing no evidence of surface damage. The grating was then replaced in the imaging system and a tungsten spectrum was recorded. For this experiment, the exit arm of the system, i.e., the exit mirror was removed. The exit slit was removed and the CCD camera was located on the Rowland circle at the exit of the monochromator. The entrance arm remained the same with the toroidal mirror focusing the plasma light onto the entrance slit of the monochromator. A tungsten spectrum was taken in these conditions in the same wavelength range. The two spectra are compared in figure 3.26. Figure 3.26. shows a cut off in the output flux at around 55 nm, which does not occur in the spectrum recorded without the entrance mirror.

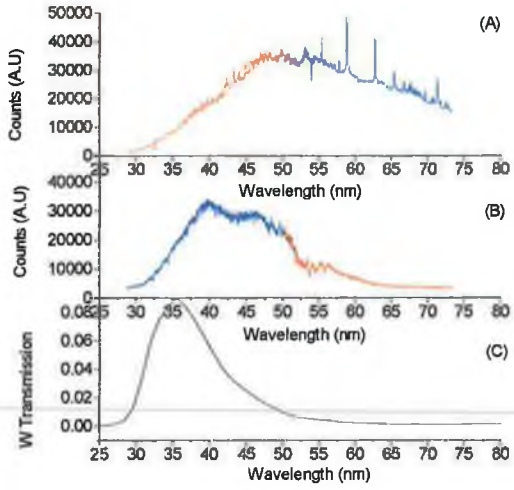

Figure 3.26. Comparison of a tungsten spectrum using the same grating, (A) without the entrance mirror and (B) with the entrance mirror. (C) is a plot of the tungsten transmission as a function of wavelength

On the plot of the tungsten transmission as a function of wavelength, we notice that the decrease in the output flux follows the decrease in the tungsten reflectivity indicating the presence of a very thin layer of tungsten on the mirror surface. The decision was taken to produce the continuum VUV source with a gold target where the addition of a thin layer of gold on the mirror surface wouldn't influence the mirror reflectivity.

3.3.4 Vacuum system

3.3.4.1 Target chambers

The system incorporates three target chambers. Two chambers are used to house the backlighting plasma and the sample plasma and a third one supports an aluminium filter. All three target chambers are similar, i.e., 127 mm × 127 mm aluminium cubes with 70 mm diameter holes on each six sides. In figure 3.27. we show the system of co-ordinates describing the target lens arrangement for the two chambers housing a laser plasma.

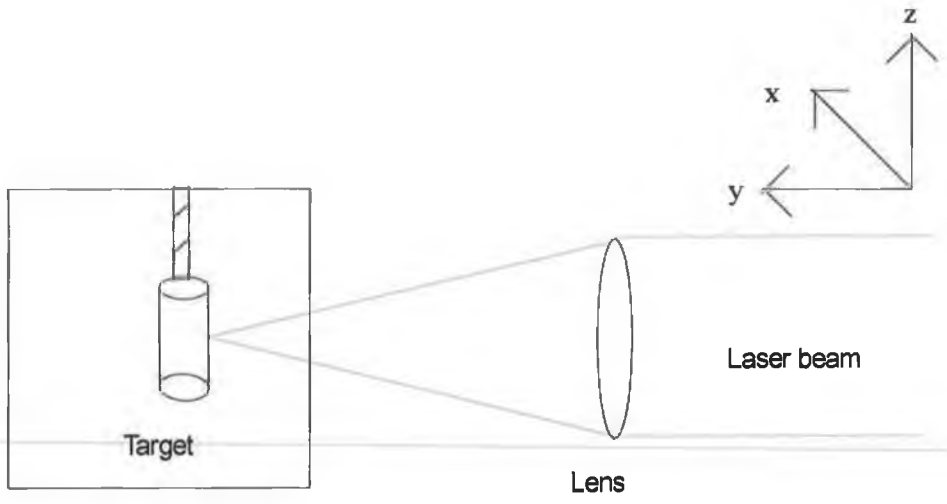

Figure 3.27. System of co-ordinates chosen to describe the movement of the lens with respect to the target chamber.

3.3.4.2 VUV source target chamber

In this experiment we use a gold rod of 10 mm length, 6 mm diameter mounted on a x, y, z translation stage fitted on top of the chamber. The target can be moved up and down, and along the z axis in order for the laser beam to interact with a fresh target surface. Moreover movements along the x and y directions are crucial for positioning of the plasma source on the optical axis. The opposite bottom port is connected to the pumping ring, which consists of a combination of a rotary and a turbomolecular pump (Leybold PT 50). The typical operating pressure is below 10^{-5} mBar.

The laser beam enters into the chamber through a custom-made window flange attached to one of the side ports. The laser light is focused to a point (~ 100 μm diameter) using a spherical lens of 100 mm focal length and 30 mm diameter. The lens holder is mounted on a optical breadboard and allows movements along the x, y and z directions. On the opposite port a custom made flange is attached to the chamber holding a thin aluminium plate with a 1 mm^2 aperture acting as a shield to prevent debris from reaching the surface of the mirror. Another window flange is attached to the fifth port, which can support a Helium Neon laser used for the target *al.*ignment. Finally, the remaining port is attached to a custom made flange connecting the chamber with the rest of the system through a KF-40 vacuum connector.

A photograph of the chamber is shown in figure 3.28.

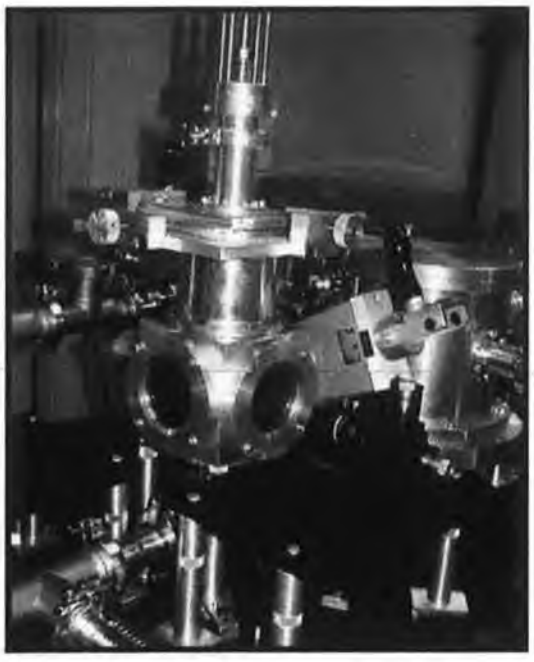

Figure 3.28. Photograph of the target chamber housing the backlighting plasma

3.3.4.3 Sample plasma target chamber

The arrangement of this chamber is very similar to the backlighter target chamber. The sample target here is a flat calcium or barium slab, attached to a holder mounted on the top of the chamber, providing x, y, z movements. Two opposite ports are fitted with custom-made flanges with KF-40 end-pieces connecting the chamber to the rest of the system. The bottom port is connected to a similar pumping rig, i.e., rotary and turbomolecular pump combination.

A window flange allows the laser radiation to interact with the target and a cylindrical lens is used to focus the laser beam to a line of ~ 3 mm by 0.2 mm. The lens is mounted on a similar holder fitted on an optical breadboard. The lens and the target have x, y, z movements to facilitate the positioning of the target with respect to the VUV probe beam. Opposite the widow flange, a custom made flange is attached, holding a knife-edge used to reduce the front plasma emission on the CCD detector, protect the aluminium filter and define a clear edge on the recorded images. The knife edge can move in and out along

the y-axis. Figure 3.29. shows a photograph of the target chamber incorporated in the system.

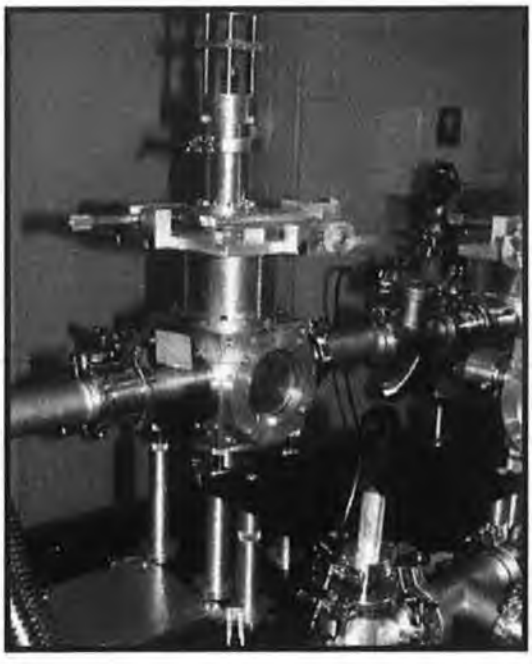

Figure 3.29. Photograph of the target chamber housing the sample plasma

3.3.4.4 Aluminium filter holder

Contrary to the first set-up where the aluminium filter was fitted in a modified KF-50 T-piece, here a separate chamber was used to centre the filter on the optical axis. The problem arose from the construction of the mirror chamber where the exit port angle was machined at 15° instead of the 10° required. The angle was compensated to 10° but the VUV beam was off-centre with respect to the mechanical arrangement. As the aluminium filter was centred in the KF connector, it was then blocking the path on the probe beam. The filter was consequently fitted in a target chamber connected to a holder allowing x, y, and z movement. A baffle was added to ensure for light tightness.
To reduce the risk of filter damage due to pumping and plasma debris, the size of the filter was limited to 5 mm^2 for a thickness of 0.2 or 0.4 μm.

There is a non negligible difference between the transmission of the two filters (see figure 3.24). To limit further loss of light flux, a 0.2 μm filter will be used when possible, i.e., when the sample front plasma emission intensity isn't too large. During experiments,

the laser energy as well as the knife-edge position is optimised in order to reduce the front plasma emission and operate with a 0.2 μm filter. Figure 3.30. shows the aluminium filter chamber – CCD camera arrangement.

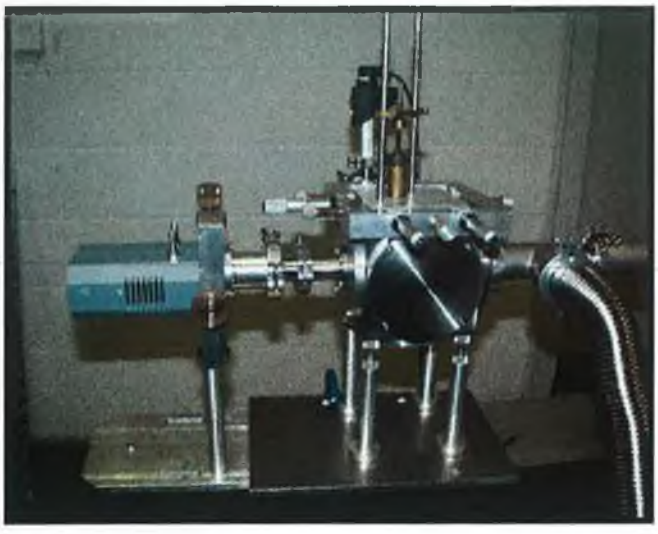

Figure 3.30. Photograph showing the target chamber housing the aluminium filter, with the x, y, z translation stage holding the filter fitted on top of the chamber

3.3.4.5 Mirror chambers

The mirror chambers used in this set-up were built according to mechanical drawings provided by the University of Padova. They consist of an aluminium cylindrical body fitted with four exit ports, a permanent base plate on which the cylinder is bolted and a removable top plate allowing fine adjustments on the mirror mount. Two of the four ports make an angle of 10° to agree with the chosen angle of incidence on the mirror. A vacuum compatible mirror mount is placed in the centre of the chamber, translations along the y and z axis are possible for fine positioning adjustments. The angle of incidence on the mirror was selected by rotating the mirror around its axis: coarse and fine rotation adjustments are permitted.

A mask which consists of a thin aluminium plate of 40 mm × 45 mm, with an aperture of 4 mm × 4 mm to limit the aperture of the system is attached to the mirror holder. A photograph of the mirror chamber is shown in figure 3.31.

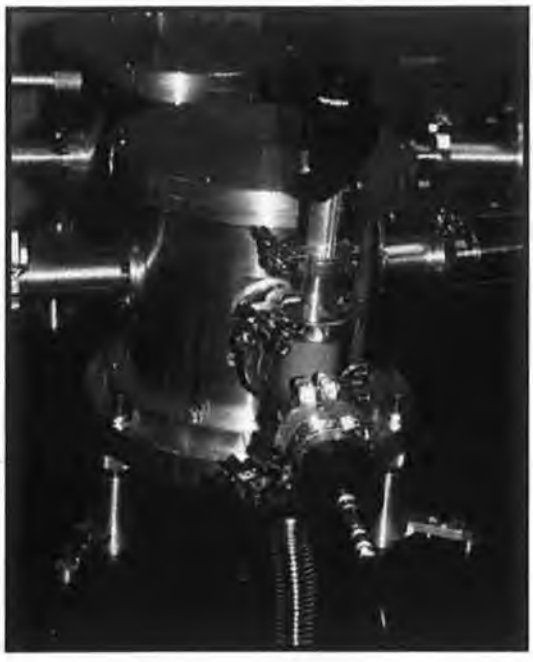

Figure 3.31. Photograph of the mirror chamber

3.3.4.6 Acton Research Corporation™ 1 meter normal incidence spectrometer

The Acton Research Corporation™ 1 meter normal incidence spectrometer is fitted with an exit slit and used as a monochromator in this set-up. A PT-360 (Leybold) pumping rig is used to evacuated the monochromator to pressures down to 10^{-7} mbar. The monochromator is equipped with a 1200grooves/mm spherical concave, iridium coated grating and covers the range from 30 to 325 nm, however the system is optimised to operate in the 30 to 100 nm range. The spectrometer specifications are summarised in table 3.6.

VM-521 Specifications (1200g/mm Grating)	
Operating range	30 nm to 325 nm
Focal length	1000 mm
Dispersion	0.83 nm/mm
Optical system	Normal Incidence Concave Grating
Angle between Entrance and Exit ports	15 Degrees
Aperture ratio	F/10.4 (tangential plane) F/17.5 (sagittal plane)

Table 3.6. Specifications of the VM-521 Acton research monochromator

In figure 3.32.we show a photograph of the VM-521 monochromator.

Figure 3.32. Photograph of the VM-521 monochromator incorporated in the imaging system

3.3.4.7 Laser system and synchronisation

Four different Nd-YAG systems are available in the "VUV laboratory" and are used either to produce the backlighting plasma or the sample plasma. The Spectron SL-400 was used during the course of this work to create the calcium or barium plasma. It comprises an oscillator stage only and can deliver 300 mJ in 15 ns at a repetition rate of 10 Hz. This laser

was synchronised to a Continuum™ Surelite laser, which produced the backlighting plasma. The Continuum laser operates at a repetition rate of 10 Hz delivering 800 mJ in 10 ns.

Two other lasers were purchased a Spectron SL-858G, comprising an oscillator and an amplifier stage, delivering 2J in 10 ns at a repetition rate of 10 Hz. This laser was acquired in hope of increasing the backlighter emission, but was not used in this work due to a design flaw. As the main part of the experiment consisted of time resolved studies, a picosecond laser system was acquired to gain better time resolution. The EKSPLA™ laser delivers 500 mJ in 150 ps at a repetition rate of 10 Hz. This laser was not used in the present work but will be used in the VUV imaging system in the future.

The Spectron SL-400 and the Continuum lasers were synchronised using two Stanford DG 535 delay generators controlled by the CCD detector. The first delay generator was set as the time reference T_0, and used to trigger the flashlamps of both lasers. A TTL pulse of 10 ms was connected to the continuum laser triggering the flashlamps at 10 Hz. A second output consisting of a similar TTL pulse was amplified to 15 V and connected to the SL400 laser. The flashlamps of both lasers are continuously being triggered at 10 Hz following the recommendation of the respective manufacturers.

The T_0 output of the delay generator was used to trigger the second delay generator ensuring time synchronisation. Two output pulses were delayed by 180 ms, the optimum delay between the laser flashlamp and Pockels cell trigger, and connected the respective Pockels cells of the lasers. The output pulse connected to the SL-400 Pockels cell trigger had to be amplified to 15 V. A variable delay was inserted between the two lasers, with a jitter of ± 1ns, providing time delays between 0 ns (overlapped pulses) and a few microseconds. These two outputs were connected to the lasers Pockels cells via an "AND" gate controlled by the CCD camera. When the CCD camera exposure begins, a pulse relayed by a trigger box is sent to the "AND" gate, which is then opened for the duration of the exposure time, permitting the Pockels cells of the lasers to be triggered. Both lasers are then firing at a repetition rate of 10 Hz, and when the exposure time is terminated, the gate closes again and the lasers stop firing. In this configuration, the number of shots is determined by the exposure time set with the CCD camera software. A timing diagram is shown in figure 3.33.

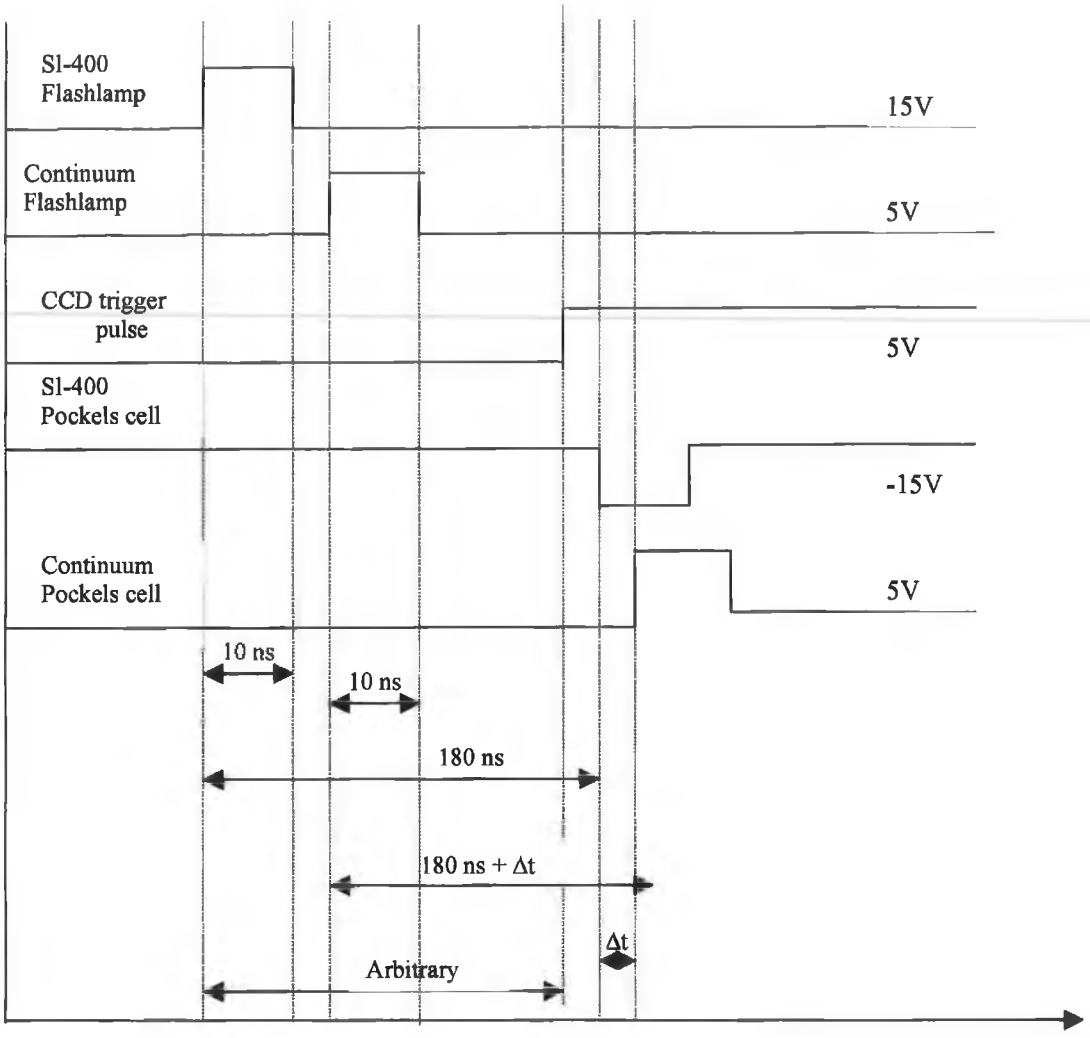

Figure 3.33. Timing diagram of the laser system synchronisation

The typical exposure time used during this work was 1 s corresponding to 10 laser shots. The target (backlighter) was moved to a fresh surface every 50 shots. The detected flux on the CCD camera integrated over the area of the VUV beam, i.e., 4 mm^2 has been plotted as a function of the number of laser shots in figure 3.34.

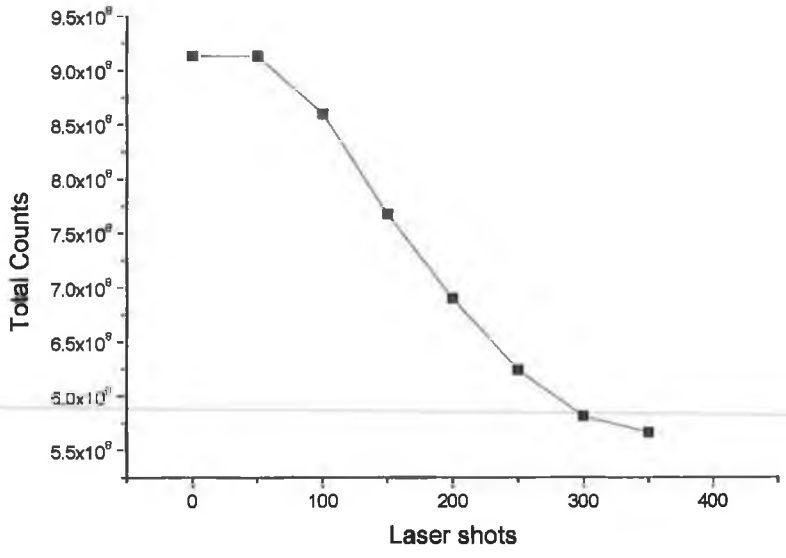

Figure 3.34. Stability of the detected flux over the area of the VUV beam as a function of the number of laser shots

It is clear from figure 3.34 that the VUV flux detected on the CCD camera is constant for the first 50 shots and then decreases monotonically. The data acquisition procedure was chosen accordingly and 5 series of 10 shots were used for each acquisition before moving to a fresh target surface.

3.3.5 Ray tracing

In this section we will derive the parameters necessary for the ray tracing phase of this work, i.e., the monochromator, and toroidal mirrors optical parameters. We present the results of the ray tracing code and compare with direct experimental measurements. The derivation of the different equations will not be given here, as they have been derived in section 3.2.

3.3.5.1 Monochromator simulation

The monochromator used in this experiment was a VM-521 Acton Research monochromator, with specifications shown in table 3.6. The monochromator parameters,

i.e., the angle of incidence on the grating, the diffracted angle and the position of the primary and secondary foci were calculated using the same equations given in section 3.1. Here the subtented angle between the entrance and exit ports of the monochromator is 15°.

$$\alpha - \beta = 15^{\circ} \qquad [3.19]$$

Using equations [3.4] and [3.7], the angle of incidence α is given by:

$$\alpha = 7.5^{\circ} + \arcsin\left(\frac{m\lambda}{2d\cos(7.5)}\right) \qquad [3.20]$$

The system was ray-traced for four different wavelengths, 30 nm, 50 nm, 70 nm and 100 nm, constituting the wavelength region of interest for this work. α and β were calculated for these four different wavelengths and the results are summarised in table 3.7.

Wavelength	*Incidence angle α*	*diffracted angle β*
30 nm	8.54 °	6.46 °
50 nm	9.23 °	5.76 °
70 nm	9.93 °	5.07 °
100 nm	10.97 °	4.03 °

Table 3.7. Calculated incident and diffracted angles for four wavelength settings

The position of the primary focus is given by:

$$r = R\left(\frac{\cos^2(\alpha)+\cos^2(\beta)}{\cos(\alpha)+\cos(\beta)}\right) \qquad [3.14]$$

In a similar fashion, the position of the secondary focus r' (spatial focus) is given by the following equation:

$$\frac{1}{r'} = \frac{\cos(\alpha)+\cos(\beta)}{R} - \frac{1}{r} \qquad [3.5]$$

The values of r and r' calculated at 30 nm, 50 nm, 70 nm, and 100 nm, are shown in table 3.8.

Wavelength	*horizontal focus r*	*vertical focus r'*
30 nm	986.72 mm	1022.21 mm
50 nm	986.45 mm	1023.11 mm
70 nm	986.02 mm	1024.50 mm
100 nm	985.14 mm	1027.48 mm

Table 3.8. Position of the horizontal and vertical focus of the VM-521 Acton Research monochromator for different wavelengths (the positions are measured from the center of the grating)

3.3.5.2 Computed mirror parameters

The parameters of the two toroidal mirrors were calculated using the classical optical geometric equations [3.9], [3.10]:

$$\frac{1}{p}+\frac{1}{q}=\frac{2}{R\cos(\alpha)}$$ in the Tangential plane

$$\frac{1}{p}+\frac{1}{q}=\frac{2\cos(\alpha)}{\rho}$$ in the Sagittal plane

with p and q being respectively the object to mirror distance and the image to mirror distance. R is the radius of curvature in the tangential plane and ρ is the radius of curvature in the sagittal plane. α is the angle of incidence and is set at 85°. The tangential lies normal to the plane defined by the vertical slits and the sagittal plane is parallel to it, i.e., perpendicular to the tangential plane. The entrance mirror operates in the Rowland circle condition. p and q were chosen to be 400 mm each so that the radius of curvature in the tangential plane is calculated to be 4590 mm.

In the sagittal plane we still have p = q = 400 mm and the radius of curvature is calculated to be 34.9 mm. The exit mirror is located at 400 mm from the exit slit and is

designed to produce a parallel beam. Hence, the value of q was set to infinity, i.e., $\frac{1}{q} = 0$ in both planes.

The radii of curvature were calculated to be R = 9180 mm in the tangential plane and ρ = 69.7 mm in the sagittal plane. This value was optimised to 63.5 mm using different ray tracing simulations. A summary of the values needed for the ray tracing phase is summarised in table 3.9.

Entrance mirror	
Shape	Toroidal
Incidence angle	85 degrees
Entrance arm	400 mm
Exit arm	400 mm
Tangential radius	4590 mm
Sagittal radius	34.9 mm
Mirror size	60 mm × 20 mm
Angle of acceptance	10 mrad × 10 mrad
Exit mirror	
Shape	Toroidal
Incidence angle	85 degrees
Entrance arm	400 mm
Tangential radius	9180 mm
Sagittal radius	63.5 mm
Mirror size	60 mm × 20 mm

Table 3.9. Computed parameters of the entrance mirror, the exit mirror and the monochromator used in the ray tracing simulations

3.3.5.3 Aberrations and mirror reflectivity

The numerical aperture of the system is f/100 × f/100, while the angle of incidence on the entrance and exit mirrors was set at 85° to maximise the reflectivity of each mirror. The ray tracing code was used to monitor any aberration on the entrance slit of the monochromator that would result in flux loss. The simulation was run for a point like source at a wavelength of 50 nm and for an angle of incidence of 85° and a number of different angles of acceptance. The results are shown in figure 3.35.

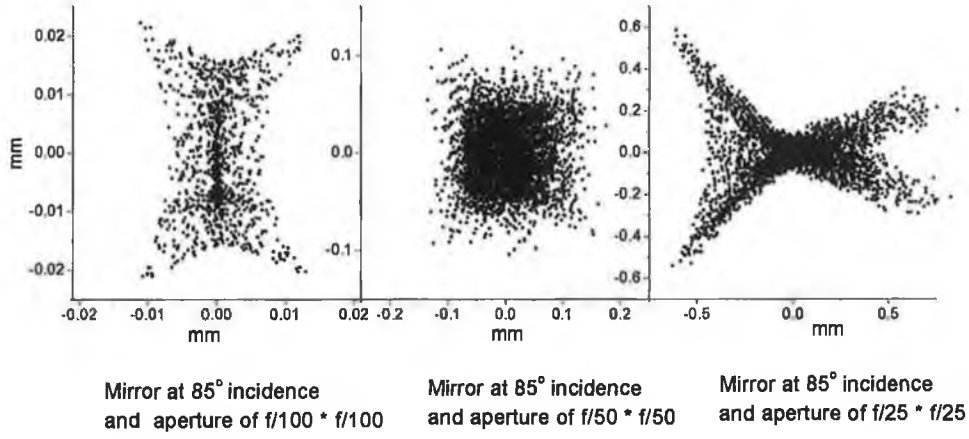

Figure 3.35. Predicted vacuum ultraviolet 'footprints' of the laser plasma source on a plane located at the entrance slit of the 1 meter normal incidence monochromator for different angles of acceptance

We clearly see from figure 3.35 that at an angle of 85° incidence, the aberrations are larger than 100 μm for an acceptance angle of 20 × 20 mrad (f/50) and more than 1 mm for an acceptance angle of 40 × 40 mrad (f/25). For an aperture of 10 × 10 mrad (f/100), the size of the image of a point source is less than 40 μm, indicating no loss of light flux at the entrance slit of the monochromator. We note that increasing the numerical aperture at a grazing incidence angle results in important aberrations. As a consequence, the gain in flux due to the larger aperture is cancelled out by the light lost at the entrance slit of the monochromator.

Both toroidal mirrors were coated with gold on a sub-layer of chromium. The reflectivity of a gold-coated surface is plotted in figure 3.36 for different angles of incidence and wavelengths between 30 nm and 110 nm.

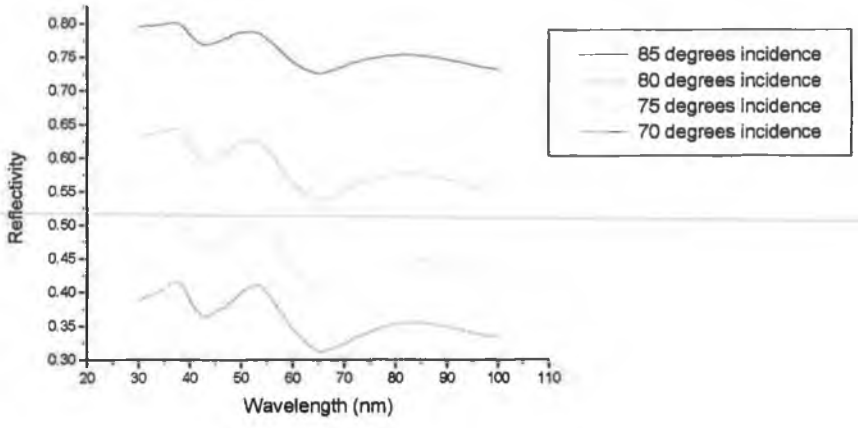

Figure 3.36. Reflectivity of a gold coated surface as a function of the angle of incidence for wavelengths between 30 nm and 110 nm

The reflectivity of the gold mirror is increased by a factor of two when the angle of incidence is increased from 70° to 85°. Even if aberrations are larger for grazing incidence angles, it turns out that the configuration here, combining an angle of incidence of 85° and an numerical aperture of f/100 × f/100, is the optimum to ensure minimum flux loss.

3.3.6 System performances

3.3.6.1 Spectral resolution

The spectral resolution of the system was first determined using the ray tracing program and compared with experimental measurements. The spectral resolution was computed for different entrance and exit slit combinations, at 30 nm, 50 nm, 70 nm and 100 nm. The first calculations were performed with 50 μm entrance and exit slit widths. Subsequently calculations were performed with entrance/exit slit widths of 100 μm/ 100 μm and 140 μm / 140 μm. A particular combination was tested to monitor the influence of the exit slit width

on the spectral resolution: the exit slit width was set at 100 μm while the entrance slit width was 50 μm.

Using the ray tracing code, once the slit widths have been set, the number of rays exiting the monochromator at a particular wavelength (30nm, 50 nm, 70 nm, 100 nm) were recorded and taken as a reference. The wavelength was then increased in small $\delta\lambda$ steps (here 0.02 nm) until 50% of the initial flux was lost. The corresponding wavelength interval is written as $\Delta\lambda_1$. The same wavelength scan is repeated when decreasing the wavelength and the second interval is written as $\Delta\lambda_2$.

The resolving power is then given by:

$$R = \frac{\lambda}{\Delta\lambda_1 + \Delta\lambda_2} \qquad [3.15]$$

The results are shown in figure 3.37.

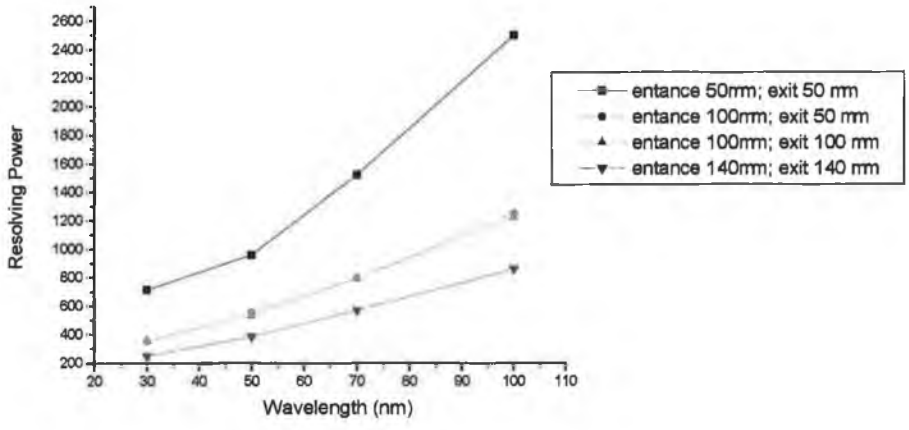

Figure 3.37. Computed resolving power for different entrance and exit slit width combinations

The most significant feature in figure 3.37 is the comparison between the configurations showing an entrance and exit slit set at 50 μm and an entrance slit width of 50 μm with the exit slit was opened to 100 μm. The two curves describing the resolving power are nearly identical, indicating that the resolving power is mainly determined by the width of the entrance slit of the monochromator. Thus, it is possible to increase the exit slit width to 100 μm and gain output flux without altering the spectral resolution. With a 50 μm

entrance slit width, the resolving power is ~1000 at a wavelength of 50 nm, and more than 2000 at 100 nm. The system being optimised to operate with 50 μm entrance and exit slit, this configuration will be used when possible to achieve high spectral resolution. However, considering the width of the transition under study in this work and the available flux, all results were obtained using an entrance and exit slit width of 100 μm.

These computed results were checked experimentally using absorption spectroscopy. We measured the He $1s^2$-1s 2p absorption resonance at 58.43 nm. The Helium pressure (P) in the target chamber was held in the range of 0.17 mbar < P < 0.19 mbar and the absorbing column length (L) was ~ 900 mm. The experimental procedure was as follows. The pixels on the CCD camera were binned 64 x 64 resulting in pixels of size 0.832 mm x 0.832 mm to maximise the detected flux. Due to the large area of the "superpixels", single shot data acquisition was possible, thus preventing the formation of craters on the target surface and giving us better stability on the output flux. A set of images were taken scanning the wavelength from 58.2 nm to 58.50 nm in 0.02 nm steps. Four "superpixels" were isolated on every image and the number of counts per pixel were added for every wavelength. The results are plotted in figure 3.38 for matched entrance and exit slits widths of 50 μm and 100 μm each. The spectral resolution is extracted from each curve by measuring their full width at half maximum.

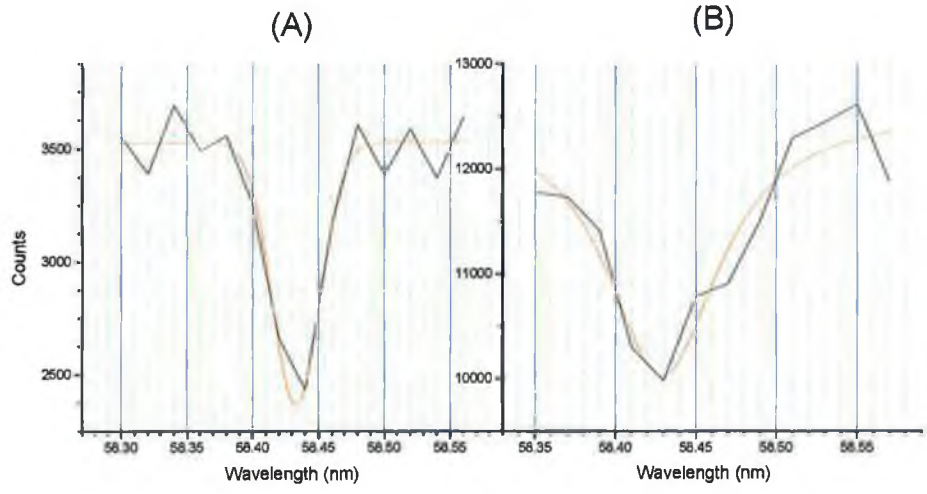

Figure 3.38. Measured spectral resolution using the He 1s2 – 1s2p resonance line at 58.43 nm, with (A) 50μm / 50μm entrance/exit slit and (B) 100μm / 100μm entrance/exit slit

For an entrance and exit slit of 100 μm, the best fit to the data is a Gaussian fit of width 0.085 nm (FWHM). The data are best fitted with a Gaussian curve of width 0.04 nm (FWHM) when operating with an entrance and exit slit of 50 μm. These experimental values correspond to resolving powers of 687 (± 80) and 1460 (± 70) at 58.43 nm and compare well with ray tracing which predicts resolving powers of 660 and 1200 respectively at 58.43 nm.

3.3.6.2 Spatial resolution

The spatial resolution in the horizontal and vertical plane has been measured using the same procedure as for the first optical system. Briefly a knife-edge was inserted into the path of the VUV beam in both the tangential and sagittal planes. By isolating a row (or column for the vertical resolution) on the 2 dimensional image, we obtain the edge trace. By differentiating the latter we obtain then the line spread function, and the full width at half maximum of the best fitted curve will give the spatial resolution of the system. The edge trace and the corresponding line spread function in the horizontal plane are plotted in figure 3.39. The signal is very noisy and even more so when differentiating the edge trace, hence we only plotted the relevant part of the graph to obtain a more accurate fit. The pixels were binned 4 x 4 for these measurements because of flux limitations giving an effective pixel size (superpixel) of 52 μm.

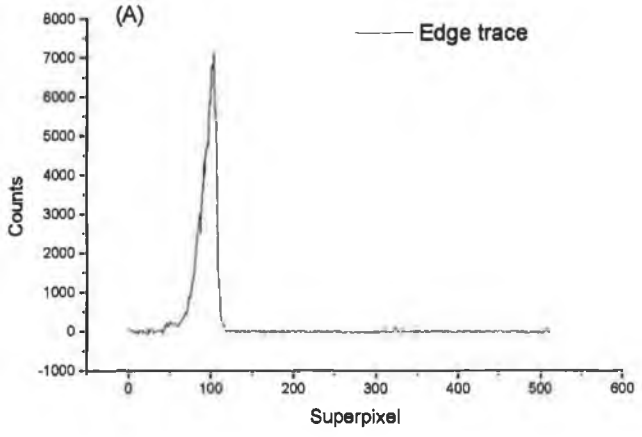

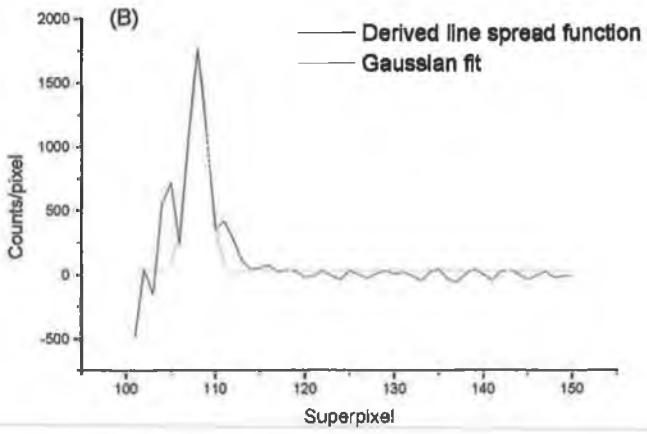

Figure 3.39. Determination of the horizontal spatial resolution, with (A) the edge trace and (B) the derived line spread function

Here, the best fit is a Gaussian curve of width 120 μm ± 10 μm corresponding to the spatial resolution of the system with an entrance and exit slit of 100 μm. In the vertical plane the spatial resolution is calculated following the same procedure and the results are shown in figure 3.40.

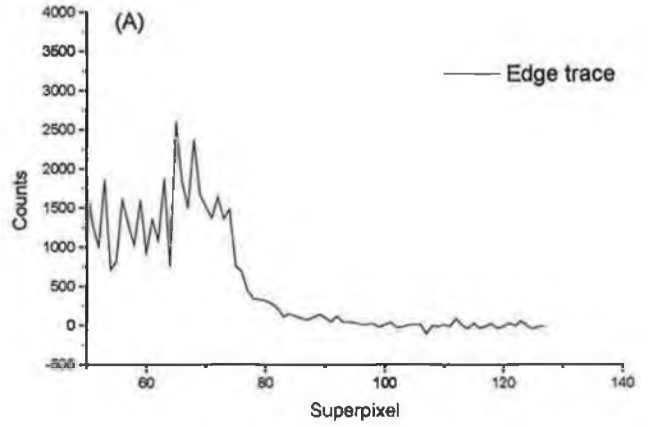

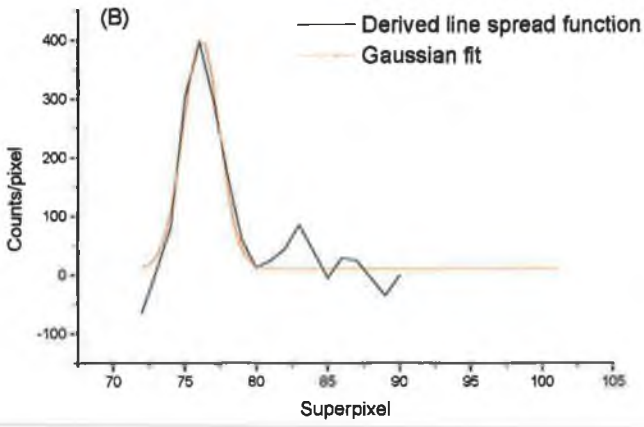

Figure 3.40. Determination of the vertical spatial resolution, with (A) the edge trace and (B) the derived line spread function

Here again, the line spread function is best fitted by a Gaussian function of full width at half maximum of 160 μm ± 15 μm corresponding to the vertical spatial resolution of the system. This value is independent of the size of the entrance and exit slit width since the resolution in the vertical plane is mainly determined by the size of the VUV source.

To understand the variation of the horizontal spatial resolution with the width of the exit slit we used ray-tracing simulations. A pinhole was located at the sample plasma position and its image was recorded in a plane located at the CCD camera position. The calculations have been repeated at 9 different points covering the spatial extent of the VUV beam in the CCD camera plane and the results were constant within the area. Three different entrance and exit slit widths were used, i.e., 50 μm/50 μm, 100 μm/100 μm and 140 μm/140 μm. The results are summarised in table 3.10.

Slits width	Horizontal resolution	Vertical resolution
50 μm	65 μm	180 μm
100 μm	130 μm	180 μm
140 μm	170 μm	180 μm

Table 3.10. Computed spatial resolution in the horizontal and vertical plane using the ray tracing code

We see that for an entrance and exit slit of 100 μm, the values obtained using the ray tracing program agree well with the experimental measurements. In this work, due to the low VUV flux in the monochromatic beam, the experiments were performed using an entrance and exit slit width of 100 μm, resulting in a horizontal resolution of 130 μm and a vertical resolution of 180 μm.

3.3.6.3 Footprint and collimation

The VUV beam exiting the monochromator is a quasi monochromatic beam with a bandwidth defined by the width of the exit slit. This beam is collimated by the exit arm toroidal mirror producing a parallel beam of cross section 4 mm × 4 mm. The footprint of the beam can be monitored at any distance from the mirror using the ray tracing code and the beam divergence can thus be estimated.

The footprint of the probe beam has been calculated for three different wavelengths (30 nm, 50 nm, 100 nm) and at two distances from the exit mirror, i.e., 550 mm and 1050 mm.

The results are shown in figure 3.41.

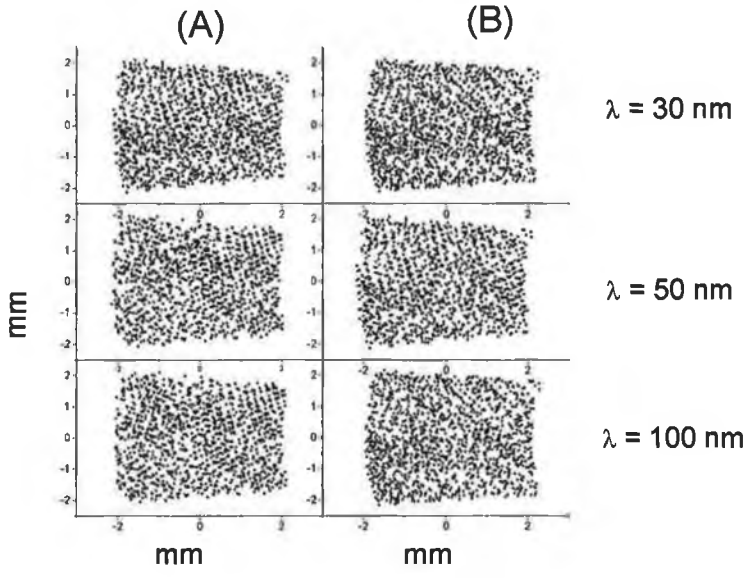

Figure 3.41. Calculated footprint using the ray tracing code for different wavelengths at (A) 550 mm and (B) 1050 mm from the exit mirror

These results have been obtained using a elliptical source of 140 μm × 100 μm in the ray tracing simulations with an entrance and exit slit width of 50 μm on the monochromator. The calculated size of the VUV beam is (at 550 mm from the exit mirror) 4.3 mm × 4 .0 mm at 30 nm, 4.2 mm × 4.2 mm at 50 nm and 4.2 mm × 4.0 mm at 100 nm. At 1050 mm from the exit slit the simulation gives similar footprints of 4.2 mm × 4 .2 mm at 30 nm, 4.1 mm × 4.2 mm at 50 nm and 4.2 mm × 4.3 mm at 100 nm. The relatively small number of rays (2000 at the viewing position) spread over ~ 4 mm × 4 mm makes the error on the measurement of the footprint very large and to calculate the beam divergence with these data would not constitute a reliable result. Thus, the divergence of the VUV beam will be extracted from the measured footprint shown in figure 3.42. To measure the footprint of the VUV beam, the CCD detector has been placed at the same positions, i.e., 550 mm and 1050 mm, and the full width at half maximum of the footprint is calculated at each position.

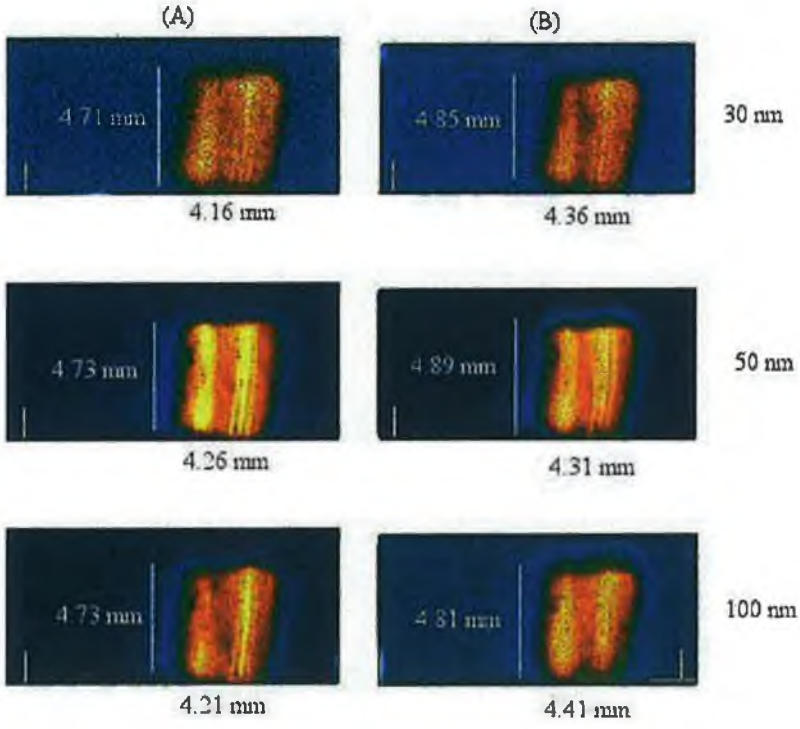

Figure 3.42. Measured footprint of the VUV beam for different wavelengths at (A) 550 mm and (B) 1050 mm from the exit mirror

The images are plotted on the same colour scale, which shows the difference in intensity with respect to the wavelength. The size of the VUV beam agrees well with the ray tracing predictions and by taking the average size (FWHM) of the beam at 550 mm and 1050 mm we can determine a divergence of 0.3 mrad ± 0.01 mrad in the horizontal plane and 0.25 mrad ± 0.01 mrad in the vertical plane.

3.4 Summary

The two optical set-ups used in this work have been described and their individual performances have been characterised. The first system or prototype system used a diverging beam of divergence 30 mrad in the horizontal plane and 14 mrad in the vertical plane. The flux loss at the entrance slit of the monochromator was estimated to be ~ 70 % and constituted one of the main concerns for future development of the technique. The spectral resolution was poor, reaching values from 30 at 30 nm to 100 at 100 nm. This was the result of the use of a wide entrance slit width to compensate for the flux loss. The spatial resolution had a value of 360 μm in the horizontal plane and of 420 μm in the vertical plane.

The system designed and implemented in the DCU laboratory was an answer to these problems and limitations. To facilitate the data analysis and be in agreement with the conditions to derive the equation of radiative transfer, we decided to use a collimated beam of cross section 4 mm x 4 mm as a probe beam. The problem of the loss of light flux at the entrance slit of the monochromator was solved by replacing the spherical mirror by a toroidal mirror, thereby eliminating most of the losses. The performance of the system was considerably improved. In our mode of operation, i.e., with entrance and exit slit widths of 100 μm, the spectral resolution has values ranging from 400 at 30 nm to 1200 at 100 nm. Finally, the spatial resolution has been improved to 130 μm in the horizontal plane and to 180 μm in the vertical plane.

Chapter 4

Results and analysis

4 Overview

In this chapter we begin by reviewing the work to date on the photoionisation of atomic and ionic calcium and barium in the VUV. We present then the results obtained using both the prototype system at the Rutherford Appleton Laboratory and the results obtained using the system built in the DCU laboratory. We present, in turn, time and space resolved photoioinisation studies using the 3p-3d resonance of neutral calcium, Ca^{+}, Ca^{2+} and of the 5p – 6d resonance of Ba^{+} ions. The final results are extracted from the images recorded with the DCU system where the spatial resolution, the spectral resolution and the signal to noise ratio have been improved substantially. We demonstrate how to extract column density values from maps of equivalent width recorded directly from the experiments for Ca^{+} and Ba^{+} species for which the absolute cross sections have been measured at the Daresbury (UK) synchrotron (Lyon *et al.* 1986, 1987). A discussion on the plasma expansion dynamics is included in this chapter where experimental values are compared with predictions obtained using the Singh and Narayan (1990) expansion model. Here we restrict ourselves to the determination of the plasma atomic species expansion velocity only, which can be extracted directly from the photoabsorption images.

Calcium studies

4.1.1 Introduction: Photoionisation of calcium and calcium ions

For the last two decades, calcium, and especially the 3p region of the spectrum has been the subject of numerous studies both theoretical and experimental. Mansfield (1977) carried out an extensive photoabsorption study of neutral calcium in the wavelength range between 30 and 80 nm with a particular emphasis on the 3p –3d transitions. His study revealed a very rich spectrum dominated by a very strong absorption feature at 39.48 nm, and at the same time, he proposed a non-relativistic theoretical approach as an explanation to the complexity of this spectrum. In a situation where the $4s^2$ subshell remains unaffected, one of the most probable transitions is the following:

$$3p^6\,4s^2\,(^1S) \rightarrow 3p^5\,4s^2\,nd\,(^1P)$$

Looking at the potential curves for "nd" electrons in figure 4.1, one notices that for n = 3 the potential well is deeper than for n = 4 to 6 where it remains identical. As a consequence, since the 3p orbital is confined to a region close to the nucleus (r < 2 a.u.) a considerable overlap between the 3p and 3d wavefunctions is observed leading to a substantial increase in the oscillator strength of the 3p – 3d transition.

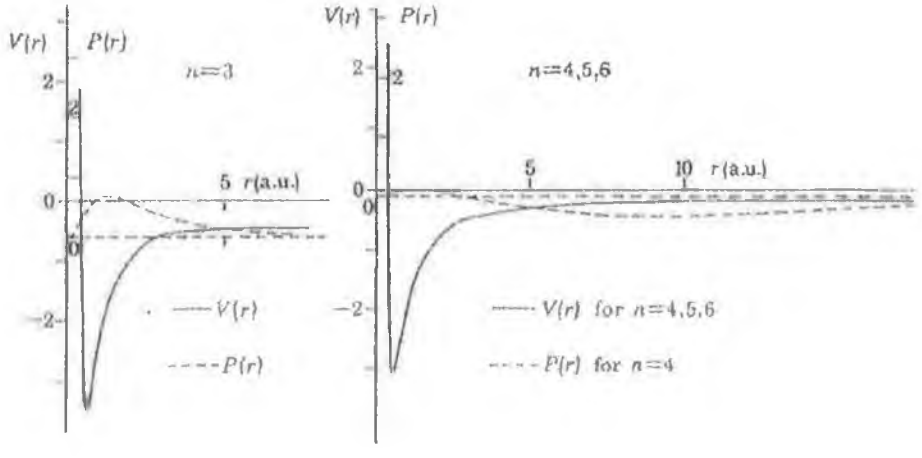

Figure 4.1. Effective potential V(r) and wavefunctions P(r) for nd electrons in calcium $3p^5 4s^2 nd$ configurations (from Mansfield 1977)

Calculations on the photoionisation cross section of calcium by Altun (1983, 1985) with excitation to the 3d level confirmed the existence of the 3p –3d "giant resonance" near 39 nm. Further relativistic studies by Connerade (1992) confirmed that strong configuration mixing within the inner shell excited states rather than spin orbit splitting was the origin of the complexity of the calcium spectrum in the 3p – 3d excitation region.

Experimentally, the 3p – 3d transitions in neutral calcium, Ca^+ and Ca^{2+} have been investigated using a wide range of techniques. Sato *et al.* (1985) used a time of flight mass spectrometer, and synchrotron radiation as a light source, to study single and double photoionisation of atomic calcium in the 35 to 42 nm range showing good agreement with the results of Mansfield (1977). Bizau *et al.* (1987) performed photoelectron spectroscopy and uncovered a wealth of complex ionisation thresholds in Ca^+ corresponding to shake up processes such as:

$$Ca\,(4s^2) + h\nu \rightarrow Ca^+\,(4s) + e^-$$
$$\rightarrow Ca^+\,(3d) + e^-$$

Ueda *et al.* (1993) subsequently performed angle resolved photo-electron spectroscopy to determine the partial photoionisation cross-section of calcium corresponding to ionisation of the different subshells (3p, 4s …). Finally, Van Kampen *et al.* (1995) used the Dual Laser Plasma technique to record the absorption spectrum of Ca^{2+} between 22 nm and 49 nm.

We will concentrate our attention on two particular experiments, which have led to the measurement of the absolute cross section of the Ca^+ ions and especially the 3p – 3d resonance at 37.34 nm, which is studied in this work.

Lyon *et al.* (1987) measured the absolute photoionisation cross section of Ca^+, by merging a VUV synchrotron radiation beam, with wavelength ranging from 28.2 nm to 49.8 nm, with a beam of ground state Ca^+ ions. A schematic of the experimental apparatus is shown in figure 4.2.

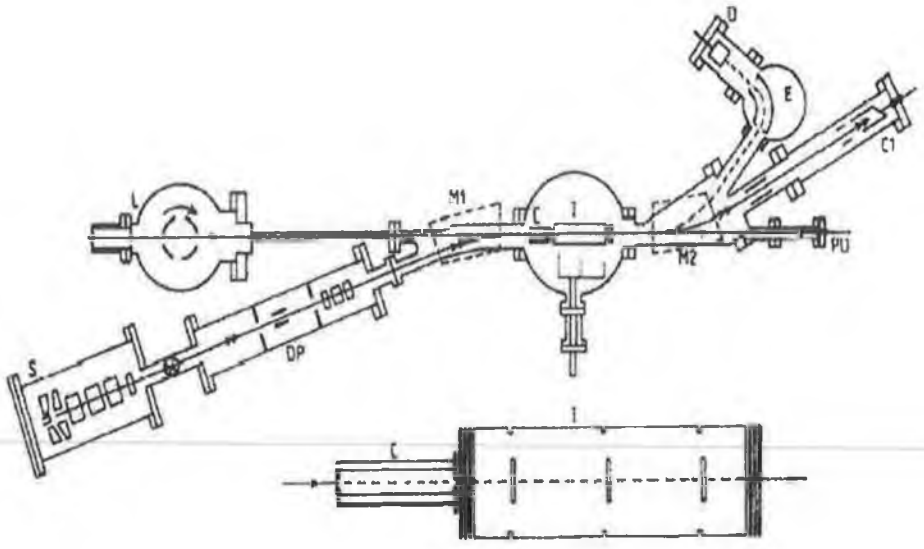

Figure 4.2. Experimental set-up, where L is a rotating chopper wheel, S is the Ca+ ion source, DP is a differential pumping tank, M1 is the first deviating magnet, C is a pair of slits, I is a biased cylinder, M2 is the second deviating magnet, PD is a photodiode, C1 is a faraday cup, E is an electrostatic analyser, and D is a Johnston multiplier (from Lyon *et al.* 1987)

The experiments performed at the Daresbury Laboratory (UK) were the first ever measurements of the absolute photoionisation cross-section for an ion and a real experimental tour de force. The Ca^+ ion beam produced in the surface ionisation source S was first mass analysed using the magnet M1 and then collimated to form a 2 mm × 3 mm cross section beam. It was then merged with a monochromatic beam of synchrotron radiation whose wavelength was selected using a 5 meter normal incidence Mc Pherson monochromator. The Ca^+ ions were then collected in a Faraday cup whereas the Ca^{2+} ions, following a second deflection by the magnet M2 and an electrostatic analyser were detected individually by a calibrated Johnston multiplier.

The absolute photoionisation cross section of Ca^+ was measured from 28.2 nm to 49.2 nm. We show in figure 4.3, the absolute cross section around the 3p –3d resonance at 37.34 nm, which we used in this work to detect and follow the evolution of Ca^+ species in an expanding calcium plasma plume.

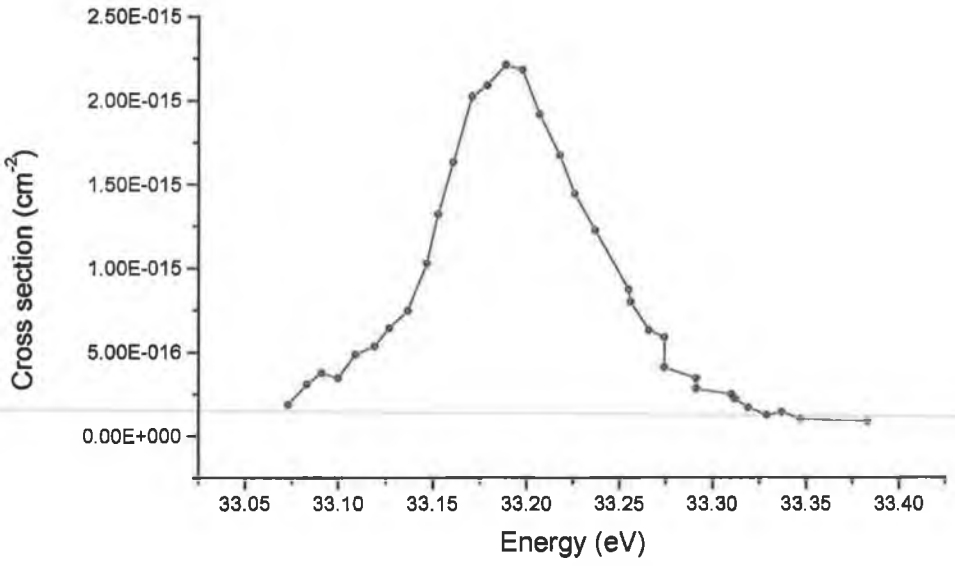

Figure 4.3. Absolute cross section of the Ca^+ 3p – 3d resonance centred at 33.19 eV (37.34 nm) (from Lyon *et al.* 1987)

In a second pioneering experiment, Bizau *et al.* (1991) measured the first ever photoelectron spectrum of an ion. A schematic of the experimental set-up is shown of figure 4.4.

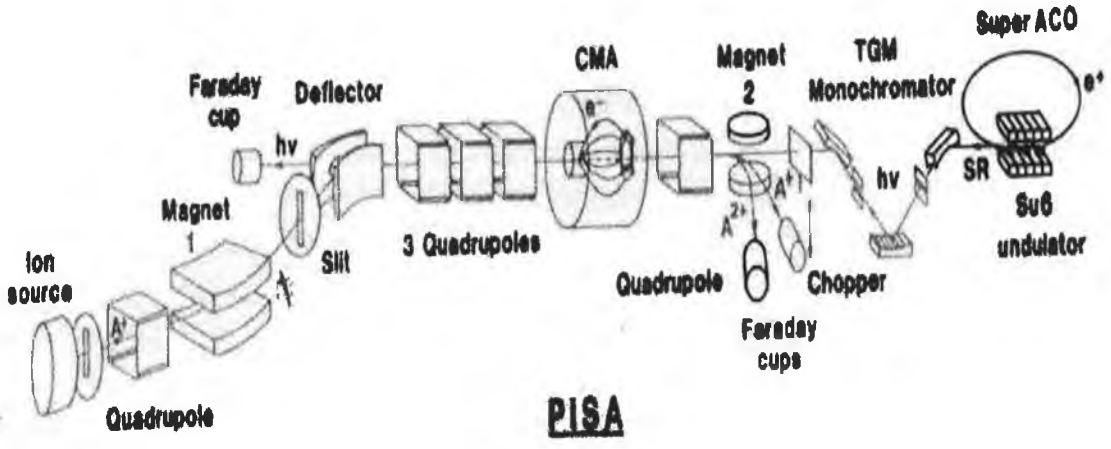

Figure 4.4. Experimental set-up used by Bizau *et al.* (1991)

A beam of Ca^+ ions was formed in the ion source and further focused into the cylindrical mirror electron analyser. Monochromatic light emanating from the SU6 undulator beamline at Super ACO was also, in turn, focused into the cylindrical mirror electron analyser and the electrons emitted were analysed at an angle close to the magic angle using high-counting-rate channeltrons. The results were in good agreement with the previously published results of Lyon *et al.* (1987). The Ca^+ 3p –3d resonance appears at 37.34 nm (peak) and is shown in figure 4.5.

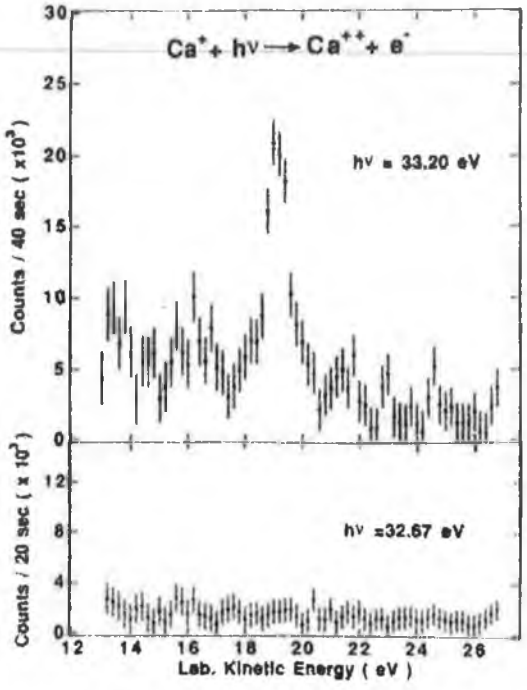

Figure 4.5. Photoelectron spectra measured using a Ca^+ ion beam with 33.2 eV photons

We have chosen calcium as a first atomic and ionic candidate to demonstrate the feasibility of the VUV photoabsorption imaging technique mainly because of the large value of the VUV photoionisation cross-section. As we are dealing with a resonant photoionisation process, the cross section values are increased due to the presence of intermediate autoionizing states. In particular, we focused our attention on the 3p –3d transitions in neutral calcium, Ca^+ and Ca^{2+} at respectively 39.48 nm, 37.43 nm and 35.73 nm. The photoioinisation processes studied can be written as:

$$Ca\ (3p^6\,4s^2\ {}^1S) + h\nu \rightarrow Ca^*\ (3p^5\,4s^2\,3d\ {}^1P) \rightarrow Ca^+\ (3p^6\,4s\ {}^2S) + e^-$$

$$Ca^+\ (3p^6\,4s\ {}^2S) + h\nu \rightarrow Ca^{+*}\ (3p^5\,4s\,3d\ {}^2P) \rightarrow Ca^{2+}\ (3p^6\ {}^1S) + e^-$$

For the case of Ca^{2+}, we are faced with a resonant photoexcitation process only, which can be written as:

$$Ca^{2+}\ (3p^6\ {}^1S) + h\nu_{absorbed} \rightarrow Ca^{2+*}\ (3p^5\,3d\ {}^1P) \rightarrow Ca^{2+}\ (3p^6\ {}^1S) + h\nu_{emitted}$$

In this case we would have to deal with the more general form of the radiative transfer equation (i.e., including stimulated and spontaneous emission processes). This point illustrates the main motivation underlying the use of inner shell photoionisation resonances to track ions in plasmas.

As the knowledge of the absolute cross section is an essential condition to derive maps of column density, we have chosen to study the Ca^+ 3p – 3d resonance (σ = 2200 Mb) at 37.34 nm as test species. At the same time the excitation energy of this resonance was within the wavelength range of our apparatus and in a wavelength region where the flux of the backlighter was high. The technique could be further validated by studying the neutral calcium 3p - 3d resonance at 39.48 nm and a bound state of Ca^{2+} using the 3p – 3d resonance at 35.73 nm. To extract accurate maps of column density we had to be certain that the transition used was uniquely distinct from interference by transitions (absorption lines) of adjacent ion stages likely to be present in the calcium plasma plume. We used the results of a photoabsorption study of calcium plasmas carried out by A. Gray (1999), using the Dual Laser Plasma technique to ensure this condition for neutral calcium, Ca^+ and Ca^{2+}. The recorded spectra are shown in figure 4.6.

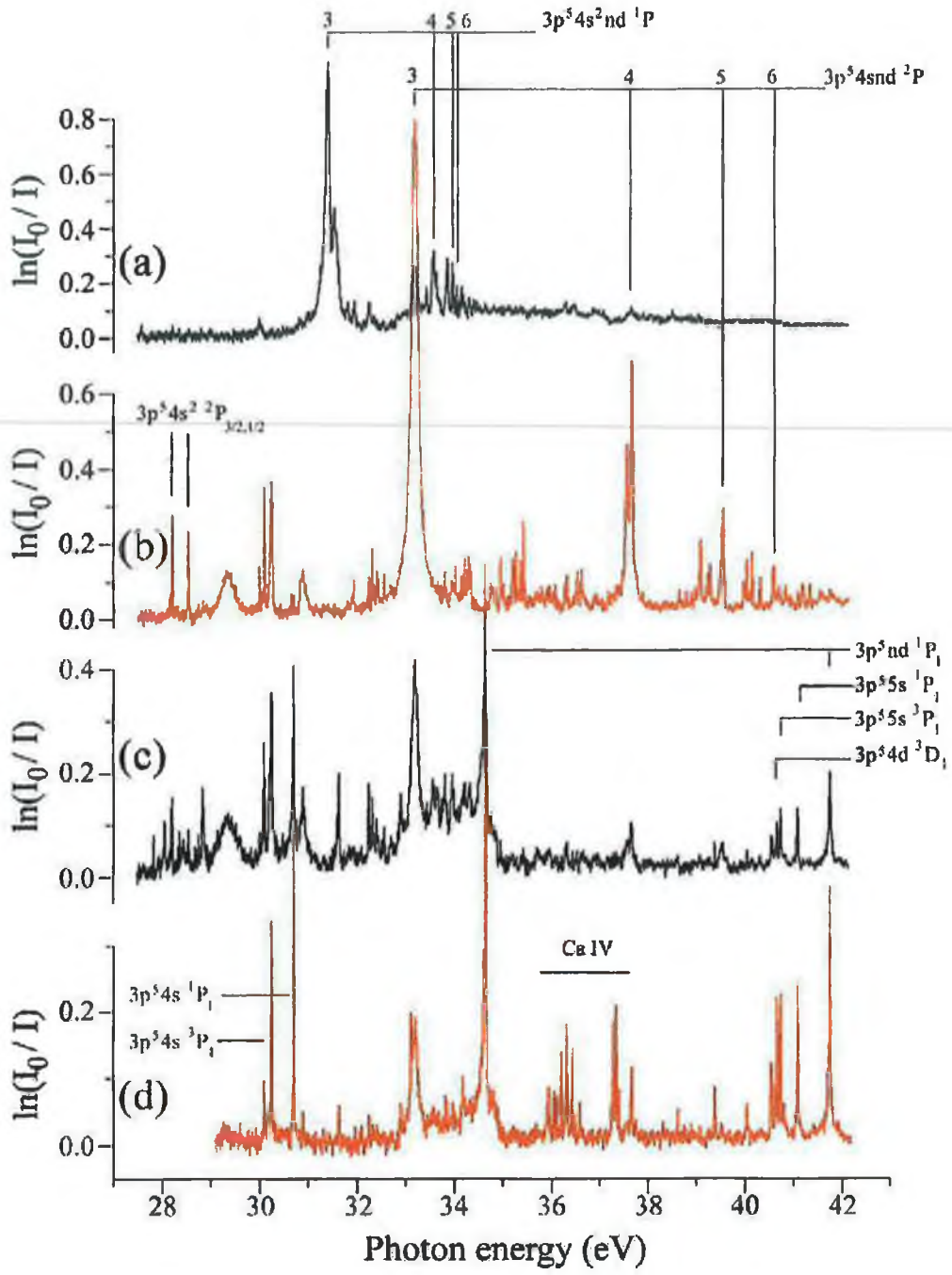

Figure 4.6 : Calcium isonuclear sequence in photoabsorption where (a) is Ca^0 (ΔT=800ns, cylindrical lens), (b) is Ca^+ (ΔT=500ns, cylindrical lens), (c) is Ca^{2+} (ΔT=20ns, cylindrical lens) and (d) is Ca^{2+} (ΔT=45ns, spherical lens)(After Gray 1999)

The bandwidth of the VUV beam emanating from the monochromator is ~ 0.1 nm with 100 μm entrance and exit slit widths. From figure 4.6 we see that the 3p – 3d transitions in Ca, Ca^+ and Ca^{2+}, can be uniquely selected without interference from resonances in neighbouring ion stages. Of course, at any one space-time point we would expect to have all three species in the plume with varying proportions. Hence, we would expect to obtain an absorption signal due to direct photoionisation of neutral species plus the resonance, e.g., at 37.34 nm we would have $N_+\sigma^+$ (3p – 3d + 4s direct)L + N_0 σ^0 (4s direct)L.

The Ca^{2+} ionisation threshold lies well above 37.34 nm and hence it does not contribute to photoionisation. Since σ^+ (3p – 3d + 4s direct) is 2200 MB compared to less than 1 MB for the σ^0 (4s direct) and we measure an absorption signal, we can neglect the direct neutral absorption signal.

4.1.2 Data acquisition

We used the same data acquisition procedure in the two experiments. Firstly, a background image was recorded without any laser being fired and was saved as a first background (Bg 1). An image of the backlighting plasma was then recorded with background (Bg 1) subtraction, and saved as $\int_{\Delta\lambda} I_0(\lambda)d(\lambda)$ where $I_0(\lambda)d(\lambda)$ is the VUV fluence in Jcm^{-2} between λ and λ + d λ falling on each pixel of the detector. The sample plasma was created and an image of the plasma emission was recorded and saved as a second background (Bg 2). Finally both lasers were triggered at a set time delay and the resulting photoabsorption image was recorded with background (Bg1 + Bg2) subtraction. This image was then saved as $\int_{\Delta\lambda} I(\lambda)d\lambda$ where I(λ)d λ represents the transmitted VUV fluence between λ and λ + d λ.

Using these images a map of equivalent width was created, defined by the following expression:

$$W_\lambda = \Delta\lambda \times \frac{\int_{\Delta\lambda} I_0(\lambda)d\lambda - \int_{\Delta\lambda} I(\lambda)d\lambda}{\int_{\Delta\lambda} I_0(\lambda)d\lambda} \qquad [4.1]$$

The ANDOR basic software enables easy handling of the image files on which the usual arithmetic operations can be applied. Time and space resolved maps of equivalent width are thus created by subtracting the image of transmitted intensity from the image of the backlighter signal and the result is divided by the image of the backlighter as shown in equation [4.1]. The ANDOR software is able to handle "divide by 0" operations, the pixels concerned are attributed a "NAN" (Non-Attributed Number) value which can be replaced during data processing, by a 0 value.

Data analysis at RAL

In the experiment carried out at RAL, the images of both the transmitted and backlighter signal were recorded after 10 shots, and data processing was carried out with these values. The shadowgram of the backlighter was used for, on average, 10 successive images (of 10 shots each) corresponding to 10 different time delays before a new image was recorded. This introduced errors in the measurements and we will discuss this problem in detail in the next section.

Data analysis in DCU

In the experiment performed in the DCU laboratory, 5 series of 10 shots were used to record the data, the emission of the sample plasma being high, the accumulation of 50 shots would have saturated the detector. We used 5 x 10 shots on the same target position since the signal of the backlighter doesn't decrease significantly after the first 50 shots (see chapter 3). However a shadowgram of the backlighter was recorded for each series of shots at every time delay and the data were processed as follows:

Let I_1, I_2, I_3, I_4, I_5 be the recorded images of the backlighter, and I_{01}, I_{02}, I_{03}, I_{04}, I_{05} the recorded images of the transmitted signal. We define I the image of the accumulated

backlighter signal and I_0 the image of the accumulated transmitted signal and the equivalent width is calculated to be:

$$W_\lambda = \Delta\lambda \times \frac{I_0 - I}{I_0} \qquad [4.2]$$

with

$I = I_1 + I_2 + I_3 + I_4 + I_5$

$I_0 = I_{01} + I_{02} + I_{03} + I_{04} + I_{05}$

This process was repeated for every time delay for the study of both calcium atoms/ions and barium ions.

4.1.3. Maps of equivalent width

The first step in deriving maps of column density is to record time and space resolved maps of equivalent width, which can be obtained directly from the experiment. We first present photoabsorption images recorded at RAL using the prototype system in figure 4.7, 4.8, and 4.9. We show time and space resolved maps of equivalent width of neutral calcium using the 3p-3d resonance line at 39.48 nm, of Ca^+ using the 3p-3d resonance at 37.34 nm and of Ca^{2+} using the 3p-3d resonance at 35.73 nm. These images were recorded following the data acquisition procedure described in section 4.1.2 with pixels binned 8 × 8 on the CCD camera to compensate for the low incident flux.

The backlighting source was produced using a KrF laser (248 nm, 170 mJ, 20 ns) focused to a point of 100 μm diameter, resulting to a power density on target of ~ 1 x 10^{11} $W.cm^{-2}$. The sample plasma was produced using a Nd-YAG laser (1064 nm, 300 mJ, 10 ns) focused to a horizontal line of 8 mm length and 200 μm width, resulting in a power density on target of ~ 2 x 10^9 $W.cm^{-2}$. In these images, the target surface is located at the top of the images with the plasma expanding from top to bottom.

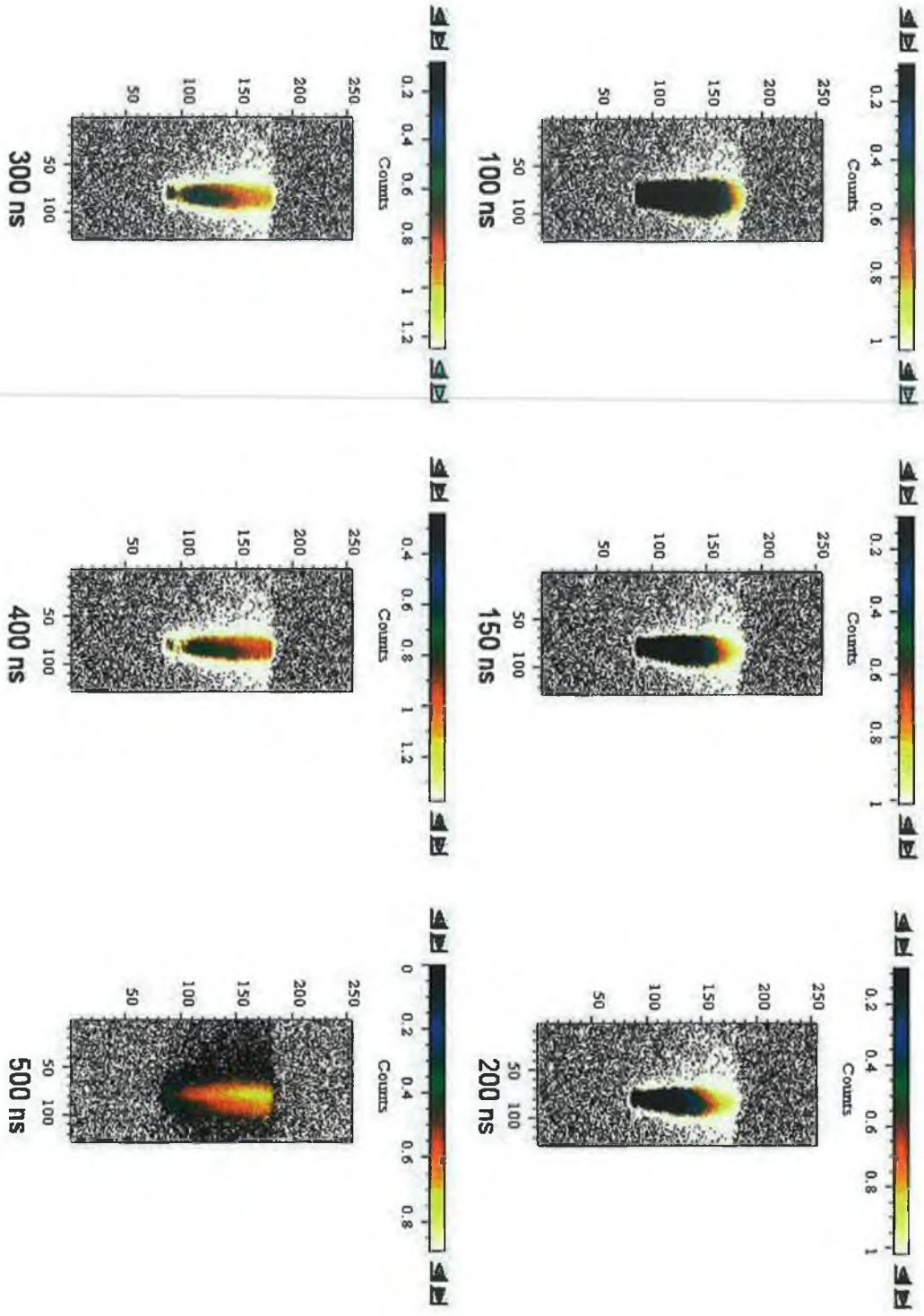

Figure 4.7. Time and space resolved maps of equivalent width in Angstrom of neutral calcium using the 3p-3d resonance at 39.48 nm

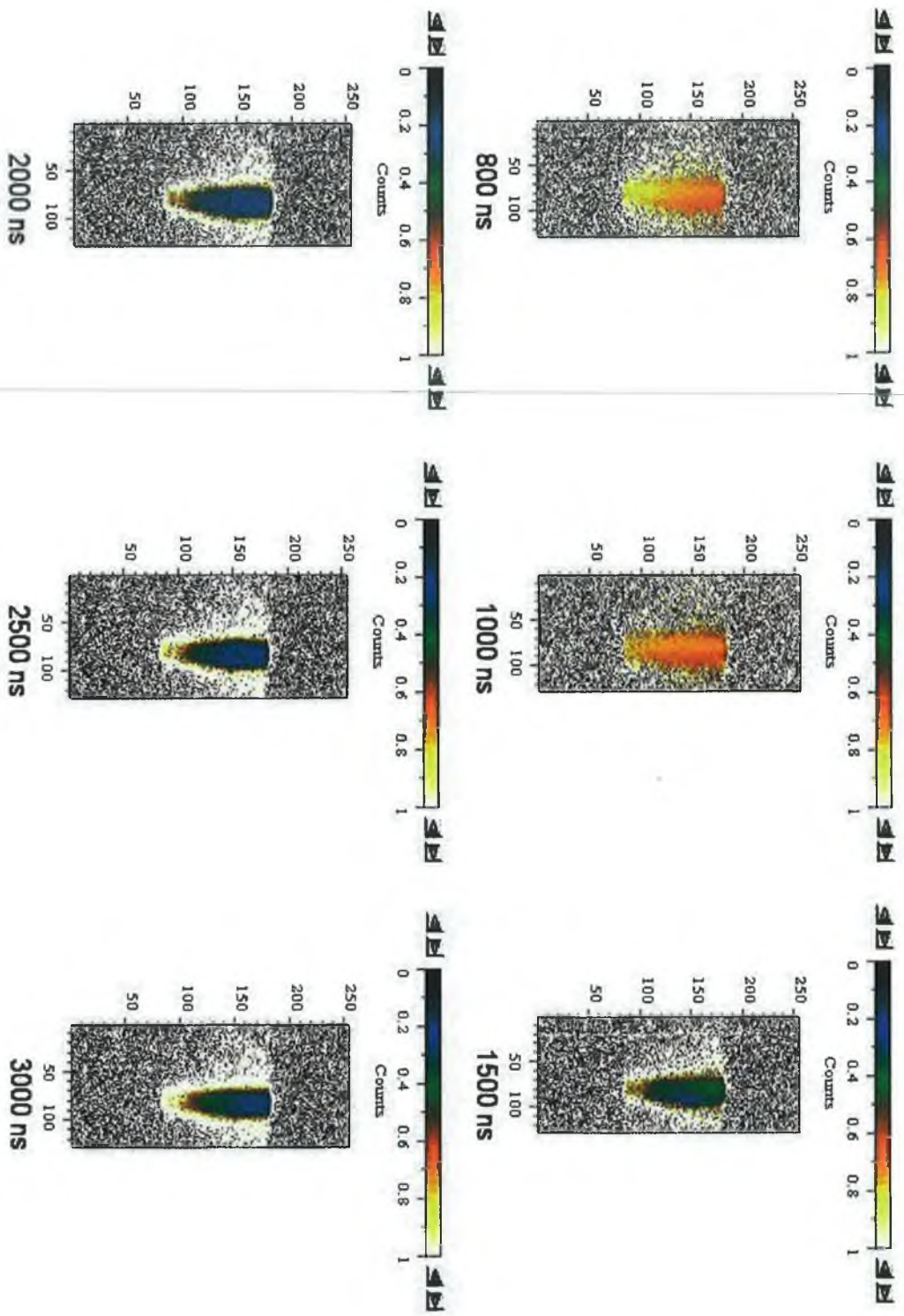

Figure 4.7 (cont) Time and space resolved maps of equivalent width in Angstrom of neutral calcium using the 3p-3d resonance at 39.48 nm

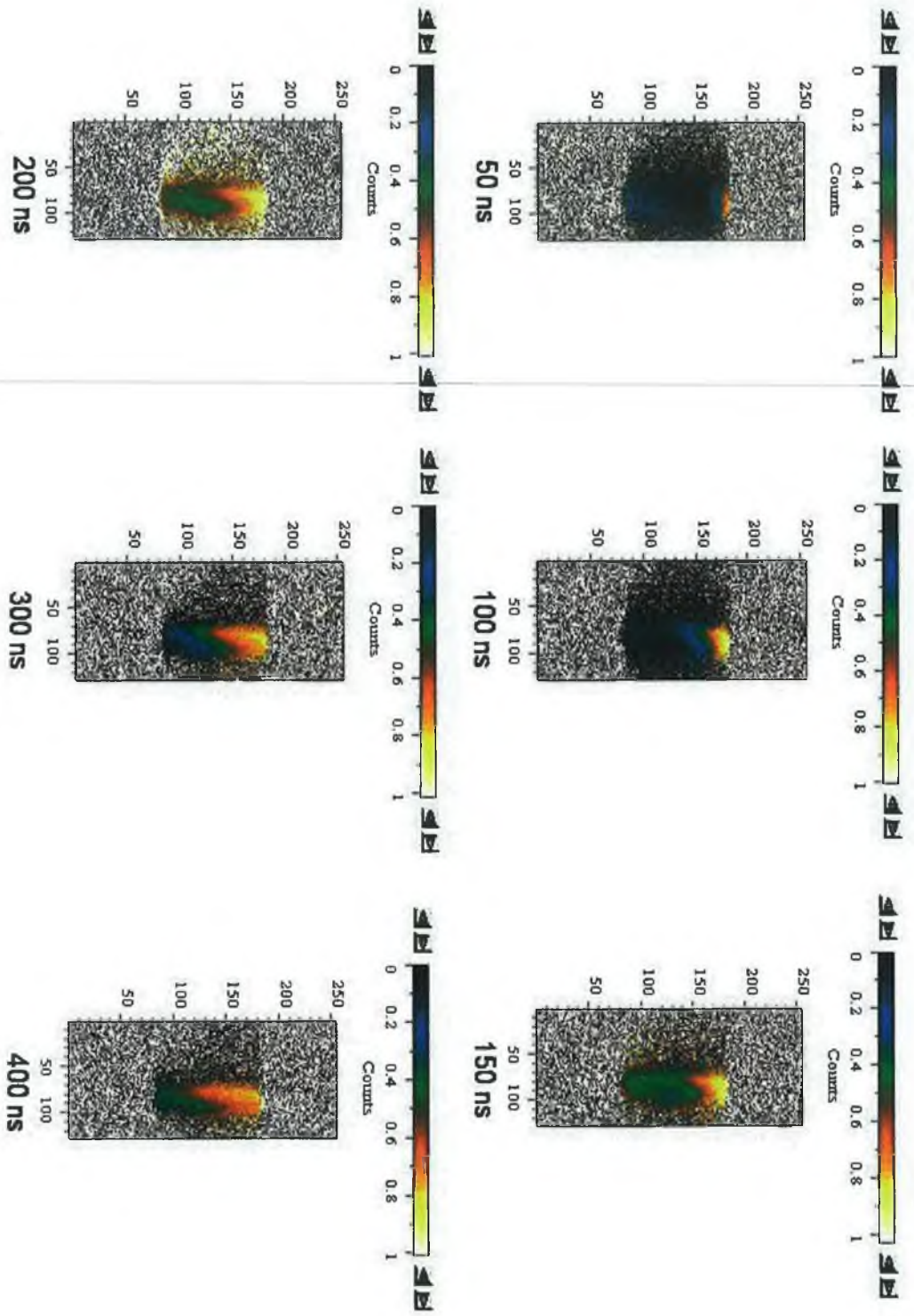

Figure 4.8. Time and space resolved maps of equivalent width in Angstrom of singly ionized calcium using the 3p-3d resonance at 37.34 nm

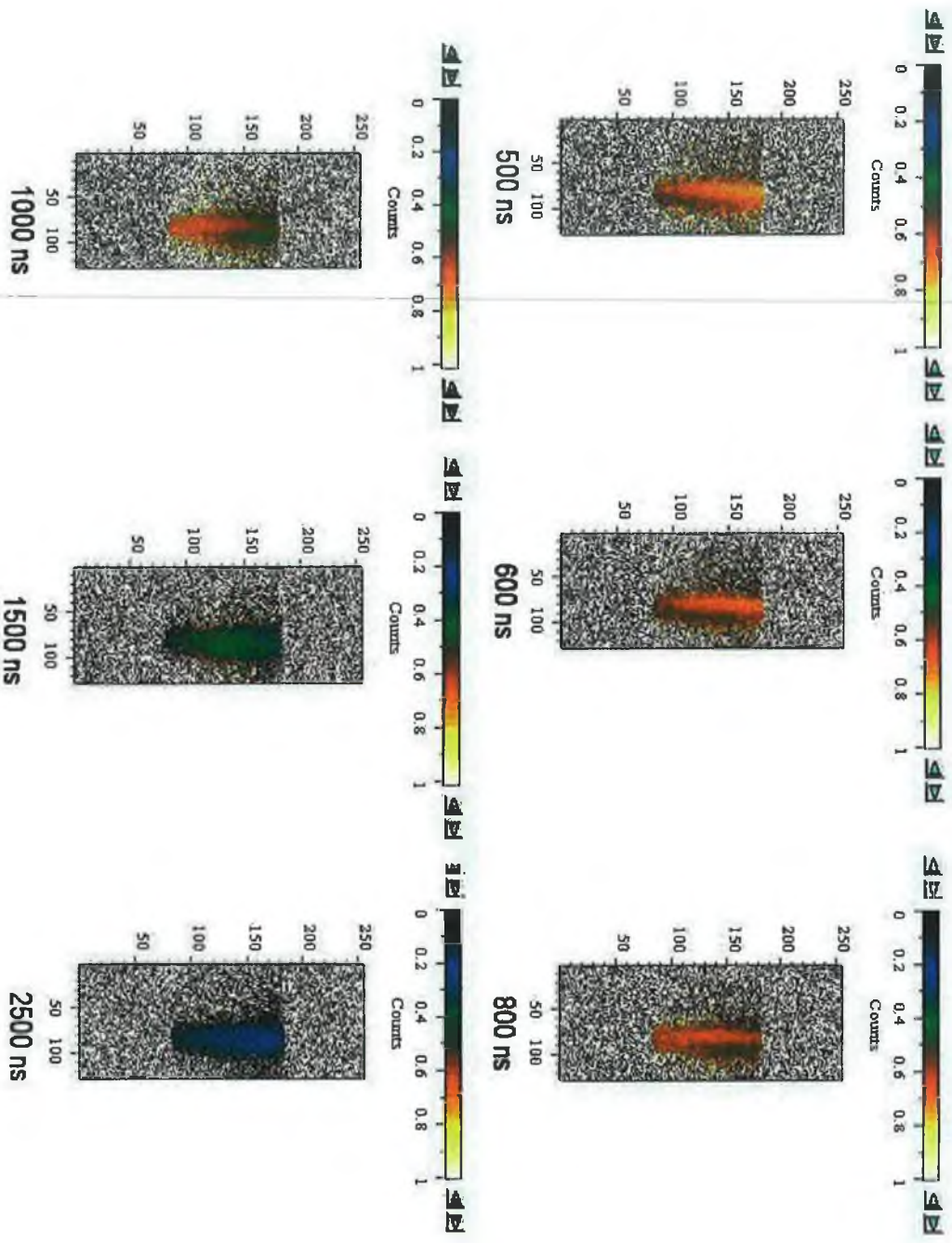

Figure 4.8 (cont) Time and space resolved maps of equivalent width in Angstrom of singly ionized calcium using the 3p-3d resonance at 37.34 nm

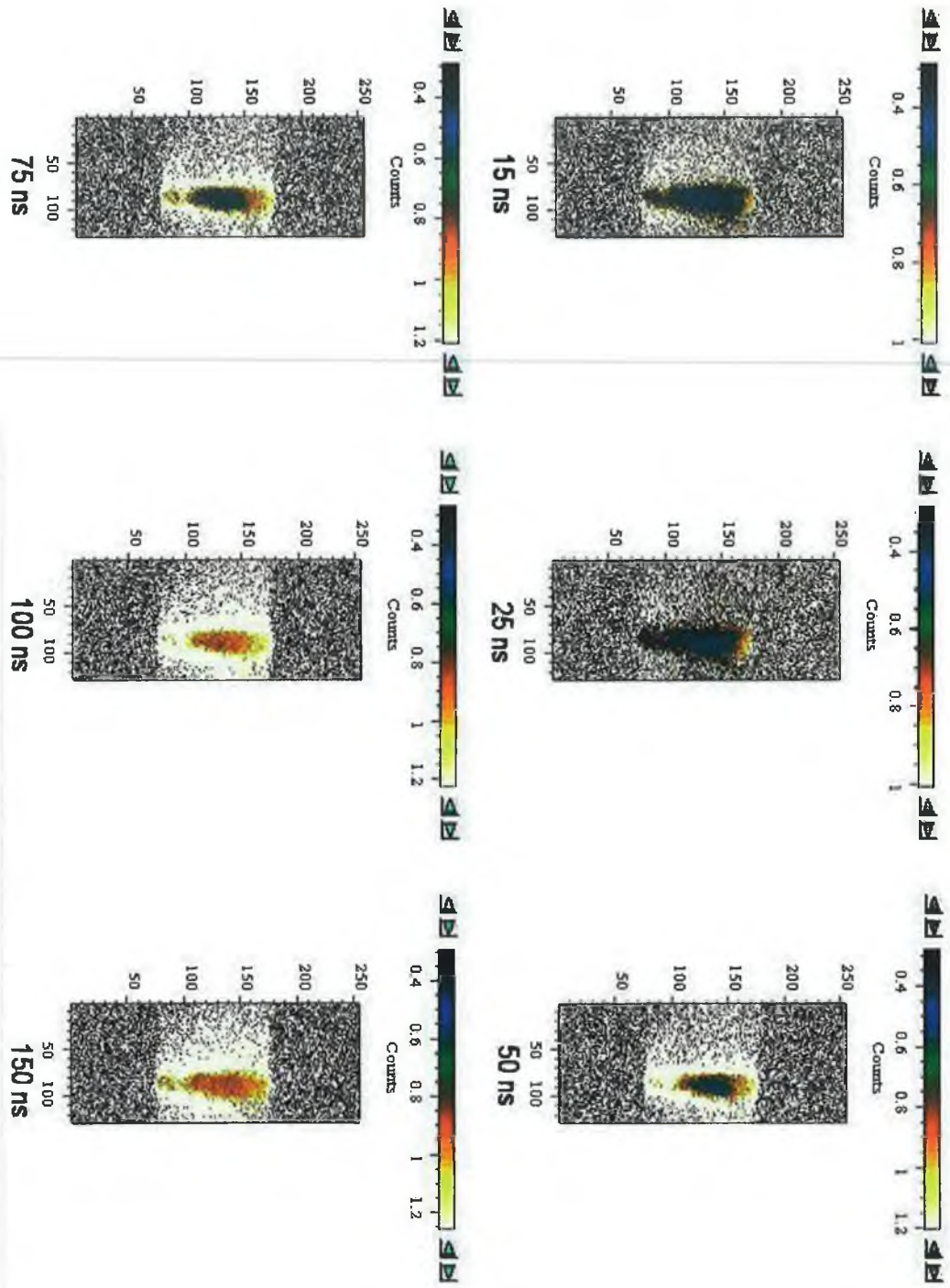

Figure 4.9. Time and space resolved maps of equivalent width in Angstrom of doubly ionised calcium using the 3p-3d resonance at 35.73 nm

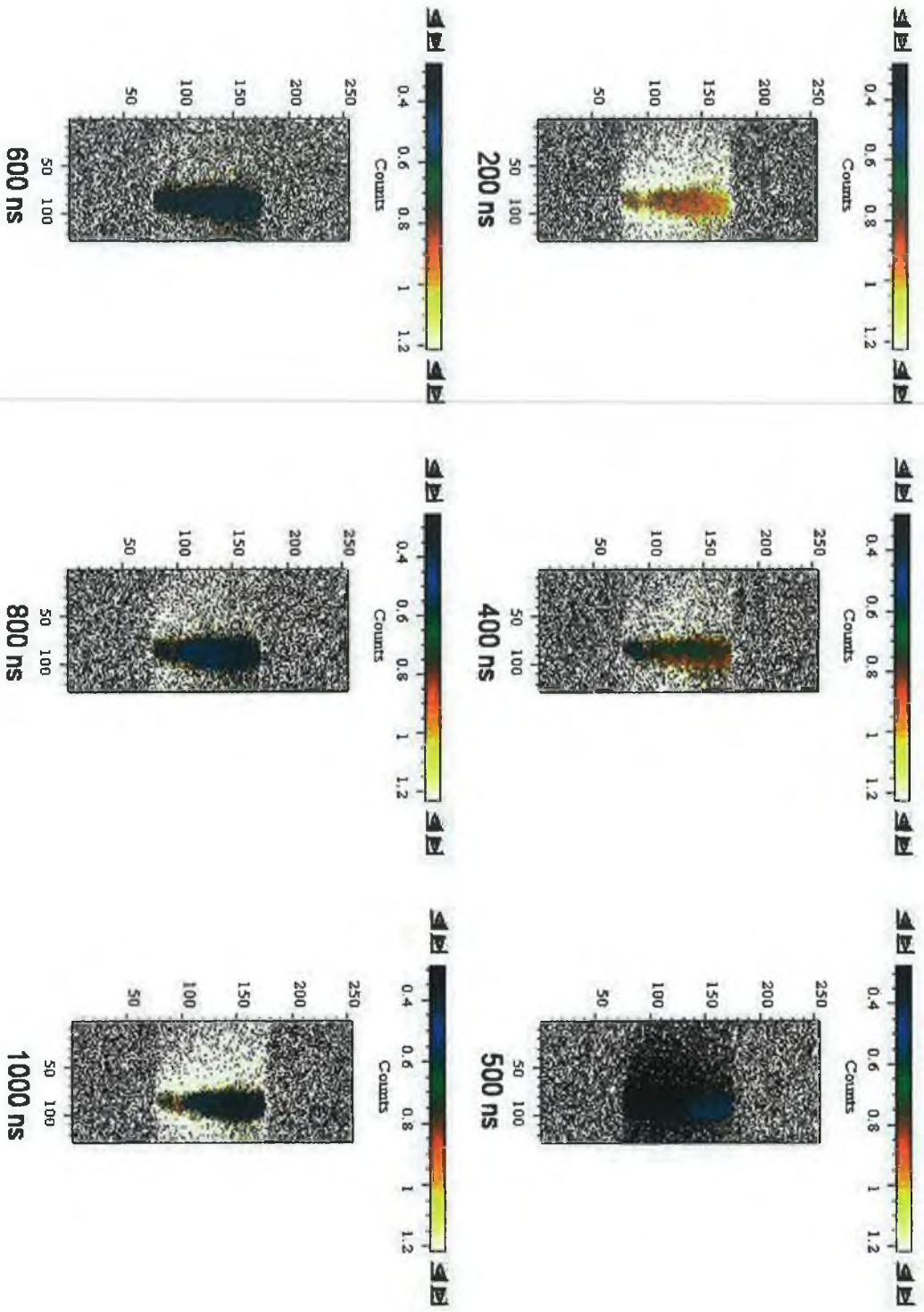

Figure 4.9 (cont) Time and space resolved maps of equivalent width in Angstrom of doubly ionised calcium using the 3p-3d resonance at 35.73 nm

Due to the poor spatial and spectral resolution of the RAL data we will not present any detailed analysis here. Instead, we now present the images recorded in the DCU laboratory in figures 4.10, 4.11, and 4.12. We show time and space resolved maps of equivalent width of the same calcium transitions, i.e., neutral calcium using the 3p-3d resonance line at 39.48 nm, Ca^{+} using the 3p-3d resonance at 37.34 nm and Ca^{2+} using the 3p-3d resonance at 35.73 nm with a parallel beam of cross section 4 mm × 4 mm.

The knife-edge arrangement described in chapter 3, protruded ~ 200 μm in front of the calcium target. Here the target surface is located on the right hand side of the image and the plasma is expanding from right to left. The pixels are binned 6 × 6 giving a single "superpixel" size of 78 μm. These images correspond to the accumulation of 5 series of 10 shots and the images were processed as explained in section 4.1.2.

The backlighting source was produced using a Nd-Yag laser (1064nm, 800 mJ, 10 ns) focused to a point of 100 μm diameter, resulting in an on target irradiance of ~ 1×10^{12} $W.cm^{-2}$. The sample plasma was produced using a Nd-YAG laser (1064 nm, 300 mJ, 20 ns) focused to a horizontal line of 3 mm length and 100 μm width, yielding a power density on target of 5×10^{9} $W.cm^{-2}$.

The entrance and exit slit were both set at 100 μm, giving a spatial resolution of 130 μm in the tangential plane and 180 μm in the sagittal plane. The resolving power varies from a value of 400 at 30 nm to 1000 at 100 nm. The typical pressure reached in the sample chamber using a combination of a rotary and turbomolecular pump was of the order of 10^{-5} mBar.

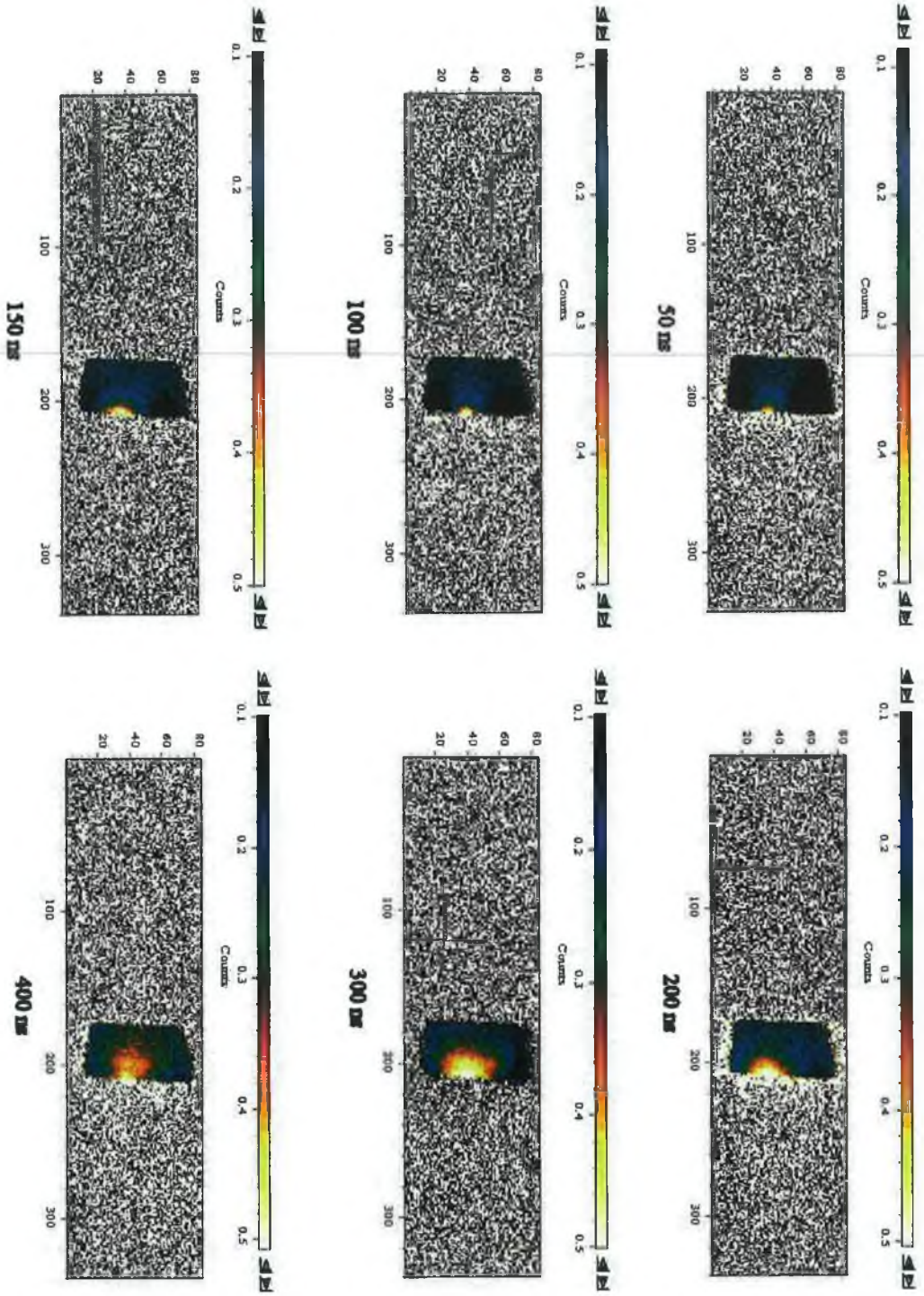

Figure 4.10. Time and space resolved maps of equivalent width in Angstrom of neutral calcium using the 3p-3d resonance at 39.48 nm

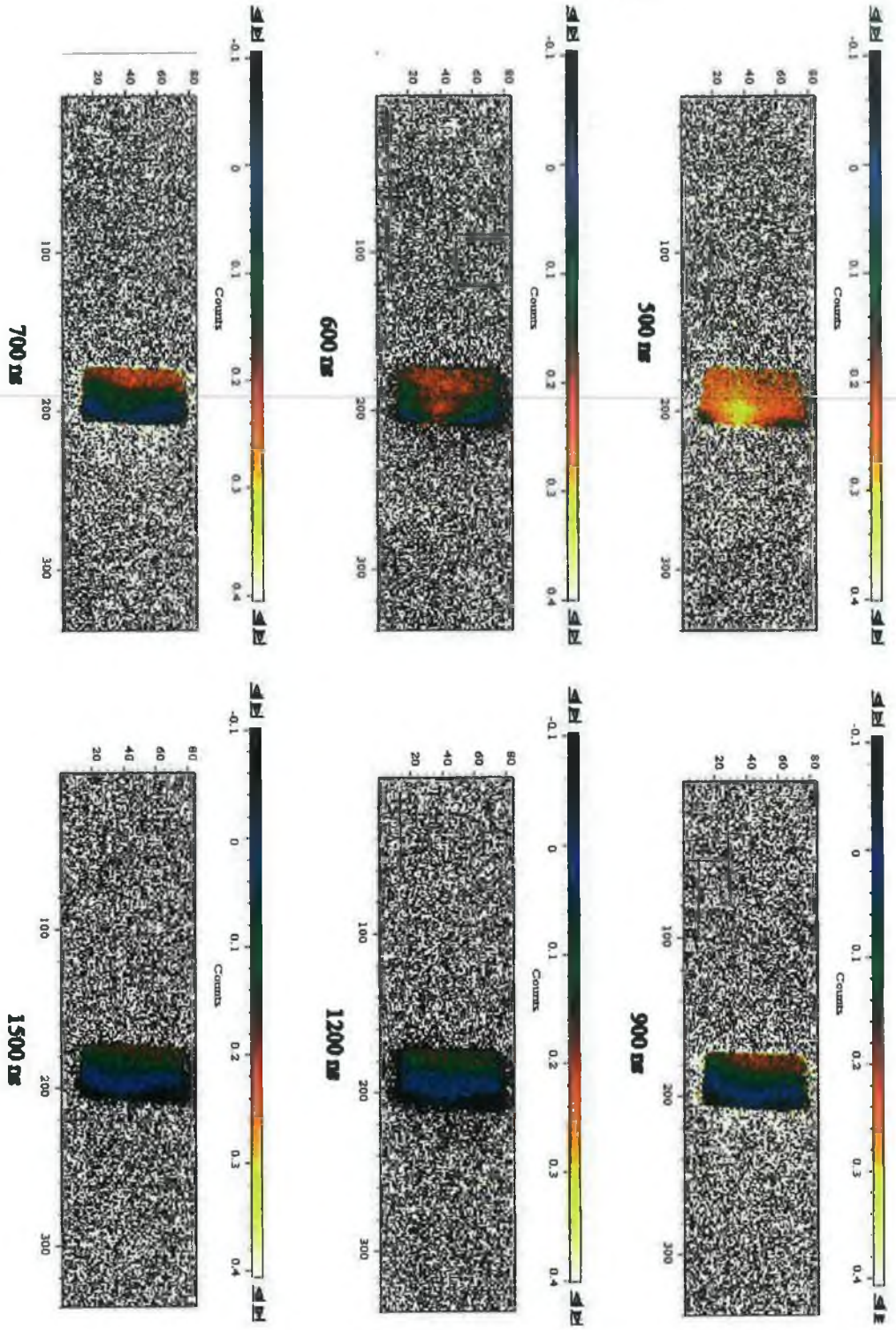

Figure 4.10 (cont) Time and space resolved maps of equivalent width in Angstrom of neutral calcium using the 3p-3d resonance at 39.48 nm

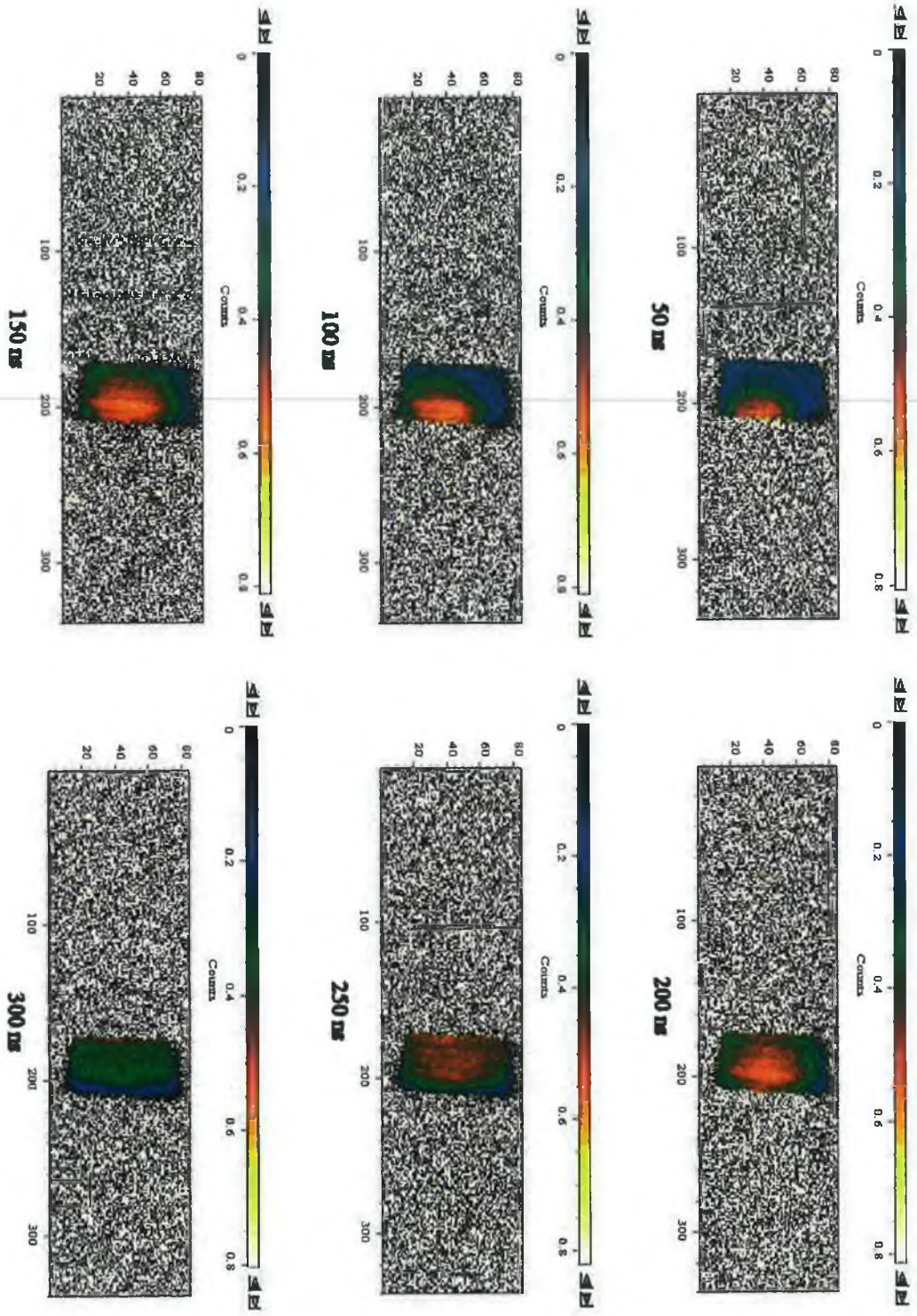

Figure 4.11. Time and space resolved maps of equivalent width in Angstrom of singly ionised calcium using the 3p-3d resonance at 37.34 nm

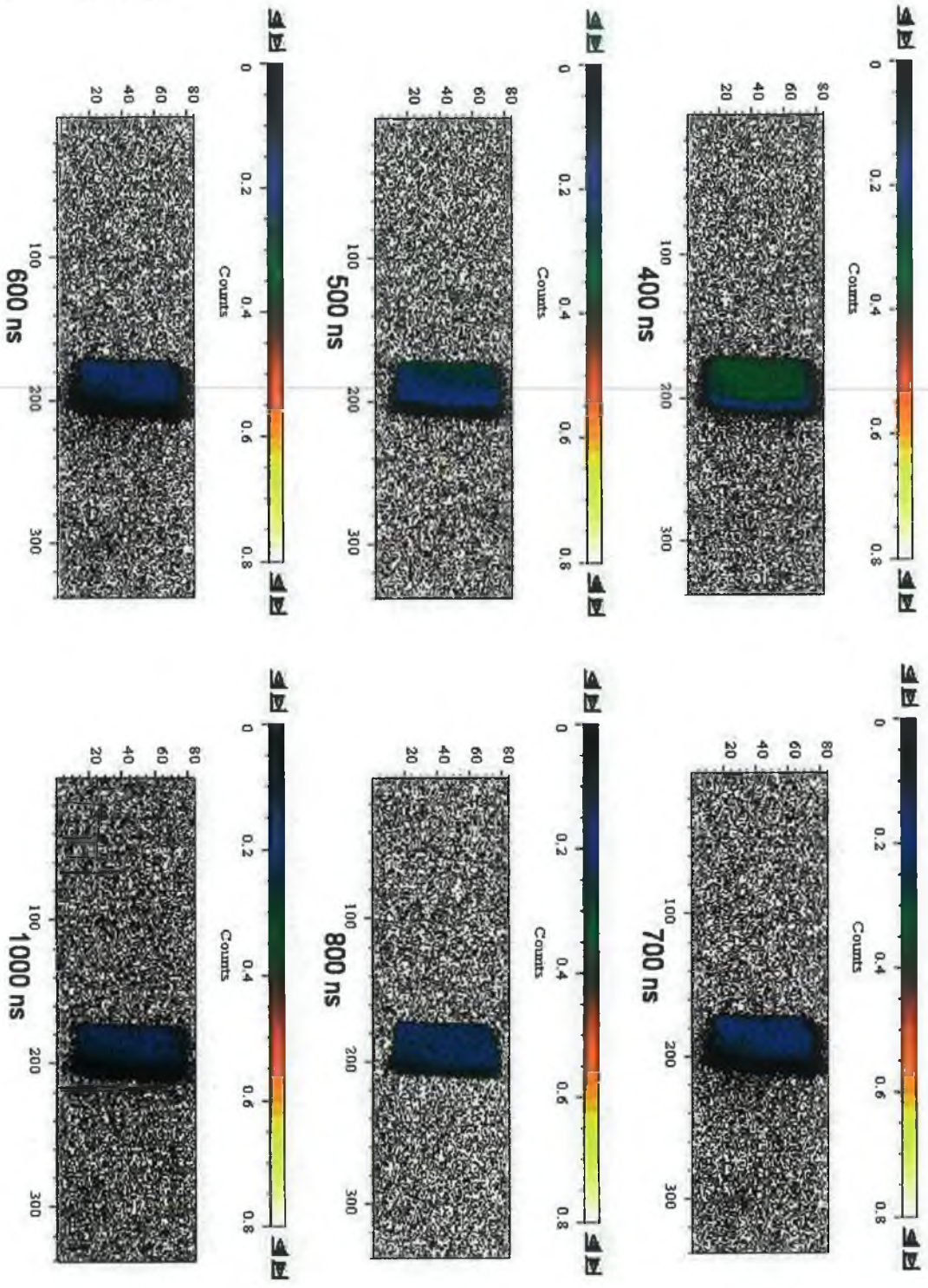

Figure 4.11 (cont) Time and space resolved maps of equivalent width in Angstrom of singly ionised calcium using the 3p-3d resonance at 37.34 nm

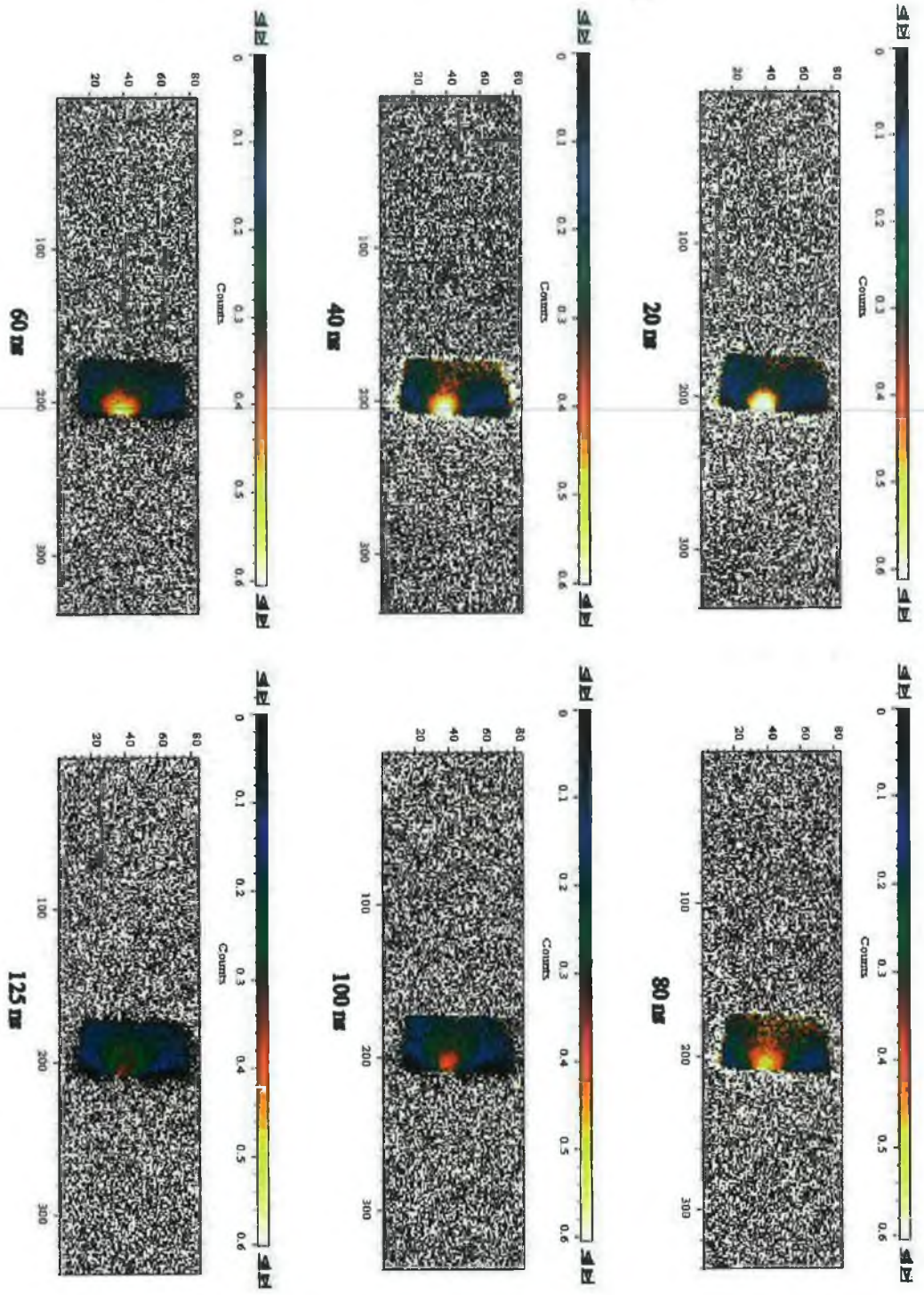

Figure 4.12. Time and space resolved maps of equivalent width in Angstrom of doubly ionised calcium using the 3p-3d resonance at 35.73 nm

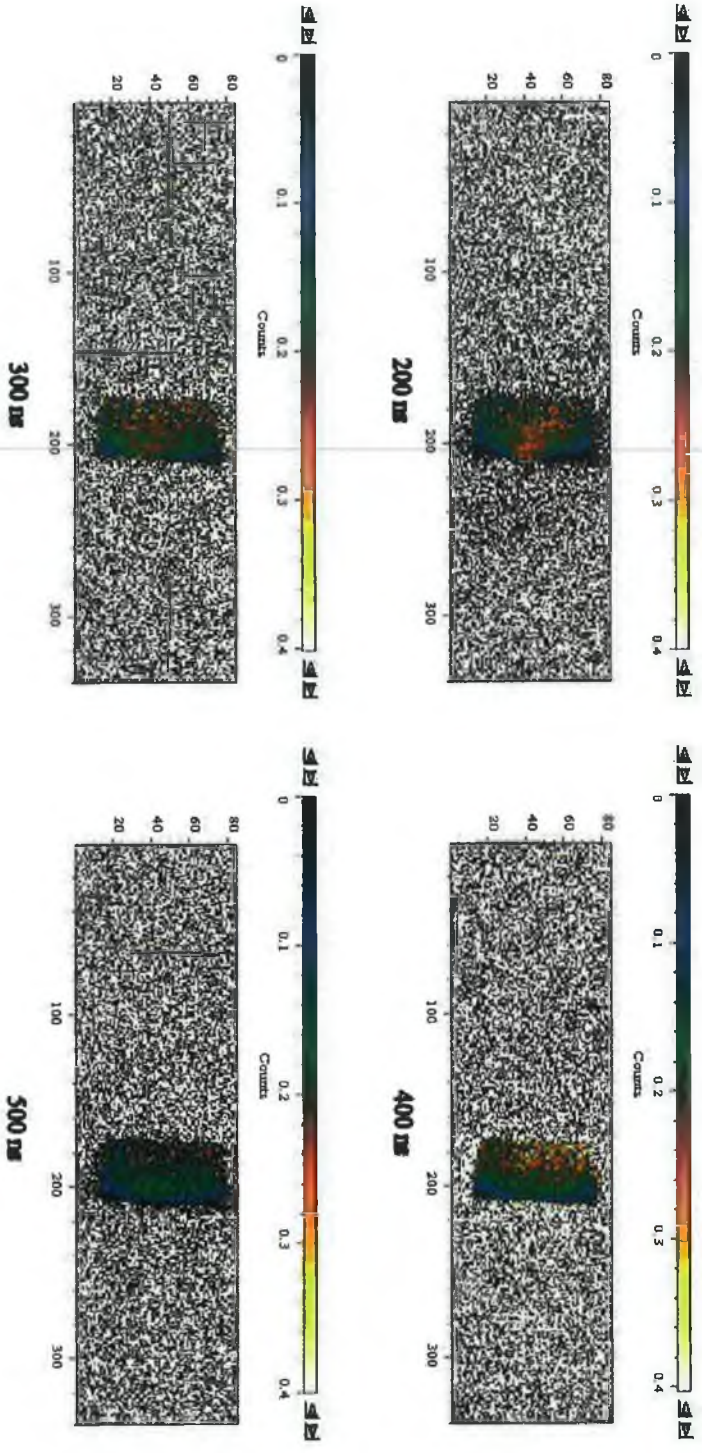

Figure 4.12 (cont) Time and space resolved maps of equivalent width in Angstrom of doubly ionised calcium using the 3p-3d resonance at 35.73 nm

In figures 4.7 to 4.12 we show a series of photoabsorption images of calcium plumes recorded at different time delays after the plasma breakdown. The VUV beam was tuned to the inner shell (3p – 3d) resonances of atomic Ca [figures 4.7, 4.10] and Ca^+ [figures 4.8, 4.11] and also the valence (3p – 3d) resonance Ca^{2+} [figures 4.9, 4.12] in order to separate out the different charges states. The VUV continuum duration is ~ 20 ns (Carroll *et al.* 1980) and represents the exposure time for each recording. The shadowgraphs embody information on the spatio-temporal evolution of ground state species in the plume, i.e., the dark material not seen in normal ICCD (emission) imaging. All pictures are photoexcitation in nature. However, since the 3p-3d resonances in the neutral and singly charged species are inner shell transitions, these images are effectively (resonant) photoionization images of these species. For the doubly charged ion, with an Ar-like electronic configuration of $3p^6$ ($^1S_0$), the image is a simple photoexcitation one, since the excited state can decay by fluorescence only.

When comparing the two sets of images, we notice a striking difference between the respective quality of the recorded shadowgrams due to a better signal to noise ratio, which the modifications added to the second system made possible, especially:

- A better optimisation of the knife-edge position and the laser parameters contributed to a significant reduction in the emission of the sample plasma detected on the CCD camera
- Improvement on the stability of the VUV source. Variation in the intensity of the VUV emission from the backlighting source would result in errors in the determination of the equivalent width (see comments about the RAL data)
- Better light collimation at the entrance slit of the monochromator resulted in a higher VUV flux recorded on the detector

Concerning the expansion of the plasma plume, we notice that in the set of images recorded during the experiment carried out at RAL, the plume seems to stay attached to the target surface. On the other hand, on the set of images recorded in DCU we see the plasma plume detaching from the target after ~ 600 ns after plasma breakdown for neutral calcium, 250 ns for Ca^+ ions, and ~150 ns for the Ca^{2+} ions. Although the full spatial extent of the plasma could not be viewed in both systems, the plume is visible on the set of images recorded in DCU. It appears certain that after a time delay specific to each ionisation stage (the highly charged ions expanding faster), the plume tends to a rugby ball shape before detaching

from the target. This behaviour has been observed in the visible region using direct ICCD measurement (Geohegan *et al.*, 1992, 1995, 1996, Whitty *et al.* 1998, Puretzky 1996). This difference can be explained by the different size of the respective probe beams ~ 3.7 mm (horizontal plane) x 2.6 mm (vertical plane) in the Rutherford Appleton Laboratory and 3 mm (horizontal plane) x 4 mm (vertical plane) in DCU. From the images recorded in DCU we see that the dimension of the plasma plume in the sagittal plane reaches ~ 4 mm after a short time delay. In the RAL set of images where the vertical dimension of the beam is only 2.6 mm, the change in the shape of the plume could not then be detected since at all time delays, the plasma plume covers the full vertical field of view of the probe beam. However, by looking closely at the images we notice that after a certain time delay, there again depending on the ionisation stage, that the values of equivalent width and hence density are smaller near the target than in the "centre" of the plume.

Comparing the range of equivalent width values recorded with the two systems, the values obtained at RAL appear to be higher than the values recorded in DCU. However the data acquisition procedure was not the same in each case and not at all adequate to make direct comparisons. When calculating the ratio $W_\lambda = \Delta\lambda \frac{I_0 - I}{I_0}$ the shadowgram of I_0 was recorded before any other absorption image and kept constant for about 10 series of 10 shots. The consistency of the backlighting source wasn't measured during the original pathfinder experiment due to the limited time available at RAL to perform the experiment. When we carried out this test in DCU, we discovered that after 50 shots the intensity of the backlighter starts to decrease using a Nd-YAG laser (1064 nm, 800 mJ , 10 ns). The backlighter in RAL was produced using a KrF laser (248 nm, 170 mJ, 20 ns) for which the ablation depth is larger than for a Nd-YAG laser (Momma *et al.* 1996, Gamaly *et al.* 1999). Hence, the plasma source was moving off the optical axis faster and the decrease in the recorded intensity was indeed quicker. It is difficult to assign a definite value to the error on the measurement but it is clear that the absolute value of the successive absorption images (I) was getting smaller independently of the absorption, and thus the values of the equivalent width were becoming higher. The data acquisition procedure has been improved for the experiments carried out in DCU, partly solving this problem. The effects due to this error reduction will be dealt with later in this chapter.

4.1.4. Maps of column density.

To determine maps of column density, a knowledge of the absolute cross section of the transition under study is essential. Here, this value is only known for the 3p – 3d resonance of Ca^+, at 37.43 nm and hence, we will only derive maps of column density NL = $\int$n(x)dx where n(x) is the ion density along the line of sight, for Ca^+ using the images obtained with the second experimental set-up.

As explained in chapter 1, we use the general expression of the equivalent width, written as a function of wavelength λ:

$$W_\lambda = \int_{\Delta\lambda}\left(1-\exp\left(-n_i L \int_{\Delta\lambda}\sigma_\lambda d\lambda\right)\right)d\lambda \qquad [4.3]$$

where σ(λ) is the total absolute photoionization cross section and the integral is taken over the 37.34 nm , 3p – 3d resonance profile.

To convert the maps of equivalent width obtained experimentally into maps of column density we solve graphically the above equation. The absolute cross section profile in the vicinity of the 3p – 3d resonance is known (Lyon *et al.* 1987) and by multiplying it by different values of NL we can compute a table of values of W_λ. We construct in this way a table of values of W_λ as a function of the column density (NL). We then plot NL vs. W_λ and by fitting a high order polynomial to the curve we can convert measured W_λ image (pixel) values directly into column density values. In figure 4.13, we plot the column density NL as a function of the equivalent width, the red curve being the best polynomial fit.

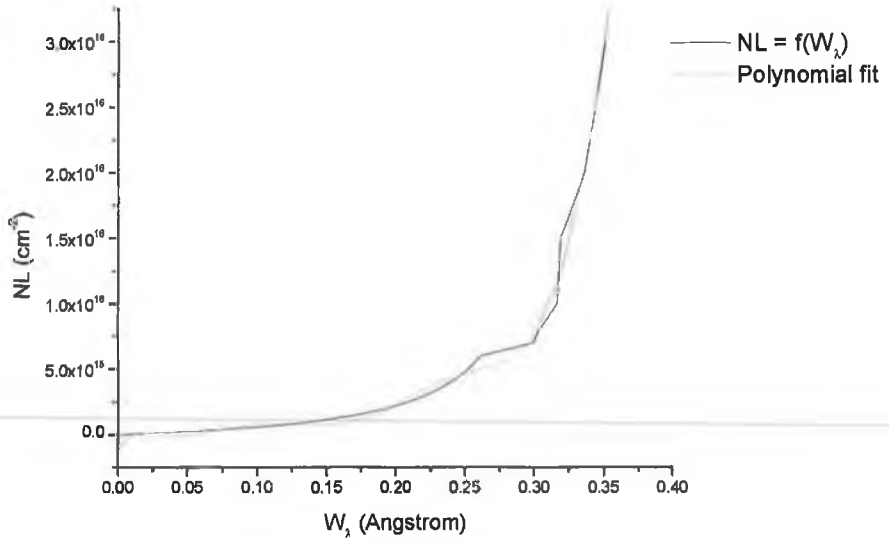

Figure 4.13. Plot of the column density NL as a function of the equivalent width

The red curve is the best fit, here a polynomial of the eighth order, which reads:

$y = -4.69\ 10^{14} + 1.16\ 10^{17}x - 7.06\ 10^{18}x^2 + 1.71\ 10^{20}x^3 - 2.03\ 10^{21}x^4 + 1.28\ 10^{22}x^5 - 4.43\ 10^{22}x^6 + 7.86\ 10^{22}x^7 - 5.58\ 10^{22}x^8$

We can convert maps of equivalent width to maps of column density NL by applying this polynomial formula to each image. The software package MATLAB was used to perform this operation since it permits an easy handling of matrices. From figure 4.13 we notice that the behaviour of the column density NL as a function of the equivalent width tends to an asymptotic value of 0.35 Σ. This is explained by noting that the 3p – 3d Ca^+ resonance is very strong (with a peak cross section of 2200 Mb), and hence when calculating the values of W_λ, saturation is reached for NL values larger than 2 x 10^{15} cm^{-2}. This becomes even more clear when plotting $1 - \exp(-\sigma NL)$ for different NL values as shown in figure 4.14.

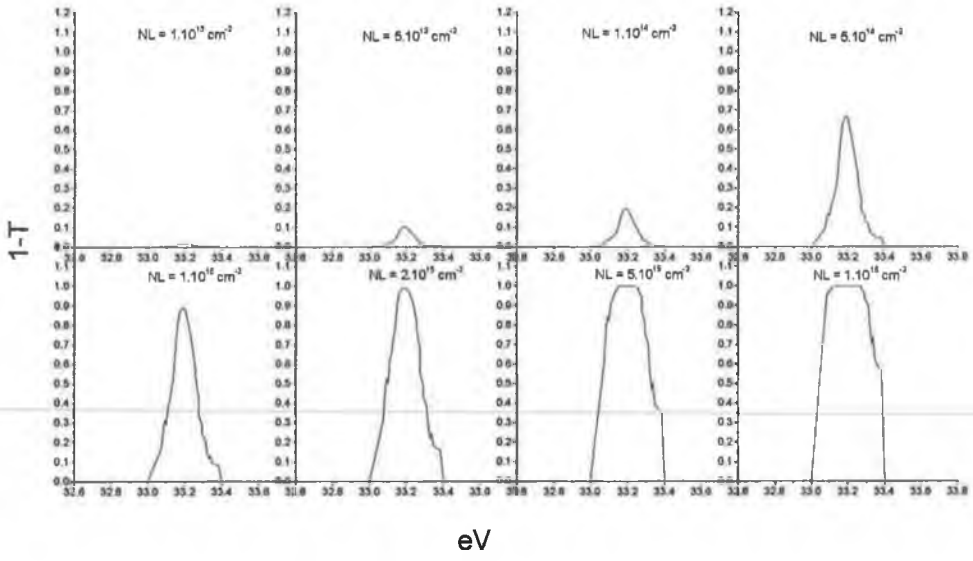

Figure 4.14. Plot of 1 – exp(-σNL) for the Ca^+ (3p – 3d) resonance line for different values of column density using the experimental absolute cross section measured by Lyon *et al.* (1987)

From figure 4.11 we notice that the values of equivalent width are larger than 0.35 Σ from the plasma breakdown until 500 ns of expansion where the main bulk of the plasma seems to be located outside our window of observation. These values correspond to a saturated signal and hence it is hard to interpret them. Nevertheless we could still extract maps of column density, which for values of $W_\lambda > 0.35\ \Sigma$ will give a number that cannot be interpreted, but for the lower values we would actually get a lower limit on the plasma column density.

The effect of saturation is clearly illustrated by derived column density maps for short time delays (figure 4.15).

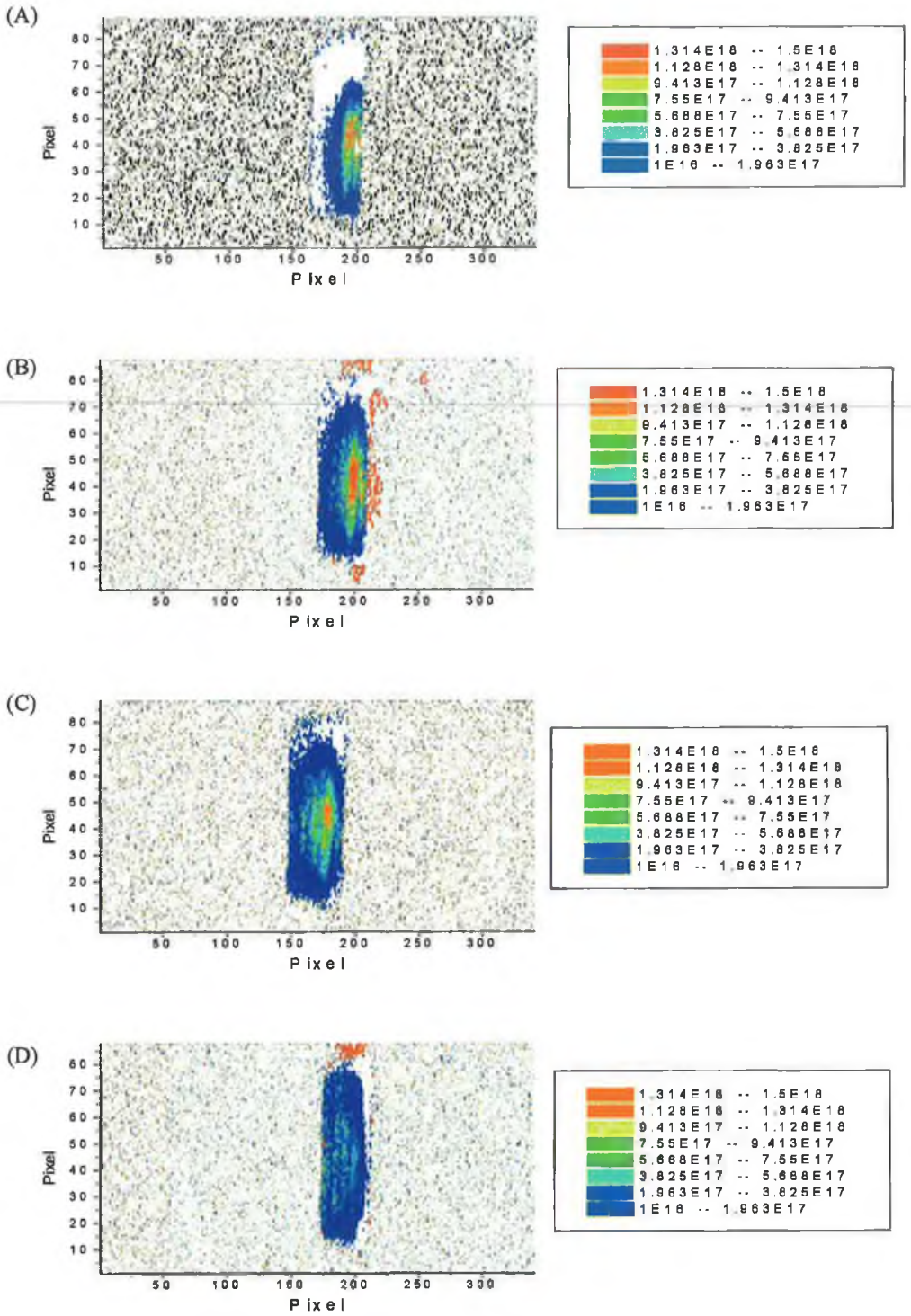

Figure 4.15 Maps of Ca^+ column density for a time delay of (A) 100 ns, (B) 150 ns, (C) 200 ns and (D) 250 ns

The values of column density shown in figure 4.15 are well above the saturation limit. Moreover, it is hard to derive an accurate error margin on the derivation of column density maps for calcium since we are dealing with a saturated signal. The saturation of the signal gives rise to a change in the slope of the function describing the variation of the column density NL with the equivalent width. As a consequence, the linear fit does not increase monotonically, and the "oscillations" in the polynomial give in some cases higher density values for lower values of equivalent width. Shown in figure 4.16 is a column density map for a delay of 600 ns. Although not saturated at this time delay, the main plume has detached from the target and has almost left the field of view. Hence, it is of limited physical value in studying plume-ion expansion and column densities. To overcome these problems we decided to switch to column density maps of Ba^+ ions, where a more accurate polynomial fit can be obtained.

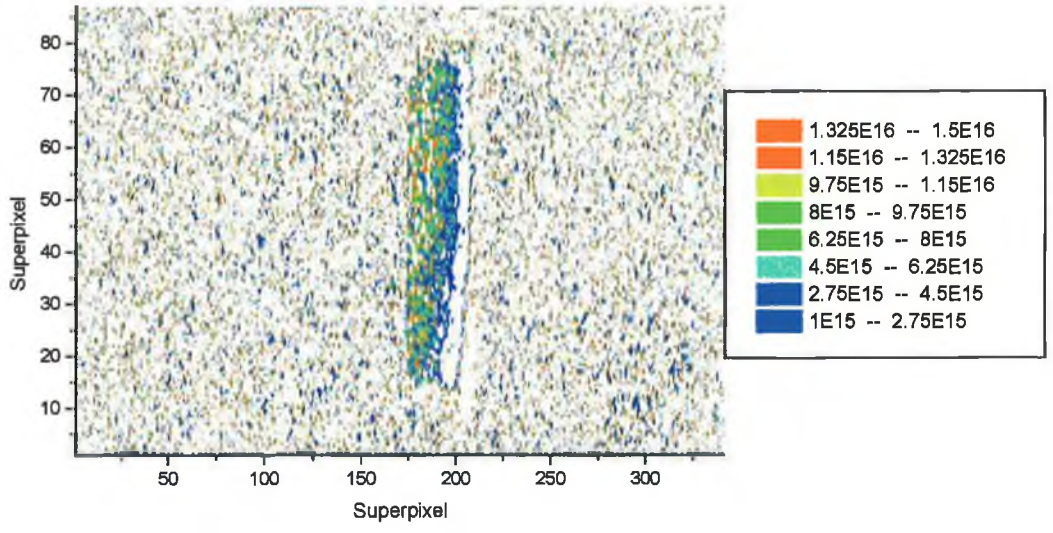

Figure 4.16. Map of Ca^+ column density for a time delay of 500 ns

4.2 Barium studies

4.2.1 Introduction: Photoionisation of barium and barium ions

The calcium study revealed several problems related to the accurate determination of maps of column density. The saturation of the signal, due to the large value of the Ca^+ 3p - 3d cross section exposed the difficulty in obtaining an accurate fit and thus led to considerable errors in the measurements. Barium and its ions have been studied in photoionisation throughout the VUV and extreme-UV spectral range (Holland *et al.* 1981, Lyon *et al.* 1984, Kent *et al.* 1987) and hence, much supporting data are readily available. In particular we have chosen to study the Ba^+ transition at 46.68 nm. Firstly because the absolute cross section of Ba^+ has been measured by Lyon *et al.* (1986) between 42 nm and 77.5 nm, a wavelength range for which the photoabsorption system is optimised. Secondly, this resonance in the Ba^+ spectrum is well isolated from other transitions involving neutral barium and other more highly charged barium ions likely to be present in the plume. Finally, the study of the single element barium is a useful exercise in advance of studies on the high T_c superconducting material YBCO planned at a future date for this system.

Rose *et al.* (1980) performed relativistic Dirac Hartree Fock calculations on the 5p spectrum of neutral barium following the experimental work of Connerade *et al.* (1979) and Mehlhorn *et al.* (1977). Using the Melhorn *et al.* analysis, they were able to determine $5p^6 6s^2$ ($^2P_{1/2,3/2}$) limits and group most of the observed transitions in a number of Rydberg series. The neutral barium spectrum recorded by Connerade *et al.* (1979), with the assigned series and ionisation limits is shown in figure 4.17. The Ba^+ transition under study here lies at 46.68 nm, so that we are confident of the absence of neutral atom absorption in this wavelength range except of course for the weak direct photoionisation continuum component.

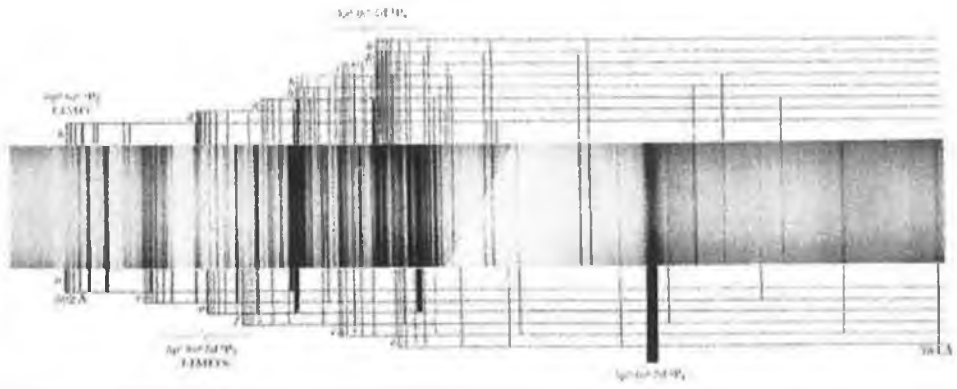

Figure 4.17.The 5p subshell spectrum of neutral barium (after Connerade 1979)

WT Hill *et al.* (1982), used photoabsorption spectroscopy to study the 5p – nl transitions in the spectrum of doubly charged barium ions. Using a multichannel quantum defect theory approach they were able to assign Ba^{2+} transitions between ~ 32 and 42 nm. Ba^{2+} transitions occurring at longer wavelength, which have not been recorded in this experiment, can be found on the National Institute of Standard and Technology (NIST) database and are presented in table 4.1.

Wavelength (nm)	Relative intensity
40.38	5
40.71	2
42.01	7
42.38	4
44.89	9
45.70	8
55.55	14
58.76	14
64.73	18
65.34	9

Table 4.1. Ba^{2+} transitions in the VUV from the NIST database (http://physics.nist.gov/cgi-bin/AtData/main_asd)

From the table 4.1, the closest Ba^{2+} transition is found at a wavelength of ~ 45.70 nm, compared with the Ba^{+} transition under study found at 46.68 nm. Knowing that the radiation bandwidth is 0.1 nm, we can easily isolate the Ba^{+} transition at 46.68 nm from the nearest Ba^{2+} transitions. Hence we are only measuring a Ba^{+} transition, and the column densities measured are free from neutral barium or doubly ionised barium contamination.

The Ba^{+} spectrum is complicated by a multitude of intermediate autoionising levels (Kent *et al.*, 1987) and most of the transitions although accurately measured have not yet been assigned. The transition under study was chosen because the absolute cross section is known and we showed that it was isolated from transitions involving different ionisation stages. For completeness we will now attempt to assign this transition.

From Lucatorto *et al.* (1980), we know that the Ba^{2+}: $5p^6$ $(^1S_0) \rightarrow 5p^5$ 5d [1/2,3/2] transition is located at 55.60 nm and from Hill *et al.* (1987) we known the Ba^{2+}: $5p^6$ $(^1S_0) \rightarrow 5p^5$ 6d [1/2,3/2] is located at 42.00 nm, which constitutes a wavelength difference of 13.6 nm. Looking at the Ba^{+} transitions, from Hansen *et al.* (1974, 1975) we know that the $5p^5 5d$ (^1P) 6s $^2P_{1/2,3/2}$ is located at 57.83 nm and assuming that 6s electron is a "spectator", we should find the Ba^{+} $5p^5 6d$ (^1P) 6s $^2P_{1/2,3/2}$ at an energy close to 44.35 nm. If we allow for a reduction in the energy shift due to the screening effect of the addition of the 6s electron in Ba^{+} over Ba^{2+}, we notice in the spectrum recorded by Lyon *et al.* (1986) a similar feature at 46.61 nm, spread over the same energy range. Hence it seems reasonable to propose that the transition under study is the following:

$$Ba^{+}\ 5p^6\ 6s\ ^2S \rightarrow Ba^{+*}\ 5p^5\mathbf{6d}\ (^1P)\ 6s\ (^2P_{1/2,3/2}) \rightarrow Ba^{2+}\ 5p^6\ ^2S + e^{-}$$

The photoionisation cross section was measured by Lyon *et al.* (1986) using the same experimental set-up as used for the measurement of the Ca^{+} absolute photoionisation cross section. The profile, shown in figure 4.18 was used in this work to derive maps of Ba^{+} column density in an expanding plasma plume.

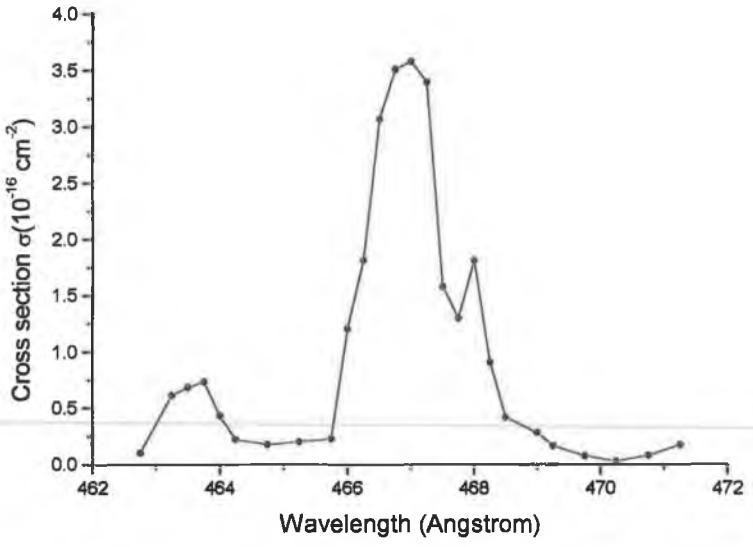

Figure 4.18. Absolute cross section the Ba^+ 5p - 6d resonance at 46.68 nm.(data supplied by John West 2002)

4.2.2 Time resolved maps of equivalent width for the 5p – 6d transition of Ba^+

The studies on the Ba^+ 5p - 6d resonance were performed using the system implemented in DCU only. We recorded maps of column density using the Ba^+ 5p - 6d resonance at 46.68 nm from time delays starting at 50 ns after the plasma breakdown. This delay corresponds to the time interval after which the absorption signal can be recorded, since for this experiment, the knife-edge protruded ~ 400 μm in front of the barium target. The plume front was then occluded by it for the first 50 ns or so. The conditions otherwise were the same as for the calcium study. Briefly, the target surface was located on the right hand side of the image and the plasma is expanding from right to left. The pixel were binned 6 × 6 giving a single "superpixel" size of 78 μm. These images were recorded after 5 series of 10 shots as in the (DCU) calcium study, and the images were processed as explained in section 4.2.1.

The backlighting source was produced using a Nd-Yag laser (1064nm, 800 mJ, 8 ns) focused to a point of 100 μm diameter, resulting in a power density on target of 1×10^{12} $W.cm^{-2}$. The sample plasma was produced using a Nd-YAG laser (1064 nm, 300 mJ, 20 ns) focused to a horizontal line of 3 mm length and 100 μm width, resulting in a power density on target of 5×10^9 $W.cm^{-2}$. The entrance and exit slits were both set at 100 μm, giving a

spatial resolution of 130 μm in the tangential plane and 180 μm in the sagittal plane. The resolving power varied from a value of 400 at 30 nm to 1000 at 100 nm. The results are shown in figure 4.19.

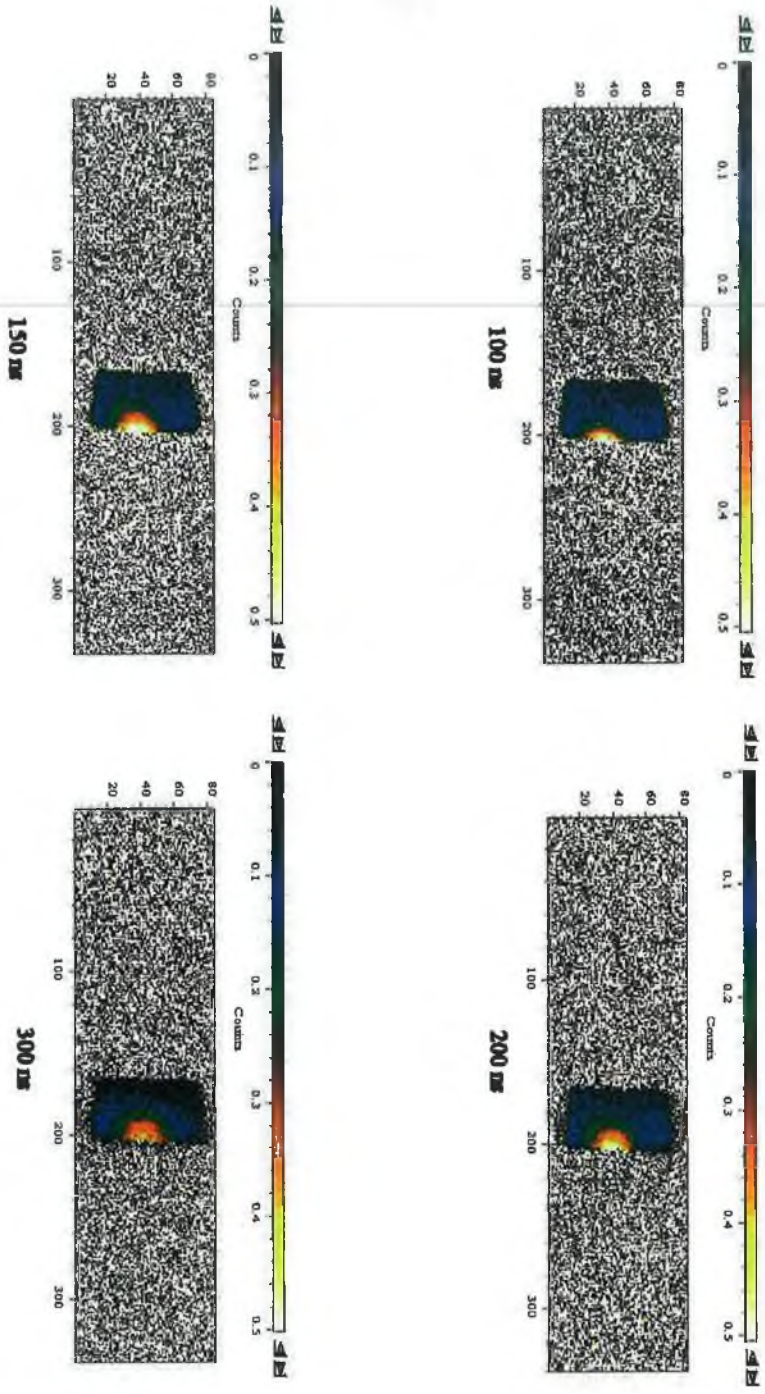

Figure 4.19. Time and space resolved maps of equivalent width of singly ionised barium using the 5p-6d resonance at 46.68 nm

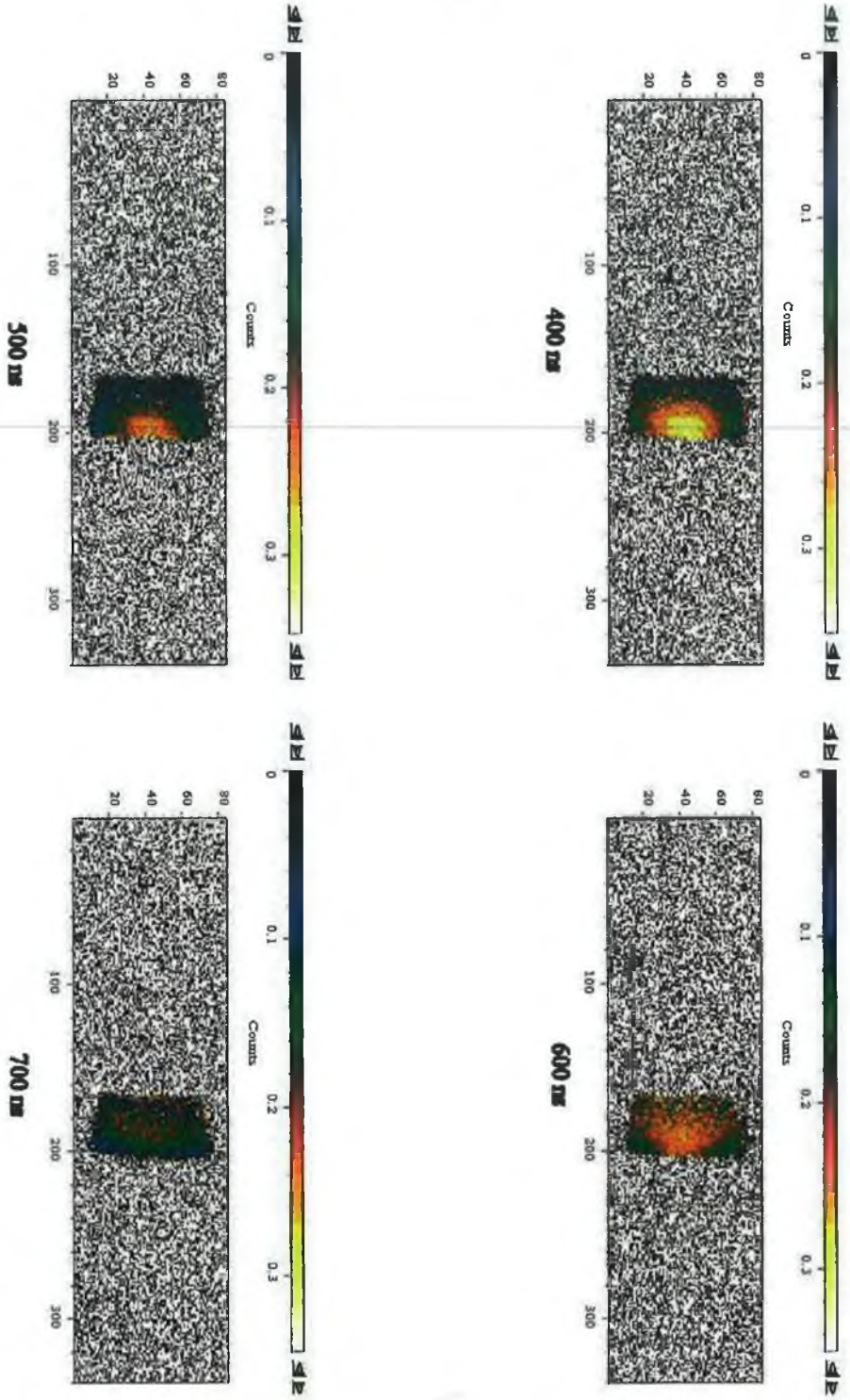

Figure 4.19 (cont) Time and space resolved maps of equivalent width of singly ionised barium using the 5p-6d resonance at 46.68 nm

The same characteristics recorded for the expansion of a calcium plasma are found for a barium plasma. The expansion velocity is slower, since it has a higher atomic mass than calcium but the shape of the plasma plume tends towards an elliptical shape before detaching from the target surface. Although the dimensions are comparable, the values of equivalent width are smaller in this case as expected. For the derivation of column density maps, we do not reach saturation for the values of equivalent width recorded here and hence, it is possible to derive maps of column density as explained previously.

4.2.3 Maps of equivalent width

We follow the procedure explained in 4.2 to derive maps of column density using the time and space resolved maps of equivalent width. In figure 4.20 we show a plot of NL as a function of equivalent width values.

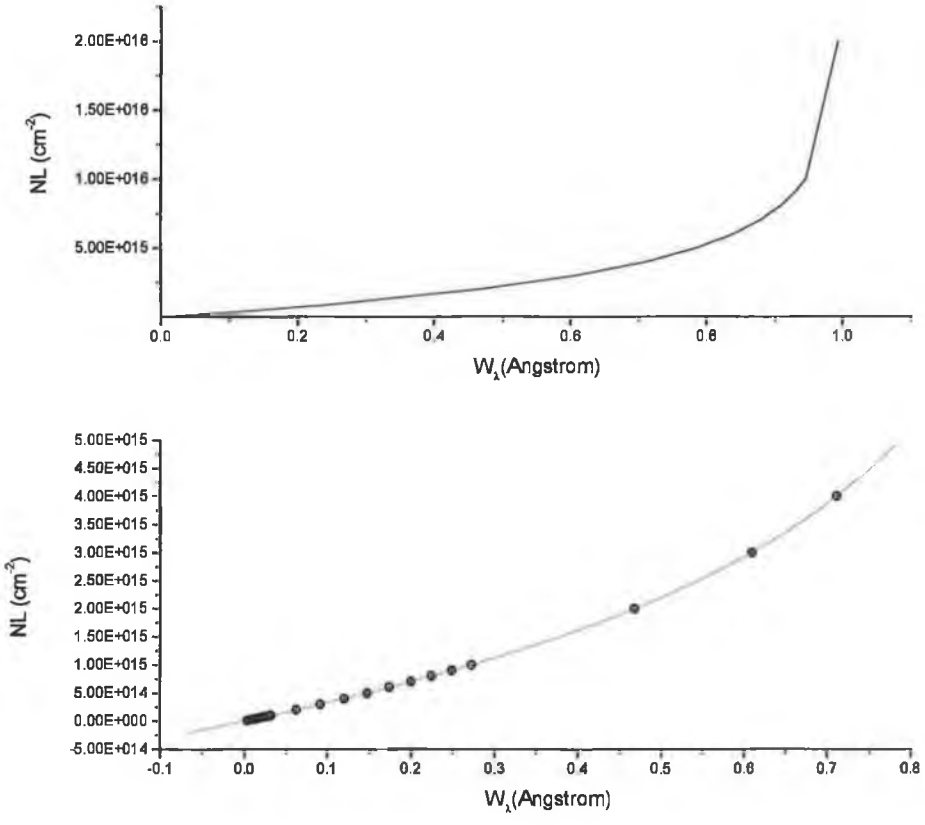

Figure 4.20. Plot of the column density NL as a function of the equivalent width (W_λ), top for $0 < W_\lambda < 1$ Å, and bottom $0 < W_\lambda < 0.7$ Å

The largest value of equivalent width extracted from the time and space resolved study is smaller than 0.7 Å, so that we only plot the column density NL as a function of the equivalent width for $0 < W_\lambda < 0.7$ Å. This way we obtained a much more accurate fit and here a polynomial of the 5th order gave us an excellent fit to the data, and the coefficient are summarised in table 4.2.

Polynomial order	Coefficient
x^0	$-5.24236\ 10^{11}$
x^1	$3.16893\ 10^{15}$
x^2	$8.89873\ 10^{14}$
x^3	$5.33356\ 10^{15}$
x^4	$-9.07590\ 10^{15}$
x^5	$9.32969\ 10^{15}$

Table 4.2. Polynomial fit coefficients to convert Ba^+ maps of equivalent into maps of column density (NL)

This polynomial was applied to the images of equivalent width for delays ranging from 100 ns to 500 ns, the results are shown in figure 4.21.

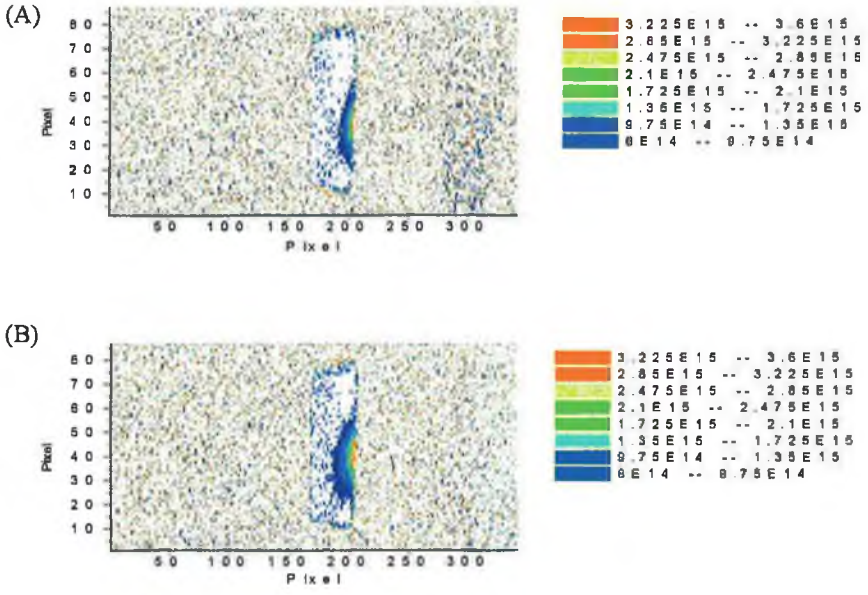

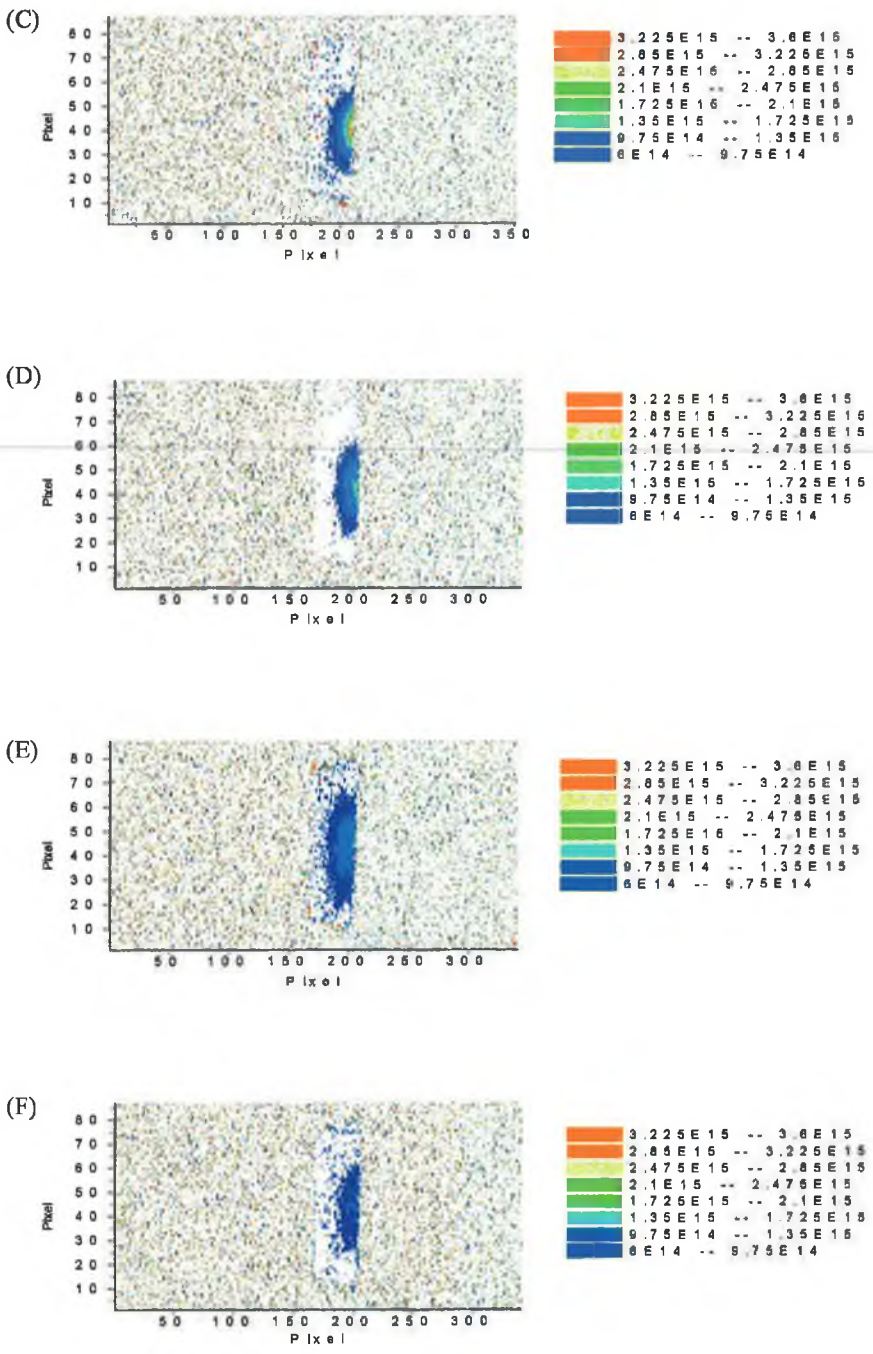

Figure 4.21. Ba^{+} maps of column density for (A) 100 ns, (B) 150 ns, (C) 200 ns, (D) 300 ns, (E) 400 ns and (F) 500 ns time delay after barium plasma breakdown

In figure 4.20, the maps (A), (B), (C) have the same scale which is on the left hand side at the bottom of the graph and the maps (D), (E), (F) are plotted on the same scale, which lies on the right hand side at the bottom of the graph.

The maps of column density show values from 3 x 10^{15} cm^{-2} close to the target surface at short time delays to values of the order of 1 x 10^{15} cm^{-2} at longer time delays. Contrary to the maps of equivalent width the detachment of the densest part of the plasma is not as obvious. Two different factors can explain this difference. First the colour scale has to be the same on each of the series of maps for an accurate comparison, and for low values of column density on a large colour scale details are lost. The main factor though is the relatively low values of equivalent width at long time delays , i.e., at $\Delta t \geq 500$ ns. When converting them to values of column density these values are in the same range as the error on the transformation and hence the maps are not as accurate as for short time delays. Nevertheless we observe on map (E) the detachment of the densest part of the plasma as here the values are still above the limit set by the error when converting maps of equivalent width to maps of column density.

The errors introduced during the determination of the column density can be extracted directly from the maps of equivalent width. Assuming that there is no absorption in some region of the 3 mm x 4mm area defined by the VUV beam, which happens at short time delays. Such regions should show values of equivalent width equal to zero, , i.e.,

$$W_\lambda = \frac{I_0 - I}{I_0} = 0 .$$

However the images show values close to 0.1 Å in regions where no absorption occurs, giving a value of $\frac{\Delta I_0}{I_0} = \frac{\Delta W_\lambda}{W_\lambda} = 0.1$ corresponding to the fractional error on the measurement. From Barford (1985) the error on the column density NL is then:

$$\Delta(f(W_\lambda)) = \Delta(NL) = f'(W_{\lambda_{mean}})\Delta(W_\lambda)$$

$$\Delta(NL) = \left(3.16 \times 10^{15} + 2\,(8.90 \times 10^{13}) W_{\lambda_{mean}} + 3\,(5.33 \times 10^{14})\, W^2_{\lambda_{mean}} - 4\,(9.07 \times 10^{15})\, W^3_{\lambda_{mean}} + 5\,(9.32 \times 10^{15})\, W^4_{\lambda_{mean}}\right) \times \Delta W_\lambda$$

We calculated the mean value of the equivalent width using the maps of equivalent width recorded experimentally for time delays of 100 ns, 150 ns, 200 ns, 300 ns, 400 ns and 500 ns. From the images, the area defined by the VUV beam was isolated and the sum of all the

equivalent width values per superpixel was calculated. This value was then divided by the number of pixels corresponding to the defined beam area to obtain a mean value of the equivalent width for each time delay. The average of this value over time , i.e., $W_{\lambda mean}$ = 0.16 Å was used to determine the error on the column density NL. By substituting it in the above expression we have an estimate of the error on the column density measurement of $\Delta NL = 3.10^{14} cm^{-2}$.

4.3 Plasma dynamics

The plasma expansion model derived by Singh and Narayan (1990) and described in chapter 1, gives us information about the evolution of the plasma dimensions with time as well as information on the plasma temperature and density.

As far as density measurements are concerned, the code calculates the overall plasma density and is not able to compute relative number densities corresponding to the different ions present within the plasma plume. As we are able to derive column density values only for atoms in a defined ion stage, it was not possible to compare directly the experimental and theoretical results obtained with the code.

On the other hand, the capability of the system to record time and space resolved photoabsorption images, enabled us to measure the size of the expanding plasma plume (or at least the ground state atom/ion component) at different time delays. Hence, we were able to extract the plasma expansion velocity, and compare these results with the simulations. More sophisticated plasma expansion models which include ionisation and excitation balance with a given ion stage will be needed to make a more direct comparison with the selective data obtained here.

We were able to measure the size of the plasma plume up to an extent of 3 mm, which constitutes the brightest part of the VUV beam. Indeed, since the VUV beam intensity distribution was not homogeneous over the 4 mm we had to reduce it to 3 mm where the intensity was evenly distributed. This spatial dimension corresponds to a time window of 200 ns for the case of Ca^+ and 400 ns in the case of Ba^+ as determined by the expansion velocities of these species. At relatively short time delays ($\Delta t < 200$ ns for Ca^+, $\Delta t < 400$ ns for Ba^+) the plume hasn't detached from the target and the maximum values of the equivalent width are concentrated close to the target surface. Hence, as the equivalent

width distribution does not have a well-defined profile, to estimate the plasma dimensions we measured the distance over which the maximum value of the equivalent width dropped to 50%. This point was then followed out from the target surface as time increased and used to determine the Ca^+ and Ba^+ mean plume front positions as a function of time. The error on this measurement was taken to be the spatial resolution in the horizontal plane, i.e., 130 μm. From figure 4.10 and 4.12 we plot the dimension of the expanding plasma plume along the direction perpendicular to the target as a function of time.

The results are shown in figure 4.22.

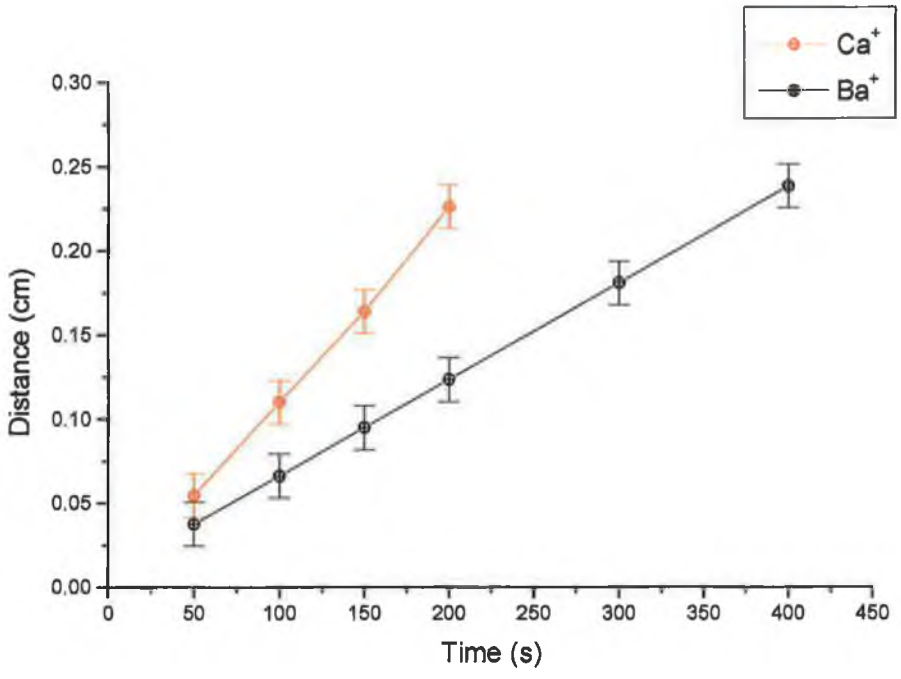

Figure 4.22. Plot of the plasma plume dimension along the direction of expansion (perpendicular to the target) with time (see text for details)

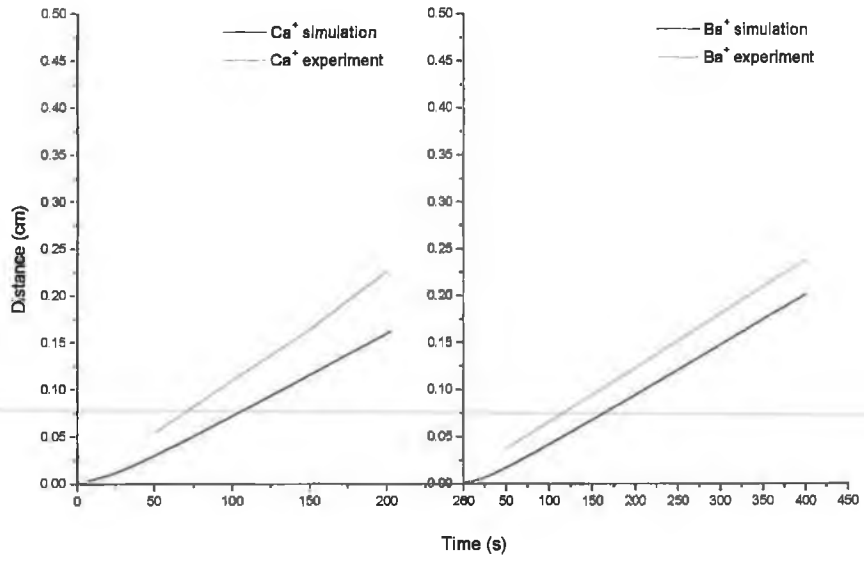

Figure 4.23. Comparison between the calculated (from Singh and Narayan model) and measured dimensions of the plasma plume, for a calcium plasma (left) and a barium plasma (right)

The experimental results have been measured from 50 ns onwards, which corresponds to the adiabatic expansion phase as describe in chapter 2. There is a linear relationship between the dimension of the plasma in the direction perpendicular to the target surface and time. Although the experimental values are higher than the values predicted by the code for both Ca^+ and Ba^+ dimensions, we note from figure 4.23 that the value of the slopes obtained graphically and experimentally are in good agreement. Hence, we expected good agreement between the measured and calculated expansion velocities. By applying a linear fit to the two experimental curves we can deduce the expansion velocity.

For Ca+ we extract a slope , i.e., an expansion velocity of 1.1×10^6 cms^{-1}

For Ba+ we extract a slope , i.e., an expansion velocity of 5.7×10^5 cms^{-1}

In figure 4.24 we show the expansion velocities calculated using the simulation program for Ca^+ and Ba^+.

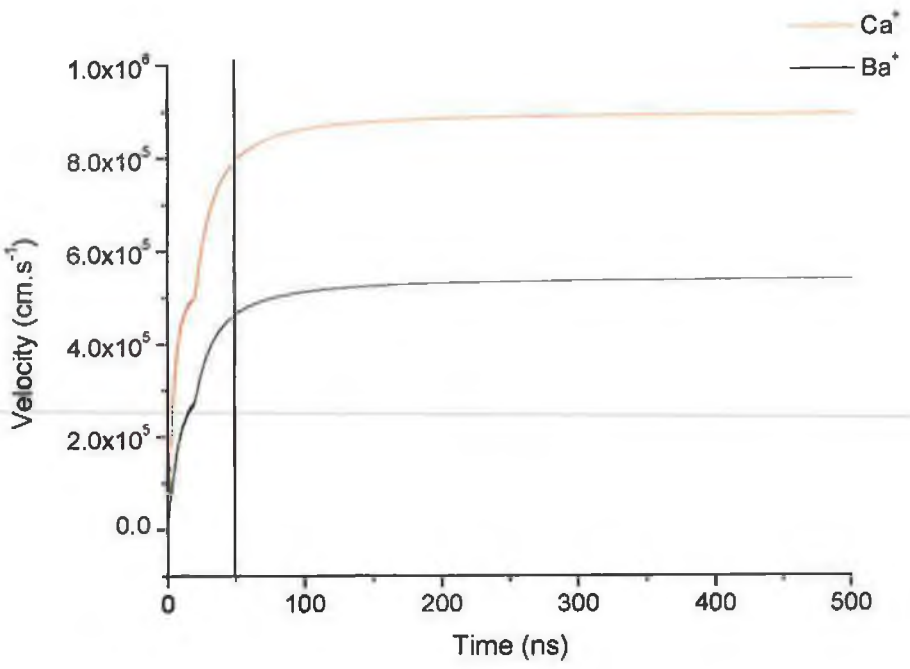

Figure 4.24. Evolution of the calculated expansion velocity of a calcium and barium plasma with time

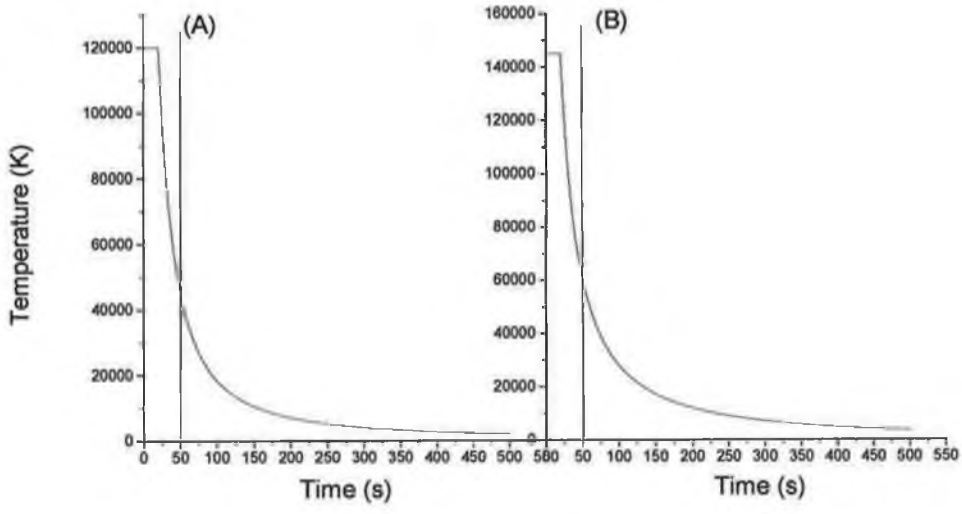

Figure 4.25. Evolution of the plasma temperature with time for (A) calcium plasma, and (B) barium plasma

There are two sources of errors on the determination of the plasma expansion velocity: the first is due to the measurement of the plasma dimensions, and the second is due to the accuracy of the time delay between the two laser pulses. As far as the measurement of the plasma dimensions is concerned the error is estimated to be the spatial resolution in the meridional plane, i.e., 130 μm.

The error on the delay between the two laser pulses was measured using two photodiodes and a digital oscilloscope. We measured a jitter of < 1 ns between the two laser pulses. As expected the error is large ~ 35 % for small distance and hence small time delays (50 ns), and decreases to ~ 12 % at longer time delays.

From figure 4.24 the plasma expansion velocity increases rapidly up to 50 ns where the curve flattens out and converges to a horizontal line. This sharp increase in the plasma velocity coincides with a rapid temperature decay during the first 50-70 ns, i.e., 30-50 ns after the end of the laser pulse. It is during this characteristic time that most of the thermal energy is transferred into kinetic energy, hence a large acceleration occurs.(Singh and Narayan 1990).

The plasma expansion velocity reaches an asymptotic value of 9×10^5 cm.s^{-1} for the Ca^+ ions and 5.4×10^5 cm.s^{-1} for the Ba^+ ions. These values compare well with the values obtained experimentally and hence we can assume that the bulk of the plasma plume is composed of singly charged ions under our experimental conditions.

Here, we have to point out that an initial temperature of 10 eV and 12 eV for the Ca^+ and Ba^+ ions respectively had to be used as an input into the simulation code. Since we are not able to measure plasma temperatures with the existing system, we compared these values with values obtained using the Collisional Radiative Model of Colombant and Tonon (1973). It is well known that laser plasmas similar to the ones produced in this work are well described by the Collisional Radiative equilibrium, and hence we are justified in its use (at least initially during the laser pulse). Moreover, with the range of electron densities we are dealing with and the temperature T_e inferred by the simulation code we deduce from figure 2.2. (Colombant and Tonon 1973) that we are effectively in a Collisional Radiative equilibrium. We estimated the dimensions of our line focus to be 3 mm by 100 μm, giving us a power density on target of ~ 6×10^9 Wcm^{-2}. We use the expression derived in Colombant and Tonon (1973) to estimate the initial plasma temperature:

$$T_e = 5.2 \times 10^{-6} A^{\frac{1}{5}} \left[\lambda^2 \phi \right]^{\frac{3}{5}}$$

where A is the element atomic number, λ the wavelength of the laser in microns and Φ the power density in $W.cm^{-2}$.

This approximation gives us an initial plasma temperature of ~ 7 eV for a calcium plasma and 9 eV for a barium plasma to compare with 10 eV and 12 eV required by the code. These small differences can be explained firstly by the approximate nature of the equation giving the expression of the temperature. Secondly, the focal spot size couldn't be measured very accurately and the sizes indicated here are upper limits so that the power density used in the equation correspond to a lower limit on the power density and hence a lower value of the initial temperature T_e.

4.4 Summary

We presented time and space resolved photoabsorption shadowgrams using the 3p – 3d transitions of neutral calcium, Ca^+ and Ca^{2+}. Maps of equivalent width have been recorded using the prototype system and compared to results obtained using the final system in the DCU laboratory. The principle leading to the derivation of maps of column density has been introduced, but the large value of the Ca^+ photoionisation cross section led to signal saturation and the results obtained were not conclusive. However, the results clearly show the improvements of the final DCU system, presenting a better spatial resolution and a much higher signal to noise ratio permitting a much more accurate data analysis.

The study of singly charged barium ions has been chosen to demonstrate the feasibility of the technique, i.e., the derivation of time and space resolved maps of column density. We show that even in non-optically thin opacity conditions, it is possible to derive maps of column density from maps of equivalent width using a simple mathematical procedure. Finally the plasma plume expansion velocity has been measured experimentally and the results are in good agreement with the plasma expansion model of Singh and Narayan (1990).

Chapter 5

Conclusions and future work

5 Summary

The description of the design and construction of a new imaging system operating in the VUV wavelength range constitute the core of this thesis. This final experimental system is a source of VUV radiation, collimated to a beam of cross section 4 mm x 4 mm, and tuneable from 30 nm to 300 nm (wavelength range of the Acton Research monochromator). The application of this system is the study of photoionisation using known transitions in calcium and barium atoms and ions to derive maps of time and space resolved column densities of the expanding plasma plume. The prototype system used in RAL based on a 0.2 meter monochromator was a proof of principle experiment to validate the VUV imaging technique. The main characteristics of the optical system are the following:

- A diverging beam (30 mrad divergence in the horizontal plane and 14 mrad in the vertical plane after the focus point) of cross section 3.8 mm x 2.6 mm at the sample is used as a probe beam.
- A resolving power of 30 at 30 nm to 100 at 100 nm is achieved using a combination of entrance and exit slit widths of 250 μm.
- A spatial resolution of 360 μm in the horizontal plane and 420 μm in the vertical plane is achieved.

The introduction of a 1 meter monochromator and two torroidal mirrors in the final system implemented in the DCU laboratory permitted a better focusing of the source onto the entrance slit of the monochromator and the collimation of the tuned VUV beam into a parallel beam of cross section 4 mm x 4 mm. As a result, the optical performance of the system has been considerably improved. The main characteristics of the final set-up are the following:

- A collimated beam of cross section 4 mm x 4 mm is used as a probe beam
- A resolving power of 400 at 30 nm to 1200 at 100 nm is achieved using entrance and exit slit widths of 100 μm
- A spatial resolution of 130 μm in the horizontal plane and 180 μm in the vertical plane using the same slit width combination is achieved

The toroidal mirror located before the entrance slit of the monochromator enabled us to reduce the width of the entrance slit and in doing so increased the spectral resolution of the system. At the same time, the better focusing properties of the mirror resulted in no flux loss at the entrance slit of the monochromator and permitted the use of grazing incidence angles and thus higher surface reflectivity.

The parameters of the toroidal mirror located after the exit slit of the monochromator have been chosen in order to create a parallel beam of cross section 4 mm x 4 mm. The use of a parallel beam as a probe beam ensures the required conditions for the derivation of the equation of radiative transfer, and the direct measurement of maps of equivalent widths. For transitions where the absolute cross section is known, the derivation of maps of column density can be achieved with a limited number of calculations. We applied this technique first to the study of calcium atoms and ions, in the 3p – 3d region of the spectrum, and more particularly to the Ca^+ ions where the absolute cross section has been measured by Lyon *et al.* (1987).

We were able to record time and space maps of equivalent width of neutral calcium using the 3p-3d resonance line at 39.48 nm, of Ca^+ using the 3p-3d resonance at 3734 nm and of Ca^{2+} using the 3p-3d resonance at 35.73 nm. The large photoionisation cross section of the Ca^+ resonance at 37.34 nm prevented us from deriving accurate maps of column density due to the saturation of the recorded absorption signal. This saturation introduced

large errors when converting the maps of equivalent width into maps of column density and hence, the results could not be interpreted.

The study of singly charged barium atoms using the 5p – 6d resonance at 46.68 nm was successfully performed and maps of column density showing values of 3×10^{15} cm^{-2} at short time delays to values of 1×10^{15} cm^{-2} at longer time delays were recorded.
The plasma plume expansion velocity was measured for singly charged ions of both calcium and barium and compared with the expansion model of Singh and Narayan (1990). The results show good agreement between the experimental measurements and the model predictions with expansion velocity of 9×10^5 $cm.s^{-1}$ for Ca^+ and 5.4×10^5 $cm.s^{-1}$ for Ba^+ ions in the expanding plasma plume.

5.1 Future system improvements

Although the system built in the DCU laboratory constitutes a major improvement with respect to the prototype system used at RAL, a few modifications to the system could be added.

First of all on the system itself, the design of a new target chamber housing the backlighting plasma seems indispensable. Indeed the actual chamber offers a very limited space to incorporate a high precision target holder. However one of the major concerns when performing an experiment is the alignment of the plasma source on the optical axis and its stability. The current custom-built target holder requires minor adjustments to retrieve the optimum position after moving the target to a fresh surface. It would then be most beneficial, to obtain consistent results, to have the capacity of moving the target to a fresh surface without altering the alignment. The combination of a motorised target holder permitting translations along the x, y and z axis from outside the vacuum chamber with flat target appears to be optimum. A similar mechanism as the target drive system used by Turcu *et al.* (1993) could nonetheless offer a good alternative. The motor driven tape arrangement uses metallic or polymer tape targets wound onto two constantly rotating spools ensuring a fresh target for every laser shot. The whole mechanism can be translated along the x, y and z axis using a series of motor for an accurate source positioning, the main problem being the target tapes which are not the standard targets in our laboratory.

The chamber housing the sample plasma could be modified to permit a more complete study of the expanding plasma plume. As mentioned the probe beam has a cross section of 4 mm x 4 mm, which does not probe the entire plasma plume. By fitting a high precision target holder it would then be possible to scan the whole plasma by translating the plasma vertically and/or horizontally. The difficulty is that the focusing conditions of the laser beam onto the target should remain unchanged. This could be realised by having the target holder and the lens holder used to focus the laser beam onto the target, connected together at a fixed distance and height. The study of the plasma at long time delays would then be obtained using several settings which could be assembled together to recreate the entire plasma plume ion distribution.

Finally, even though the modifications on the system built in DCU improved the light coupling between the source and the monochromator, the relatively low flux remains a serious concern. The optics designed in this system offer the optimum optical set-up with high reflectivity and low aberrations. In order to address the low VUV flux studies were begun on the effects of laser interaction with pre-formed plasmas with a view to increase the laser plasma flux per shot. Previous experiments have demonstrated a significant increase in soft X-ray flux emitted over direct laser target interaction (Collins 1993, Dunne *et al.* 2000), and encouraging results have been obtained in our laboratory in the VUV wavelength range. Preliminary studies on copper emission in the VUV have been carried out using a Nd-YAG (Continuum Surelite) laser delivering 800 mJ in 8 ns to form a "pre-plasma" which was subsequently heated by second Nd-YAG laser delivering 500 mJ in 150 ps (EKSPLA 312P). The results showed a gain of 3.5 in the VUV emission for an interlaser delay of 10 ns (Dunne *et al.* 2002). The influence of the use of different target shapes on the plasma emission as well as the characterisation of laser produced plasmas in capillaries is currently being carried out in the DCU laboratory. The aim of these studies is to achieve single shot operation.

On the detector side it would be valuable to calibrate the CCD camera for future absolute flux measurement on the plasma source. The Quantum Electronics Laboratory in the University of Padova has a calibrated VUV source that could be used to calibrate the VUV CCD. Moreover as the emission from the sample plasma is the dominant factor in decreasing the signal to noise ratio the use of a gated detector could partly solve this problem.

5.2 Applications

The applications of this imaging system are varied and numerous since the system constitutes essentially a collimated tuneable VUV source. This technique can be applied to the study individual components of multi-element semiconductors such as YBCO, which constitutes a very important element in pulsed laser deposition (Geohegan 1992, 1996). Taking barium as a reference, and monitoring the change in the barium column densities, the influence of the YBCO composition on thin film composition could be studied. At the same time the different column densities velocities of each component can be recorded in the VUV and the overall plume size and velocity inferred from the results.

In the normal photoionisation process, $A^{n+} + h\nu \rightarrow A^{(n+1)+} + e^{-}(T)$, a photon of frequency ν is absorbed by an atomic ion in charge state n to produce a photoelectron with kinetic energy $T=1/2(mv^2)$ and a remaining ion of charge n+1. This is referred to as "direct" photoionisation. However, if the photon energy $h\nu$ corresponds to the excitation energy of a inner transition, e.g., $Ca^{+}(3p^6\ 4s\ ^2S) + h\nu \rightarrow Ca^{+}(3p^5\ 3d\ 4s\ ^2P)$ there will be a resonant enhancement of the photoionisation cross section at this radiation frequency and hence "resonant" photoionisation. Of course the direct process is also present and the interference between the "direct" and resonant pathways will give the resonance its characteristic "Fano" shape (Fano 1961).

One of the limitations of resonant photoabsorption – photoionisation imaging is that absolute cross sections for atoms and ions are very few. However, looking at the non-resonant part of the photoionisation continuum, the total absorption cross section can be computed for all atoms and ions with good accuracy. Hence, we can apply the same technique to measure the equivalent width and convert it to column density (n_iL) of nearly all ions and atoms.

Let us consider two central frequency settings ν_1, ν_2, where both neutral and singly charged particles are present in the plasma, with respective cross sections $\sigma_0^{\nu 1}$ and $\sigma_+^{\nu 1}$ at the frequency ν_1 and $\sigma_0^{\nu 2}$ and $\sigma_+^{\nu 2}$ at ν_2. Assuming an optically thin plasma the equivalent widths $W_{\nu 1}$ and $W_{\nu 2}$ can be written as:

$$W_{\upsilon 1} = (n_i L)_0 \int_{\Delta\upsilon_1} \sigma_0^{\upsilon 1} d\upsilon + (n_i L)_+ \int_{\Delta\upsilon_1} \sigma_+^{\upsilon 1} d\upsilon$$

$$W_{\upsilon 2} = (n_i L)_0 \int_{\Delta\upsilon_2} \sigma_0^{\upsilon 2} d\upsilon + (n_i L)_+ \int_{\Delta\upsilon_2} \sigma_+^{\upsilon 2} d\upsilon$$

Solving the system of equations we can extract the value of both the column density for neutral and singly ionised species:

$$(n_i L)_0 = \frac{W_{\upsilon 1} \int_{\Delta\upsilon_2} \sigma_+^{\upsilon_2} d\upsilon - W_{\upsilon 2} \int_{\Delta\upsilon_1} \sigma_+^{\upsilon 1} d\upsilon}{\int_{\Delta\upsilon_1} \sigma_0^{\upsilon 1} d\upsilon \int_{\Delta\upsilon_2} \sigma_+^{\upsilon 2} d\upsilon - \int_{\Delta\upsilon_1} \sigma_+^{\upsilon 1} d\upsilon \int_{\Delta\upsilon_2} \sigma_0^{\upsilon 2} d\upsilon}$$

$$(n_i L)_+ = \frac{W_{\upsilon 2} \int_{\Delta\upsilon_1} \sigma_0^{\upsilon_1} d\upsilon - W_{\upsilon 1} \int_{\Delta\upsilon_2} \sigma_0^{\upsilon_2} d\upsilon}{\int_{\Delta\upsilon_1} \sigma_0^{\upsilon 1} d\upsilon \int_{\Delta\upsilon_2} \sigma_+^{\upsilon 2} d\upsilon - \int_{\Delta\upsilon_1} \sigma_+^{\upsilon 1} d\upsilon \int_{\Delta\upsilon_2} \sigma_0^{\upsilon 2} d\upsilon}$$

Here, using the maps of the equivalent width obtained experimentally we see that a simple subtraction between images will lead to maps of column density n_iL for the different species present in the plasma

The imaging system is planned to be used for the determination of optical constants and thickness of thin films by imaging the incident, reflected and transmitted beam. First of all, the optical constants of the thin film deposited on the substrate are determined using the incident and reflected images. Images of the light absorbed by the substrate can then be generated. By determining the displacement between the incident and transmitted beams, using geometrical optics the thickness of the substrate can be inferred. This experiment requires a specific target chamber for the substrate analysis, which has already been built, as part of a research program in the DCU laboratory by fellow student J. Mullen and his advisor Dr. P. Van Kampen. Preliminary tests have been carried out in the visible region, leading to measurements of thin films thickness with an accuracy of 10 μm. As a new commercial PLD system will be acquired by Dr. Jean Paul Mosnier, this diagnostic will reveal itself useful to characterise the samples grown in our laboratory in the VUV wavelength range.

The study of colliding plasmas has attracted much interest in the last decade due to obvious interest in astrophysics and collision physics. Until now, only emission studies on the effect of colliding plasma have been carried out using pinhole photography as an imaging technique and XUV spectroscopy as another diagnostic. Ruhl *et al.* (1997), Henc-Bartolic *et al.* (1998), Harilal *et al.* (2001) used these diagnostics to study the process of charge exchange collisions in carbon, boron nitride, and magnesium colliding plasmas respectively. The same experiments could be repeated here to monitor the effect of plasma collisions using photoabsorption imaging; in particular the physics should be quite different since collisions between ground state species can be studied as opposed to those between excited species as in emission spectroscopy and imaging. Also, collisions between energy carrying metastables species, known to be important in fusion plasmas and likely to be important in thin film deposition, can be easily tracked using the photoabsorption imaging system.

References

Altun Z, Carter S.L, Kelly H.P, Physical Review A, Vol 27, p 1943, (1983).

Altun Z, Kelly H.P, Physical Review A, Vol 31, p 3711, (1985).

ANDOR, private communications, September 2002.

Aota T, Yamagushi N, Ikeda K, Aoki S, Yoshikawa M, Mase A, Tamano T, Review of Scientific Instruments, Vol. 68, p1661, (1997).

Balmer J, Lewis C.L.S, Corbett R.E, Robertson E, Saadat S, O'Neil D.M, Kilkenny J.D, Back C.A, Lee R.W, Physical Review A, Vol. 40, p 330, (1989).

Barford N.C, "*Experimental measurements: Precision, Error and Truth*", Wiley, New York, (1985).

Beutler H.G, Optical Society of America, Vol. 35, p 311, (1945).

Bizau J.M, Gerard P, Wuilleumier F.J, Physical Review A, Vol. 36, p 1220, (1987).

Bizau J. M., Cubaynes D, Richter M, Wuilleumier F. J, Obert, J, Putaux J. C, Morgan T. J, Källne E, Sorensen S, Damany A, Physical Review Letter, Vol. 67, p 576, (1991).

Bobkowski R, Fedosejevs R, journal of Vacuum Science and Technology A, Vol. 14, p 1973, (1996).

G. Bonfante, "Light Path Simulation Ray Tracing Code", M.Sc. thesis (Universita degli Studi di Padova) (1989) (unpublished).

Brehm J.J, Mullin W.J, "*Introduction to the structure of matter : a course in modern physics*", Wiley, New York, (1989).

Breton C. and Papoular R., Journal of the Optical Society of America, Vol. 63, p 1225, (1973).

Cantu A.M, Tondello G, Applied Optics, Vol.14, p 996, (1975).

Carillon A, Jaegle P, Dhez P, Physical Review Letters, Vol.25, p140, (1970).

Carroll P.K, Kennedy E.T, Physical Review Letters, Vol. 64A, p37, (1977).

Carroll P.K, Kennedy E.T, O'Sullivan G, Optics Letters, Vol. 2, p 72, (1978).

Carroll P.K, Kennedy E.T, O'Sullivan G, Applied Optics, Vol. 19, p 1454, (1980).

Carroll P.K and Kennedy E.T, Contemporary Physics, Vol 22, p 61, (1981).

Carroll P.K, Kennedy E.T, O'Sullivan G, IEEE Journal of Quantum Electronics, Vol. QE-19, p1807, (1983).

Collins M, M.Sc. Thesis, Dublin City University, (1993).

Colombant D, Tonon G.F, Journal of Applied Physics, Vol. 44, p 3524, (1973).

Connerade J.P, Mansfield M.W.D, Newsom G.H, Tracy D.H, Baig M.A, Thimm K, Philosophical Transactions of the Royal Society of London, Vol. 290, p 327, (1979)

Connerade J.P, Sarpal B.K, Journal of Physics B, Vol. 25, p 2245, (1992).

Corney A, "*Atomic and Laser Spectroscopy*", Clarendon Press, Oxford (1977).

Corson D.R and Lorrain P, "*Electromagnetic fields and waves*", Freeman, New York, (1988).

Costello J.T, Mosnier J.P, Kennedy E.T, Carroll P.K, O'Sullivan G, Physica Scripta, Vol. T34, p 77, (1991).

Daido H, Nishimura H, Tateyama R, Ogura K, Nakai S, Yamanaka, Journal of Applied Physics, Vol. 56, p 3360, (1984).

Dardis L, M.Sc. Thesis, Dublin City University, (1998).

Dawson J. M., Physics of Fluids, Vol. 7, p 981, (1964)

Doyle B, M.Sc. Thesis, Dublin City University, (1995)

Dunne P., O'Sullivan G., O'Reilly D., Applied Physics Letters, Vol. 76, p 34, (2000).

Dunne P., O'Sullivan G, Kilbane D, Kennedy E.T, Neogi A, Murphy A, Mosnier J.P, Hirsch J.S, Costello J.T, Neely D, Foster P, Divall E.J, Hooker C.J, Langley A.J. SPIE Conference Proceedings, vol 4876, (2002).

Eliezer S, "*The interaction of high power lasers with plasmas*", Institute of Physics Publishing, (2002).

Fano U., Physical Review 124, p 1866, (1961)
Fischer J, Kuhne M, Wende B, Applied Optics, Vol. 23, p 4252, (1984).

Folkard M, Schettino G, Vojnovic B, Gilchrist S, Michette A. G, Pfauntsch S. J, Prise K. M, Michael B. D, Radiation research, Vol. 156, p 196, (2001).

Gamaly E.G, Rode A.V, Luther-Davies B, Applied Physics A, Vol. 69, p 121, (1999).

Geohegan D.B, Applied Physics Letters, Vol. 60, p 2732, (1992).

Geohegan D.B, Puretzky AA, Applied Physics Letters, Vol. 67, p 197, (1995).

Geohegan D.B, Puretzky AA, Applied Surface Science, Vol 96-98, p 131, (1996).

Gray A, PhD thesis, Dublin City University, (1999).

Griem H.R, "*Plasma Spectroscopy*", McGraw-Hill, (1964).

Grun J, Kacenjar S, Applied Physics Letters, Vol. 44, p 497, (1984).

Hansen J.E, Journal of Physics B, Vol. 7, p 1902, (1974).

Hansen J.E, Journal of Physics B, Vol. 8, p 2759, (1975).

Harilal S.S, Bindhu C.V, Shevelko V.P, Kunze H-J, Journal of Physics B, Vol. 34, p 3717, (2001).

Henc-Bartolic V, Andreic Z, Gracin D, Aschke L, Ruhl F, Kunze H-J, Physica Scripta, Vol. T75, p 297, (1998).

Hill W.T, Cheng K.T, Johnson W.R, Lucatorto T.B, McIlrath T.J, Sugar J, Physical Review Letters, Vol. 49, p 1631, (1982).

Hill W.T, Sugar J, Lucatorto T.B, Cheng K.T, Physical Review A, Vol. 36, p 1200, (1987).

Hirsch J. S, Meighan O, Mosnier JP, van Kampen P, Whitty W. W, Costello J. T, Lewis C. L. S, MacPhee A. G, Hirst G. J, Westhall J, Shaikh W, Journal of Applied Physics, Vol. 88, p 4953, (2000).

Holland D.M.P, Codling K, Chamberlain R.N, Journal of Physics B, Vol. 14, p 839, (1981).

Hughes T.P, "*Plasmas and Laser Light*", Adam Hilger, London (1975).

Jannitti E, Gaye M, Mazzoni M, Nicolosi P and Villoresi P, Physical Rview A, Vol. 47, p 4033, (1993).

Kaaret P, Geissbuhler P, Chen A, Glavinas E, Applied Optics, Vol. 31, p 7339, (1992).

Kalantar D.H, Haan S.W, Hammel B.A, Keane J, Landen O.L, Munro D.H, Review of Scientific Instrument, Vol. 68, p 814, (1997).

Kennedy E.T, Contemporary Physics, Vol. 25, p 31, (1984).

Kent L.W.J, Connerade J.P, Thorne A.P, Journal of Physics B, Vol. 20, p 1947, (1987).

Kiefer J-C, Chaker M, Pepin H, Villeneuve D.M, Bernard J.E, Baldis H.A, Applied Optics, Vol. 28, (1989).

Kiernan L, Phd Thesis, Dublin City University, (1994)

Koog J, Iwasaki K, Review of Scientific Instruments, Vol 67, p 3871, (1996).

Lewis C.L.S, McGlinchey J, Optics Communications, Vol. 53, p 179, (1985).

Lochte-Holtgreven W, "*Plasma Diagnostic*", AIP Press, New York, (1995).

Lucatorto T.B, McIlrath T.J, Applied Optics, Vol. 19, p 3948, (1980).

Lyon I.C, Peart B, West J.B, Kingston A.E, Dolder K Journal of Physics B, Vol. 17, p L 345, (1984).

Lyon I.C, Peart B, Dolder K, West J.B, Journal of Physics B, Vol. (19, p 4137, (1986).

Lyon I.C, Peart B, Dolder K, West J.B, Journal of Physics B, Vol. 20, p 1471, (1987).

Maloney C, M.Sc. Thesis, (1998).

Malvezzi A.M, Garifo L, Tondello G, Applied Optics, Vol 20, p 2560, (1981).

Mansfield M.W.D, Newsom G.H, Proceedings of the Royal Society of London, Series A, Vol. 357, p 77, (1977).

Martin G.W, Doyle L.A, Al-Khateeb A, Weaver M, Lamb M.J, Morrow T, Lewis C.L.S, Applied Surface Science, Vol. 129, p 710, (1998).

McWhirter R.W.P, "*Plasma diagnostic techniques*", Huddlestone R.H and Leonard S.L, Academic Press, (1965).

Mehlhorn W, Breuckmann B, Hausamann D, Physica Scripta, Vol. 16, p 177, (1977).

Meighan O, PhD thesis, Dublin City University, 2000

Michette A.G, Fedosejevs R, Pfauntsch S.J, Bokowski R, Measurement Science and Technology, Vol. 5, p 555, (1994).

Momma C, Chichkov B.N, Nolte S, Von Alvensleben F, Tunnermann A, Welling H, Wellegehausen B, Optics Communications, Vol. 129, p 134, (1996).

Namioka T, Journal of the Optical Society of America, Vol. 49, p446, (1959).

O'Neil D.M, Lewis C.L.S, Neely D, Davidson S.J, Physical Review A, Vol. 44, p 2641, (1991).

O'Sullivan G, Carroll P.K, McIlrath T.J, Ginter M.L, Applied Optics, Vol. 20, p 3043, (1981).

O'Sullivan G, Roberts J.R, Ott W.R, Bridges J.M, Pittman T.L, Ginter M.L, Optics Letters, Vol. 7, p 31, (1982).

Pikus T.A, Faenov A. YA, Fraenkel M, Zigler A, Flora F, Bollanti S, Lazzaro P.DI, Letardi T, Grilli A, Palladino L, Tomassetti G, Reale A, Reale L, Scafati A, Limongi T, Bonfigli F, Alainelli L, Shanchez Del Rio M, Laser and Particle Beams, Vol. 19, p 285, (2000).

Puretzki A.A, Geohegan D.B, Jellison G.E, McGibbon M.M, Applied Surface Science, Vol. 96-96, p 859, (1996).

Radziemski L.J, "Laser-induced plasmas and applications", Dekker M., New York, (1989).

Raven A, Azechi H, Yamanaka T, Yamanaka C, Physical Review Letters, Vol. 47, p1049, (1981).

Rense W.A, Violett T, Journal of the Optical Society of America, Vol. 49, (1959).

Rose S.J, Grant I.P, Connerade J.P, Philosophical Transactions of the Royal Society of London, Vol. 296, p 41, (1980).

Rowland H.A, Phil. Mag, Vol 13, p 469, (1882).

Rowland H.A, Phil. Mag, Vol 16, p 197, (1883).

Ruhl F, Aschke L, Kunze H-J, Physics Letters A, Vol. 107, p 225, (1997).

Samson J.A.R., "*Techniques of Vacuum Ultraviolet Spectroscopy*", Pied Publications, Lincoln, Nebraska, (1967).

Sanchez Del Rio M, Pikus T.A, Faenov A. YA, Fraenkel M, Zigler A, Review of Scientific Instruments, Vol. 70, p 1614, (1999).

Sato Y, Hayaishi T, Itikawa Y, Itoh Y, Murakami J, Nagata T, Sasaki T, Sonntag B, Yagishita A, Yoshino M, Journal of Physics B, Vol. 18, p 225, (1985).

Schmidt V, Reports on Progress in Physics, Vol 55, p 1483, (1992).

Shigemori K, Azechi H, Nakai M, Honda M, Meguro K, Miyanaga N, Takabe H, Mima K, Physical Review Letters, Vol. 78, p 250, (1997).

Shin H.J, Kim D.E and Lee T.N, Review of Scientific Instruments, Vol. 66, p 4222, (1995).

Singh R.K. and Narayan J, Physical Review B, Vol. 41, p 8843, (1990).

Tondello G, Optica Acta, Vol. 26, p357, (1979).

Turcu I.C.E, Ross I.N, Schulz M.S, Daido H, Tallents GJ, Krishnan J, Dwivedi L, Hening A, Journal of Applied Physics, Vol. 73, p.8081, (1993).

Ueda K, West J.B, Ross K.J, Hamdy H, Beyer H.J, Kleinpoppen H, Physical Review A, Vol 48, p 863, (1993).

Van Kampen P, Kiernan L, Costello J.C, Kennedy E.T, Van der Mullen J.A.M, O'Sullivan G, Journal of Physics B, Vol. 28, p 4771, (1995).

Villoresi P, Nicolosi P, Review of Scientific Instruments, Vol. 65, p 2049, (1994).

Villoresi P, Nicolosi P, Pelizzo M.G, Applied Optics, Vol. 39, p 85, (2000).

West J.B, Journal of Physics B, Vol. 34, P R45, (2002).

Whitlock R.R, Obenschain S.P, Grun J, Applied Physics Letters, Vol. 41, p 429, (1982).

Whitty W, Mosnier J-P, Applied Surface Science, Vol. 129, p 1035, (1998).

Wilkins S.W, Stevenson A.W, Nugent K.A, Chapman H, Steenstrup S, Review of Scientific Instruments, Vol. 60, (1989).

Williams C.S. and Becklund O.A, "*Introduction to the Optical Transfer Function*", John Wileys and Sons (1989).

Ymaguchi N, Aoki S, Miyoshi S, Review of Scientific Instruments, Vol. 58, p 43, (1987).

List of figures

List of tables

Appendix 1.

Mechanical drawings of the x,y,z target holder (after Moloney 1998)

Figure 1. Schematic of XYZ translation mount assembly (without guide rails).

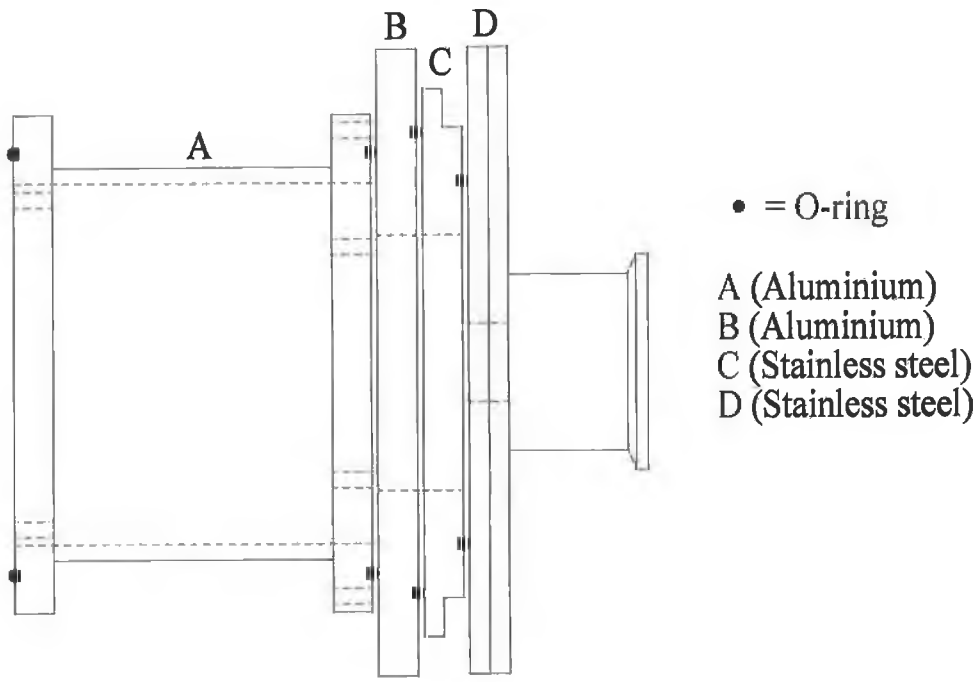

Figure 2. Schematic of extension flange *A*.

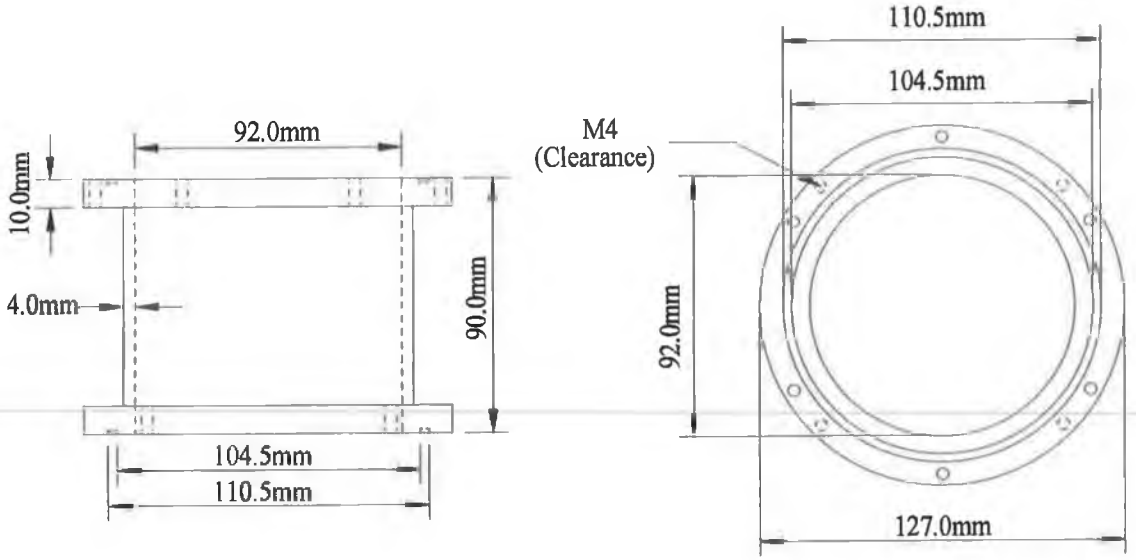

Figure 3. Schematic of mounting plate *B*.

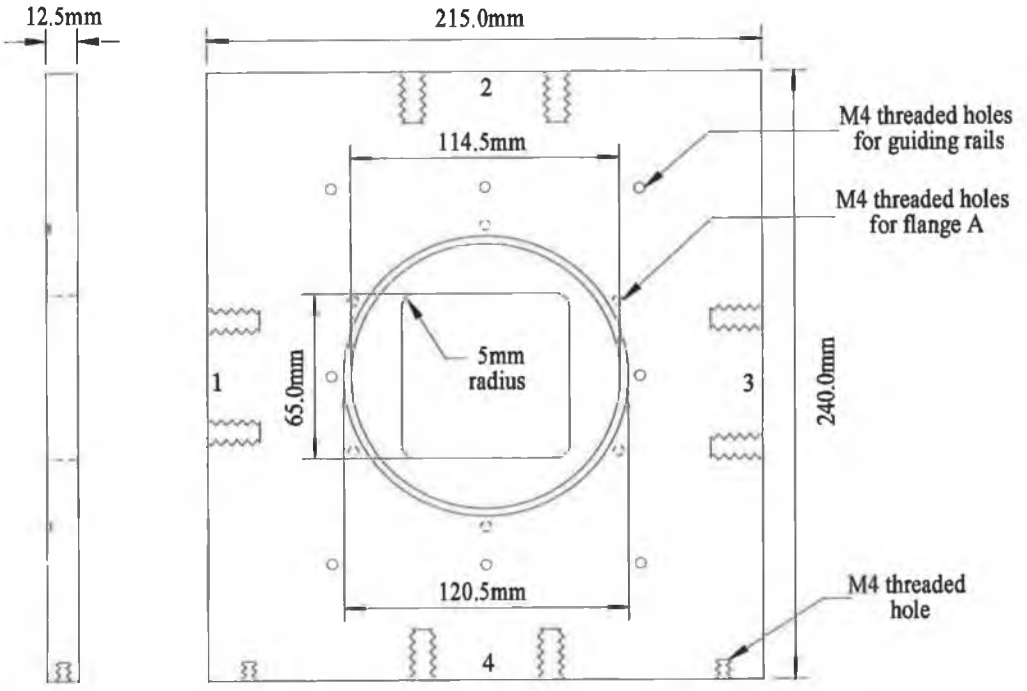

Figure 4. Schematic of the support legs for the mounting plate *B*

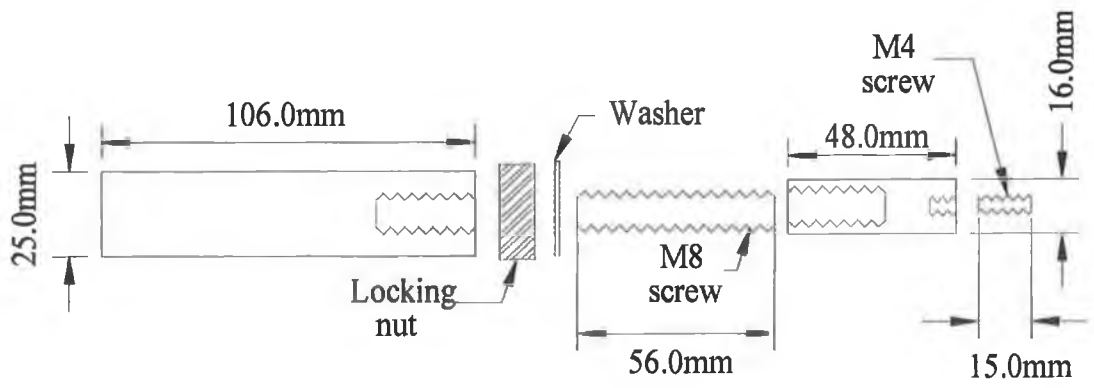

Figure 5 Schematic of micrometer and thumbscrews holders for mounting plate *B* in figure 4.

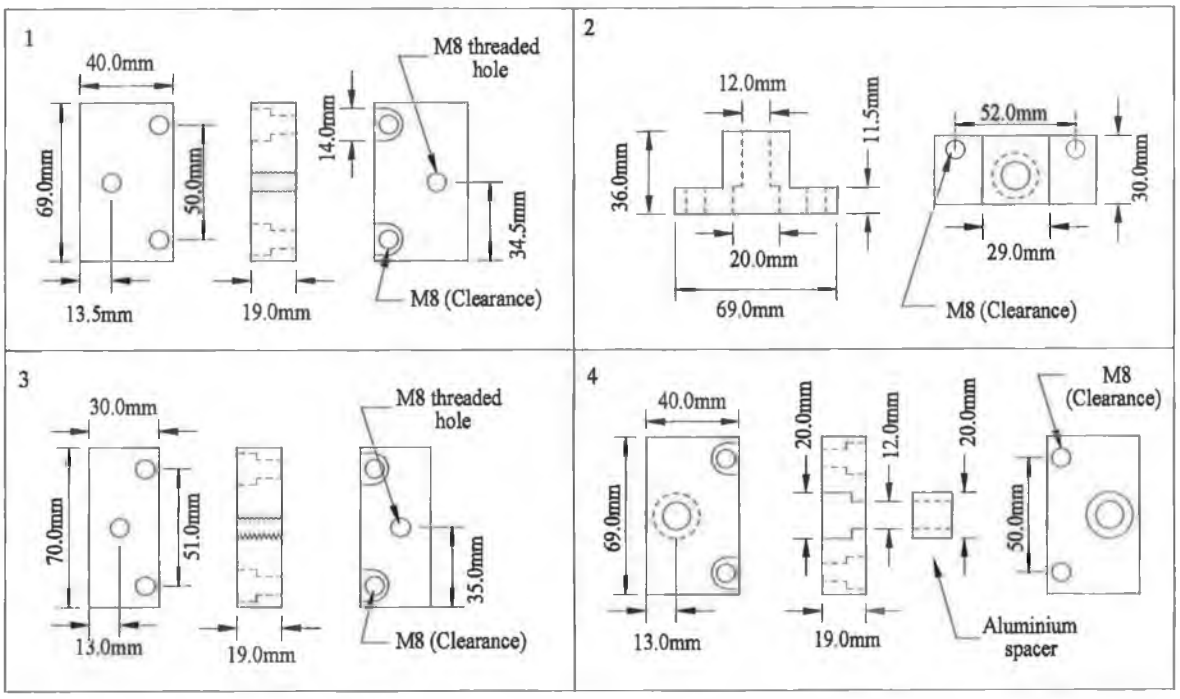

Figure 6. Schematic of horizontal sliding plate *C*.

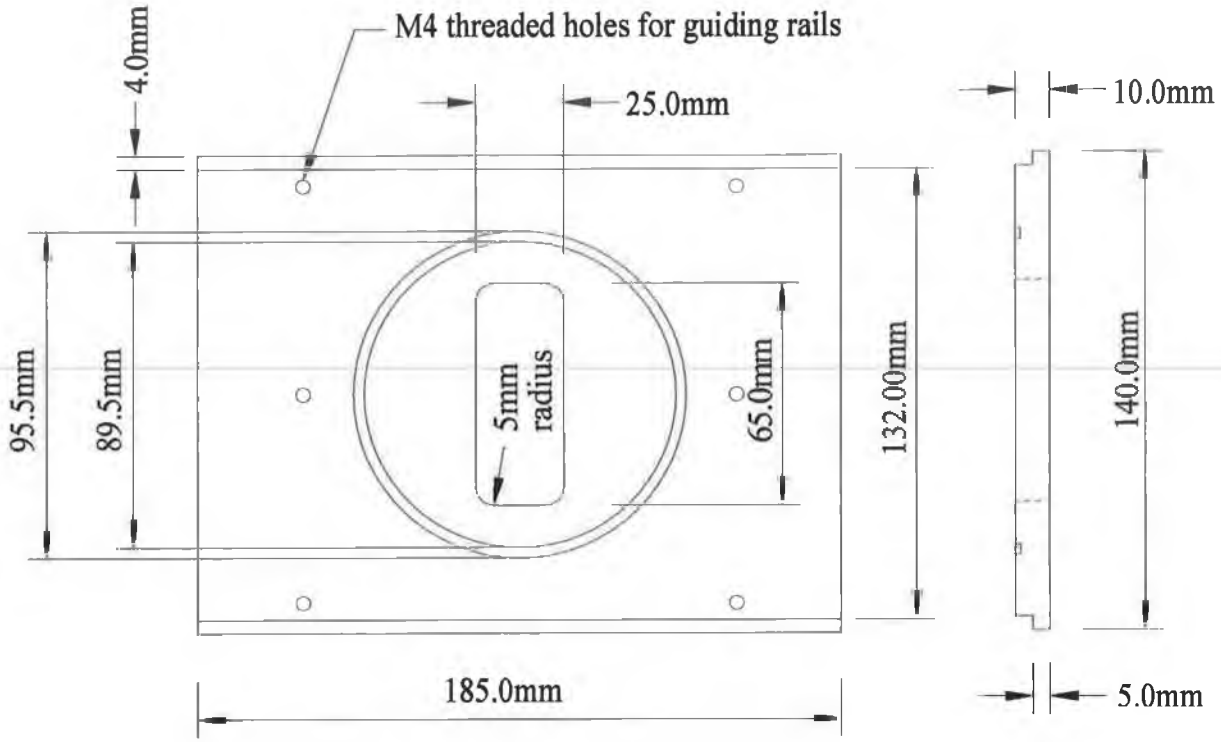

Figure 7. Schematic of sliding plate

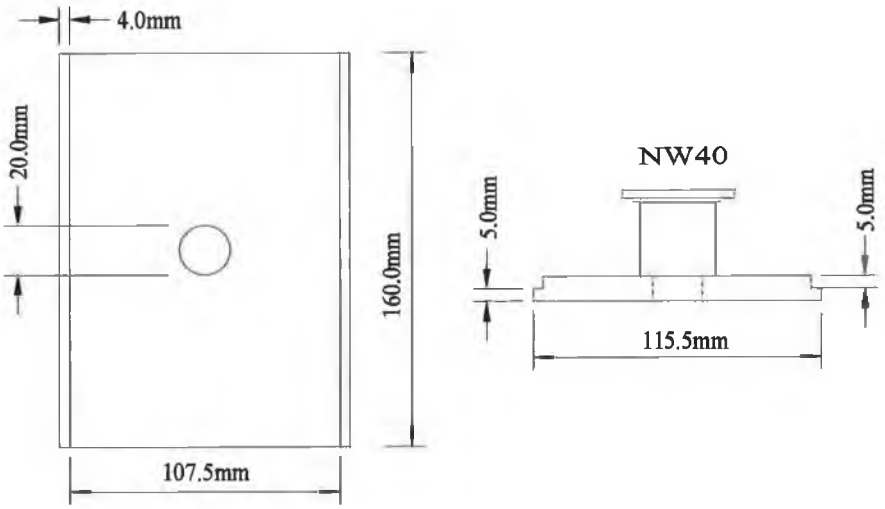

Figure 8. Schematic of the guide rails.

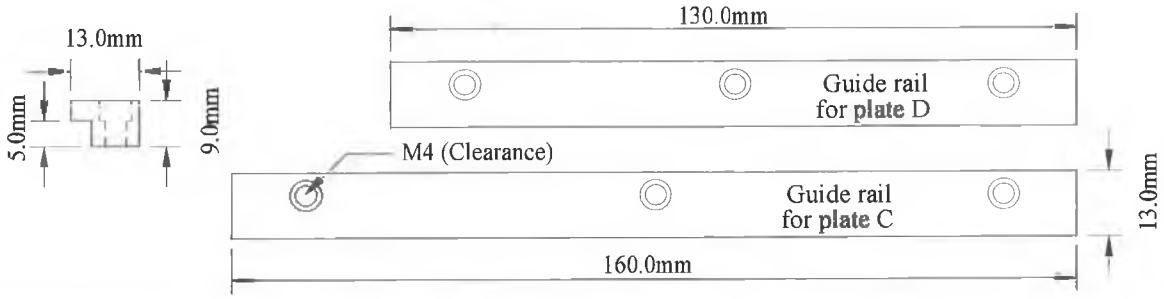
13.0mm
5.0mm
9.0mm
130.0mm
Guide rail
for plate D
M4 (Clearance)
Guide rail
for plate C
13.0mm
160.0mm

Appendix 2.

Mechanical drawings of the mirror chambers

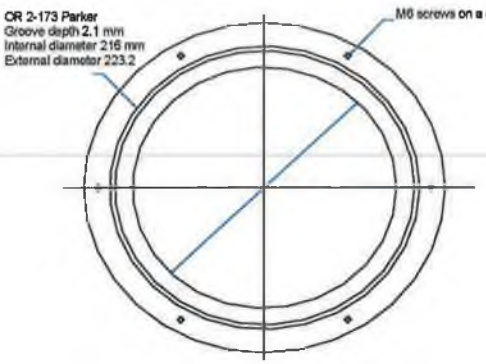

Mirror chamber
top view

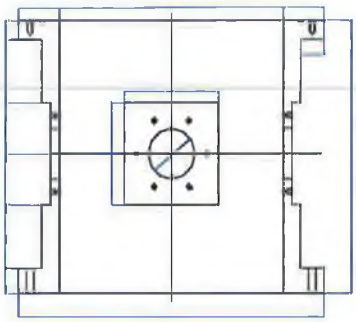

Mirror chamber
side view

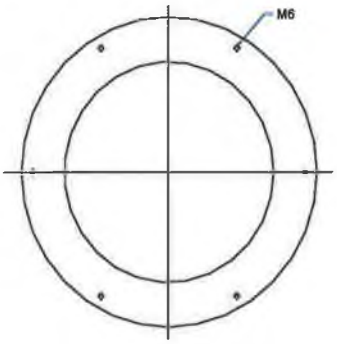

Mirror chamber top plate

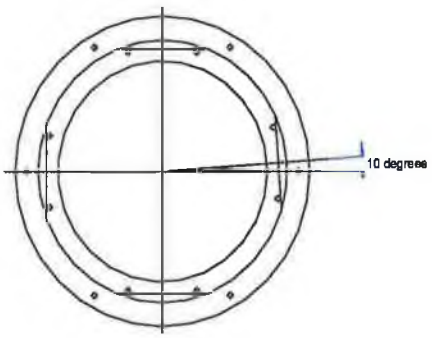

Top view of the mirror chamber
Entrance/exit ports disposition

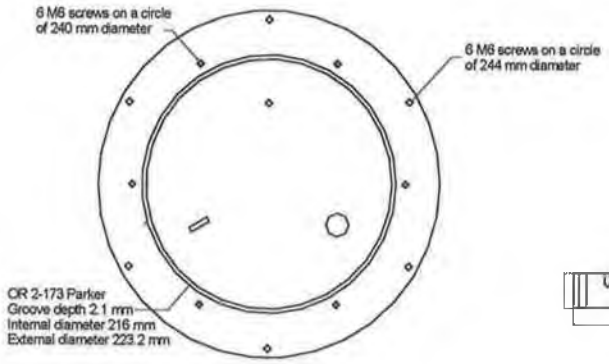

Mirror chamber bottom plate
Top view

Mirror chamber bottom plate
Side view

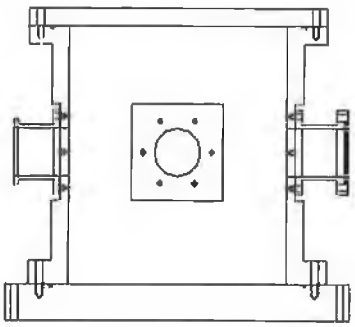

Mirror chamber showing exit ports
Side view

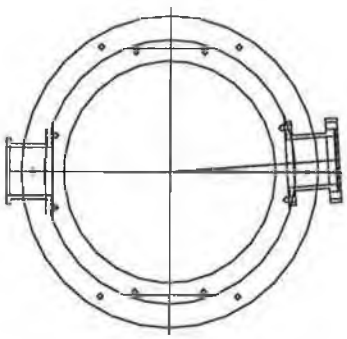

Mirror chamber showing exit ports
Top view

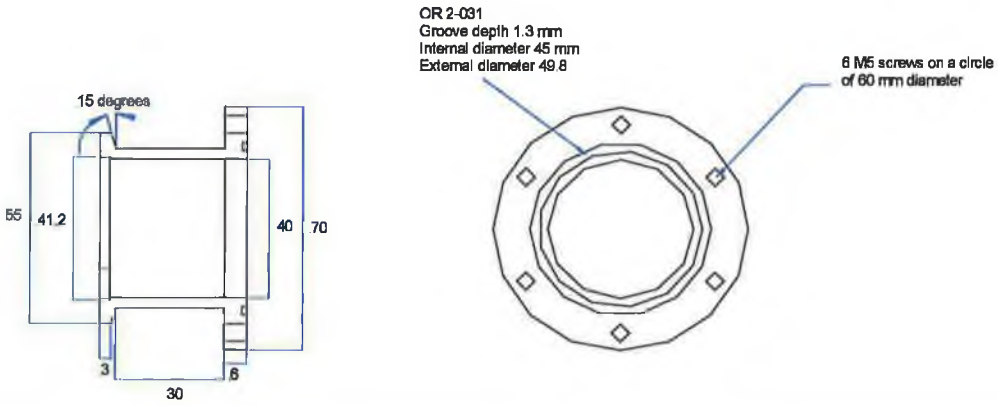

Exit port of target chamber

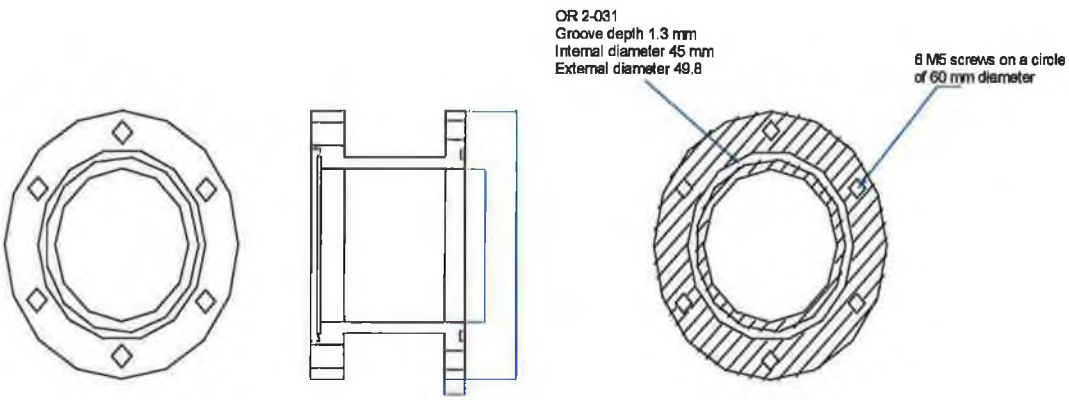

Exit port of target chamber